Nanocarbon-Enforced Anisotropic MusCAMLR for Rapid Rescue of Mechanically Damaged Skeletal Muscles

Niranjan Chatterjee and Santosh Kumar Misra*

Cite This: https://doi.org/10.1021/acsami.3c01889

Read Online

ACCESS | Metrics & More | Article Recommendations | Supporting Information

ABSTRACT: Mechanical damages to skeletal muscles could be detrimental to the active work hours and lifestyle of athletes, mountaineers, and security personnel. In this regard, the slowness of conventional treatment strategies and drug-associated side effects greatly demand the design and development of novel biomaterials, which can rescue such mechanically damaged skeletal muscles. To accomplish this demand, we have developed a musculoresponsive polymer−carbon composite for assisting myotubular regeneration (MusCAMLR). The MusCAMLR is enforced to attain anisotropic muscle-like characteristics while incorporating a smartly passivated nanoscale carbon material in the PNIPAM gel under physiological conditions as a stimulus, which is not achieved by the pristine nanocarbon system. The MusCAMLR establishes a specific mechanical interaction with muscle cells, supports myotube regeneration, maintains excellent mechanical similarity with the myotube, and restores the structural integrity and biochemical parameters of mechanically damaged muscles in a delayed onset muscle soreness (DOMS) rat model within a short period of 72 h. Concisely, this study discloses the potential of smartly passivated nanocarbon in generating an advanced biomaterial system, MusCAMLR, from a regularly used polymeric hydrogel system. This engineered polymer−carbon composite reveals its possible potential to be used as a nondrug therapeutic alternative for rescuing mechanically damaged muscles and probably can be extended for therapy of various other diseases including muscular dystrophy.

KEYWORDS: skeletal muscles, PNIPAM hydrogel, carbon nanoparticle, polymer−carbon composite, delayed onset muscle soreness
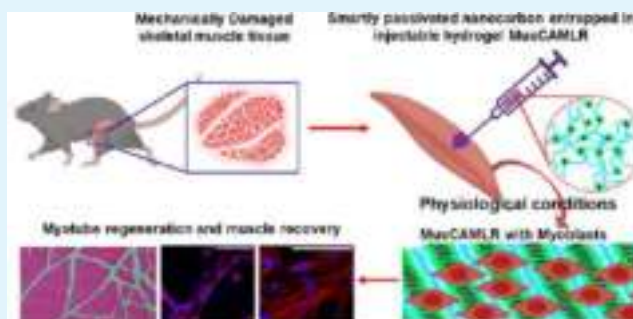
INTRODUCTION

Skeletal muscles are identified as one of the major organs of the body, as they constitute more than 40% of the average body mass and contribute to voluntary physical activities such as locomotion and other physiological functions. These functions generally occur by secreting several myokines to communicate with other vital organs of the body.[1] Several causal events such as high-intensity exercise, mountaineering, skiing, traffic accidents, combat injuries, excessive walking in uneven topographies, patrolling in jungle, traumatic injury of the soldiers in the battlefield, etc. result in mechanical damages of the skeletal muscles. These kinds of mechanical injuries are characterized by volumetric muscle loss, which destroys the structural integrity as well as functional ability of the skeletal muscles. Inflammation, pain initiation, and disruption of the extracellular matrix are some of the sets of physiological events which become conspicuous as a consequence of the mechanical damage. These could result in myofibrillar destruction and streaming of the Z-line as an integral part of the sarcomere.[2] Different approaches have been taken into consideration for the effective treatment of such mechanically damaged skeletal muscles, which include bracing and augmenting the strength of the remaining muscle fibers,

stimulating the regeneration ability of resident stem cells of skeletal muscles, i.e., satellite cells, myoblast, etc., in the case of volumetric muscle loss.[3] Although the efforts toward the improvement of myogenic potential have brought some hope by increasing the regenerative index, it has been found to be inadequate because of less cell viability, decreased cell migration, and the requirement of immunosuppressive therapy.[3,4] Nonsteroidal anti-inflammatory drugs (NSAIDs) have also been applied to some extent to alleviate symptoms like the pain production of strain-induced mechanical damage of skeletal muscles, but interestingly, there has been no such correlation established between pain sensation and the extent of skeletal muscle damages.[2,5] With the advancement in the field of tissue engineering, the application of engineered polymeric materials has created some landmarks in preventing muscle loss after severe acute mechanical trauma. Typically,

Scheme 1. Summary of the Key Steps of Preparation and Characterization of MusCAMLR to Bring Its Ability to Maintain the Unique Myotube Property[a]
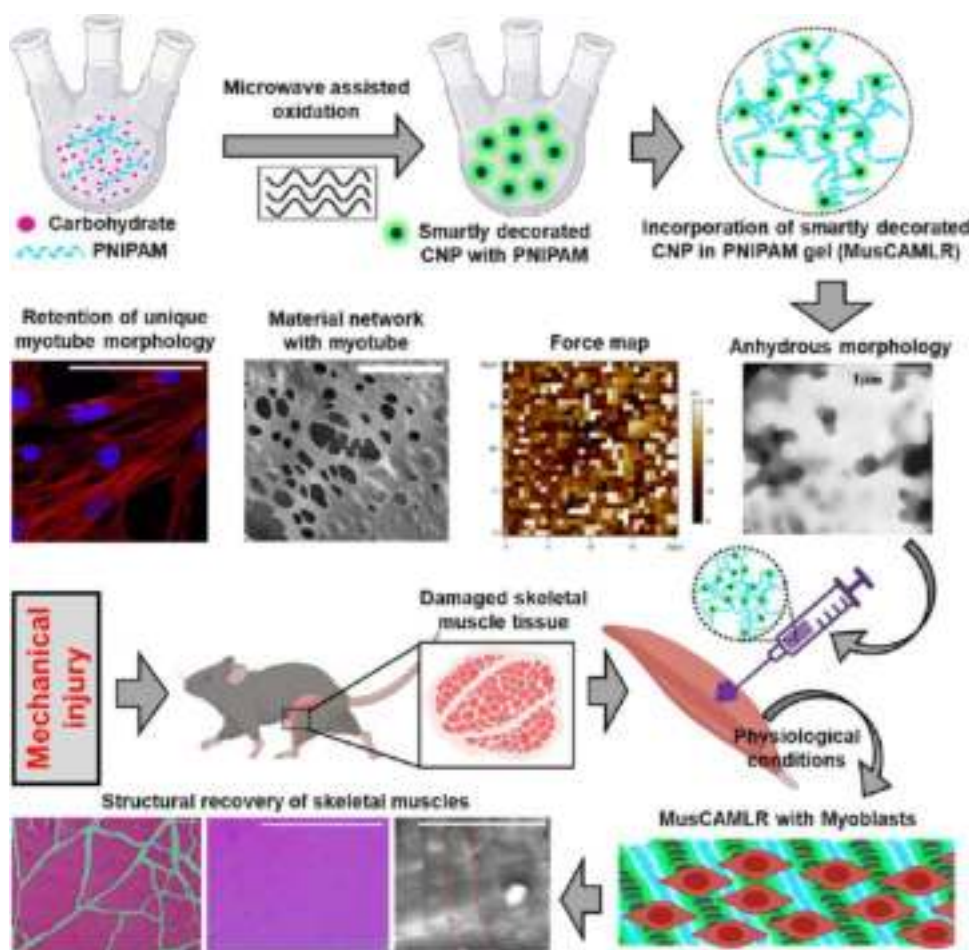
[a]It was achieved by MusCAMLR forming a special material network, which governs its functional efficiency to rescue mechanically damaged skeletal muscles within a short period of time

tissue engineering approaches are built to promote the regeneration of skeletal muscles by developing scaffolds, which are isolated from natural sources including different species, several organs, and tissues or designed in several configurations including electrospun scaffolds, foams, meshes, etc., using synthetic polymers, e.g., polypropylene, poly(lactic-co-glycolic acid), poly(ε-caprolactone), etc.[6,7] These could be used either to deliver muscle stem cells to the site of injury, i.e., cellular scaffold, or to deliver bioactive compounds such as growth factors for the proliferation and/or differentiation of satellite cells/myoblasts, i.e., acellular scaffold. However, these approaches are limited because of the size of the construct design to insert inside the host tissue and stimulation of immunogenic responses, etc. Skeletal muscle fibers are precisely organized, which are capable of contracting and relaxing anisotropically in the longitudinal direction for proper functioning.[8,9] Tremendous efforts have been made in search of such muscle mimics that can function inside the physiological environment and support the growth of skeletal muscles with appropriate dimensions and architecture. Nevertheless, this requires different high-throughput techniques, e.g., electrospinning, three-dimensional (3D) printing, etc., for controlling the orientation of the scaffold to achieve well-aligned morphology-like skeletal muscles.[8,10] In this direction, designing novel biocompatible materials with a controlled

anisotropic architecture, equivalent mechanical property with skeletal muscles in the presence of physiological cues, and ability to regenerate muscle cells is always in demand for the muscle tissue engineering application.

To achieve these goals, here, we have developed a musculoresponsive polymer−carbon composite for assisting in myotubular regeneration (MusCAMLR) by modulating the isotropic gelation behavior of a thermoresponsive polymer (PNIPAM) and tuning its gelation temperature closer to the physiological temperature (∼37 °C). PNIPAM is a widely studied polymer for mimicking the extracellular matrix, which is achieved at its gelation temperature of ∼32 °C, known as the lower critical solution temperature (LCST).[11,12] The aniso-tropic arrangement of actin and myosin in the sarcomere results in unidirectional stiffening using ATP as a source of energy.[12,13] Akin to this fact, the incorporation of PNIPAM-passivated carbon nanoparticles (CNP-PNIPAM) in the PNIPAM matrix generates MusCAMLR, which provides structural anisotropy at physiological temperature instead of using ATP as an energy source. Interestingly, this effect does not appear with incorporation of pristine carbon nanoparticles (CNPs). Furthermore, we have demonstrated the probable mechanical crosstalk between MusCAMLR and muscle cells including myoblasts and myotubes, its ability to maintain mechanical compatibility, regenerative potential, and unique
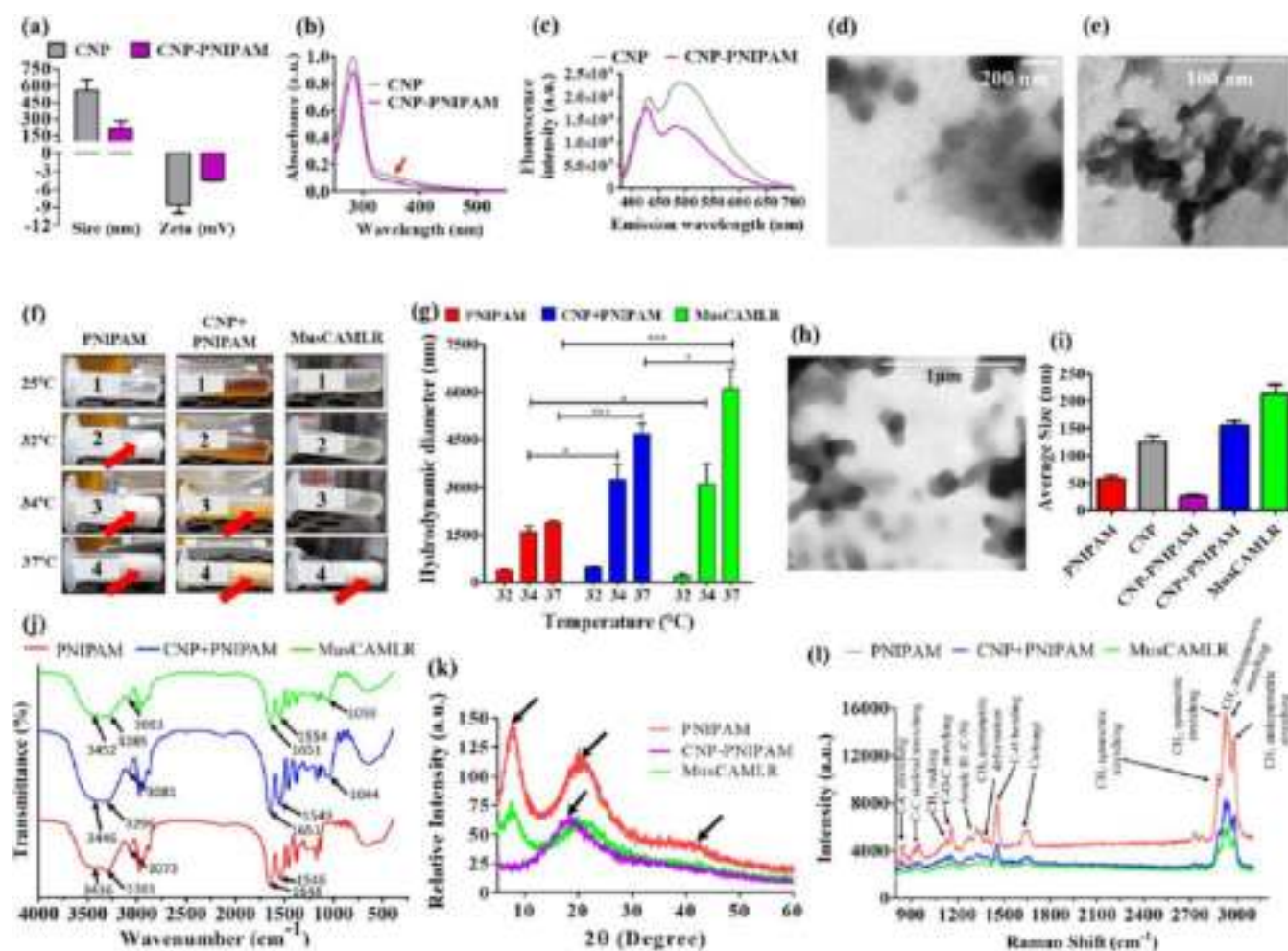
Figure 1. Preparation and characterization of MusCAMLR for physicochemical properties. (a) Hydrodynamic diameter and zeta potential of CNPs and CNP-PNIPAM. (b) UV−vis absorption spectra of CNPs and CNP-PNIPAM. The red arrow indicates the characteristic absorption of CNPs at ~360 nm. (c) Fluorescence emission spectra of CNPs and CNP-PNIPAM at an excitation wavelength of 360 nm. (d, e) TEM images of CNPs and CNP-PNIPAM. (f) Visualization of the tuned gelation pattern at different temperatures as a cue. (g) Temperature-dependent change in hydrodynamic size of PNIPAM, CNP + PNIPAM, and MusCAMLR samples. Biostatistical analysis represents *** significance with $P < 0.001$ and * significance with $P < 0.05$. (h) Anhydrous morphology of MusCAMLR in TEM investigation. (i) Analysis of the average size of PNIPAM, CNP, CNP-PNIPAM, CNP + PNIPAM, and MusCAMLR obtained from TEM images. (j) FTIR spectra of PNIPAM, CNP + PNIPAM, and MusCAMLR. (k) X-ray diffraction (XRD) patterns of PNIPAM, CNP-PNIPAM, and MusCAMLR. (l) Raman spectra of PNIPAM, CNP + PNIPAM, and MusCAMLR.

myotube morphology. Moreover, the intramuscular injection of MusCAMLR in the mechanically damaged skeletal muscles in an animal model revealed its potential to rescue the structural integrity and mechanical parameters of the damaged muscles within 72 h of application (Scheme 1).

RESULTS

For the preparation of MusCAMLR, as a bioresponsive network to support muscle tissue regeneration, a material with the property of generating a network similar to myotubes and responsiveness to physiological cues was needed. Among many of the possibilities, a physiological temperature-sensitive gel composite with the possibility of tuning the network support of muscle tissues on being mechanically damaged can be a biocompatible and potent alternative to the less effective and side effect-inducing conventional therapies.[14] This led to the selection of the modified PNIPAM composite with a network tunability cue closer to the physiological temperature,

which could be responsive to muscle tissue with faster recovery of mechanical damage in a specially developed animal model.

Preparation and Characterization of MusCAMLR. PNIPAM, as a temperature-sensitive polymer, is known to show isotropic gelation behavior at ~32 °C and thus fails to respond anisotropically toward the expansion−contraction-like behavior of skeletal muscles. To overcome these shortcomings, the gelation pattern of PNIPAM was tuned by incorporating an additive[15,16] for finding the anisotropic stiffening like the sarcomere of muscle tissues using physiological temperature as a cue. Among various possibilities, hydrophilic, biocompatible, and easily producible CNPs[17] were preferred as an additive, which due to their auto-fluorescent nature could make the system traceable by fluorescence imaging[17] as well. Furthermore, to improve on such interactions, a novel system of CNP-PNIPAM was synthesized during the preparation of MusCAMLR. CNPs were synthesized by a microwave-assisted hydrothermal method using sucrose as a carbon source.[17,18] CNP-PNIPAM particles were also prepared from sucrose
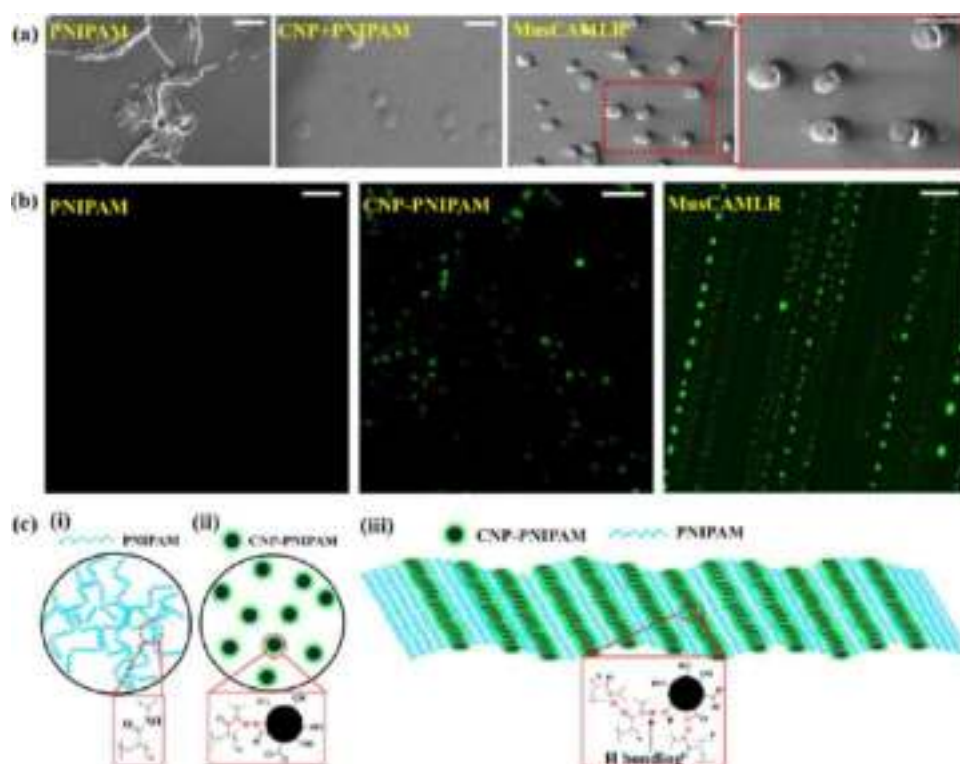
Figure 2. Structural anisotropy of MusCAMLR. (a) SEM images of PNIPAM, CNP + PNIPAM, and MusCAMLR. The red rectangle represents the area magnified for further details. Scale bar = 20 μm. (b) Confocal microscopic images of PNIPAM, CNP + PNIPAM, and MusCAMLR obtained at 37 °C. Scale bar = 10 μm. (c) Schematic representation of the arrangement network of (i) PNIPAM, (ii) CNP-PNIPAM, and (iii) MusCAMLR. The red dotted circle represents the probable arrangement of chemical entities present in different samples.

added with PNIPAM inside a pressure chamber by a similar method. The measurement of hydrodynamic diameter showed that the size of CNPs was ~556 ± 99 nm, which decreased to ~217 ± 63 nm in the case of CNP-PNIPAM (Figure 1a). Similarly, the ζ-potential of CNPs was found to be −9 mV, which reduces to −5 mV after passivation with PNIPAM, probably due to changes in the abundance of carboxylic acid groups on the surface (Figure 1a).[17,19] The analysis of ultraviolet−visible (UV−vis) absorption spectra showed the presence absorption maxima (λ_{max}) at 280 nm probably because of the $\pi-\pi^*$ transition and 360 nm due to the $n-\pi^*$ transition.[18] A reduction in absorption intensity at λ_{max} was found in the case of CNP-PNIPAM, probably due to masking of surface functionalities, which are known to be responsible for optical properties in CNPs (Figure 1b). Furthermore, fluorescence emission spectra of CNPs and CNP-PNIPAM were investigated upon excitation at their characteristic λ_{max} of 360 nm. It was found that the emission maximum of CNPs was ~490 nm, whereas in the case of CNP-PNIPAM, it shifted to ~470 nm with a reduction in emission intensity (Figure 1c). These characteristic optical properties indicate the successful synthesis of auto-fluorescent CNPs and CNP-PNIPAM, in which reduced hydrodynamic diameter and surface charge were reported.

Transmission electron microscopic (TEM) images represent the anhydrous morphology of CNP and CNP-PNIPAM (Figure 1d,e) with an average size of ~126 ± 11 and ~26 ± 3 nm, respectively (Figure 1i). Other composites were prepared by adding CNP to PNIPAM (80 mg/mL) solution to tune its LCST and subsequently followed the gelation behavior. It was observed that addition of CNP (20 mg/mL)

results in tuning of gelation from ~32 to ~34 °C, and this combination was called as CNP + PNIPAM (Figure 1f). This indicates the increase in the LCST of PNIPAM from 32 to 34 °C and maintained the gel form even at a higher investigated temperature of 37 °C. To achieve the LCST close to 37 °C, instead of adding CNP, a nanosystem, CNP-PNIPAM, was incorporated in the PNIPAM solution. Intriguingly, incorporation of 20 mg/mL CNP-PNIPAM could tune the LCST of PNIPAM (80 mg/mL) close to the physiological temperature (~37 °C). This combination of CNP-PNIPAM and PNIPAM was called as MusCAMLR. It also showed maximum reversible transition of hydrodynamic diameter in accordance with the increase in temperature as a stimulus (Figure 1g). The anhydrous morphology from the images obtained by TEM revealed that MusCAMLR was nearly spherical in morphology with a diameter of ~214 ± 13 nm (Figure 1h,i), whereas the average anhydrous size of PNIPAM and CNP + PNIPAM was ~59 ± 5 and 155 ± 9 nm, respectively (SI Figure S1a,b). The UV−vis absorption spectra of PNIPAM, CNP + PNIPAM, and MusCAMLR showed a temperature-dependent increase in absorbance (SI Figure S2), which was because of higher gelation resulting in increased scattering of the light in the range of investigated wavelengths. Furthermore, Fourier transform infrared (FT-IR) spectra were recorded to evaluate the interactions of CNP and CNP-PNIPAM with PNIPAM in the respective composites (Figure 1j). The analysis of spectral characters revealed the presence of all characteristic bands of N−H bending, C═O stretching, N−H stretching vibrations, etc., in PNIPAM. Transmittance peaks of PNIPAM at 1546 and 1648 cm^{-1} represent the N−H bending of amide II and C═O stretching of amide I, respectively,[20,21] which were
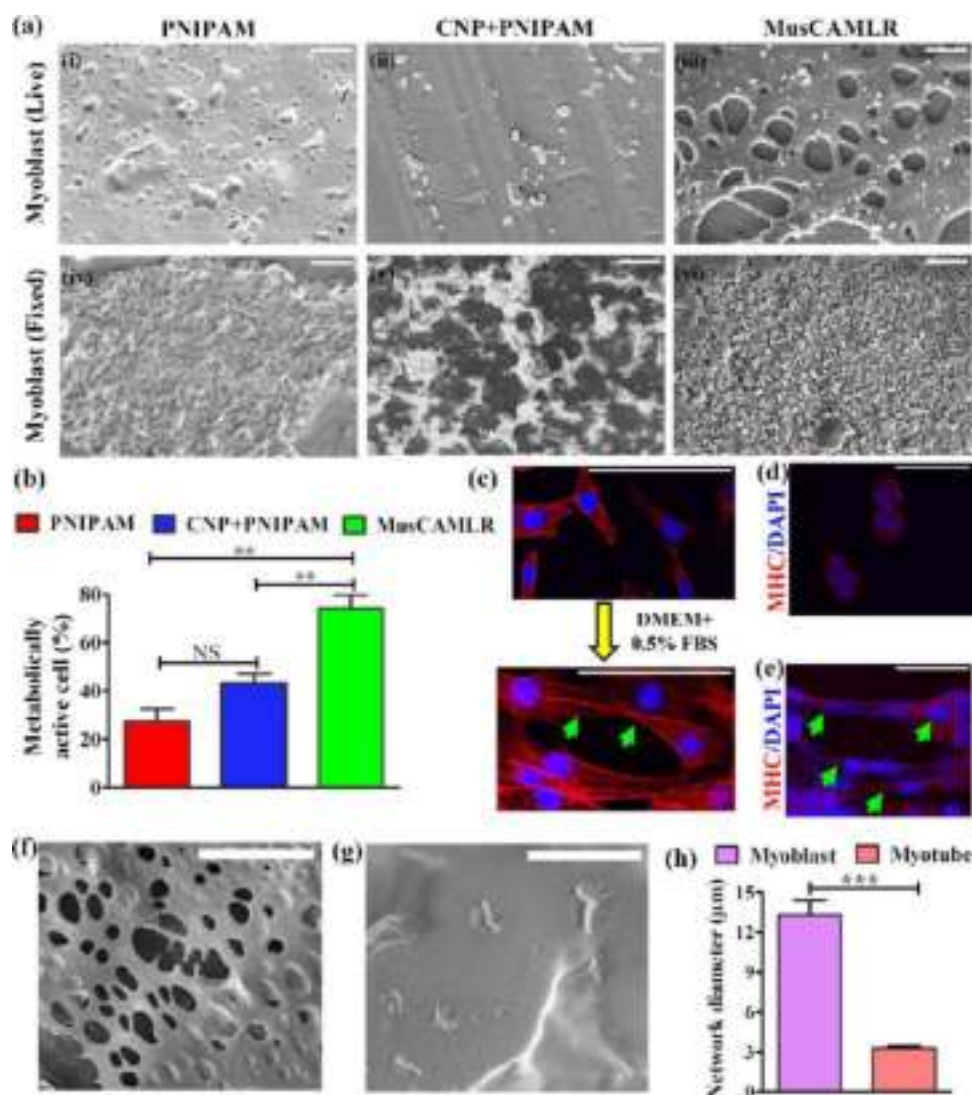
D

Figure 3. Interaction of MusCAMLR with muscle cells. (a) SEM images of (i) PNIPAM, (ii) CNP+PNIPAM, and (iii) MusCAMLR in interaction with live myoblast cells. SEM images of (iv) PNIPAM, (v) CNP+PNIPAM, and (vi) MusCAMLR in interaction with fixed myoblast cells. Scale bar = 20 μm. (b) Measurement of metabolically active cells present in interaction with different samples. Biostatistical analysis represents ** = significance with $p < 0.001$ and NS = not significant. (c) Myoblast to myotube differentiation as observed by staining with Alexa Flour 594-phalloidin. Scale bar = 100 μm. MHC-stained confocal microscopic image of (d) myoblast and (e) myotube. Scale bar in (d, e) = 100 μm. (f) SEM images of the MusCAMLR interaction with myotube. Scale bar = 20 μm. (g) SEM images of the MusCAMLR interaction with the NIH/3T3 cell line. Scale bar = 20 μm. (h) Analysis of network diameter of MusCAMLR produced after interaction with myoblasts and myotube. Biostatistical analysis represents *** = significance with $p < 0.0001$.

shifted to higher wavenumbers of 1549 and 1651 cm^{-1} in the case of CNP + PNIPAM and 1554 and 1651 cm^{-1} for MusCAMLR. Similarly, transmittance peaks of PNIPAM at 3073, 3301, and 3436 cm^{-1} indicate N−H stretching of secondary amides,[20] which was shifted to 3081, 3296, and 3446 cm^{-1} in the case of CNP + PNIPAM and 3083, 3285, and 3452 cm^{-1} in the case of MusCAMLR. These shifts of infrared (IR) bands to higher wavenumber were probably because of the hydrogen bonding interaction between CNP and PNIPAM, which was more in MusCAMLR due to the presence of CNP-PNIPAM. Furthermore, the appearance of a new peak at 1044 cm^{-1} in the CNP + PNIPAM composite represents the C−O stretching of primary alcohol present on the incorporated CNP.[17] This peak was shifted to 1059 cm^{-1} in MusCAMLR, probably because of its involvement in hydrogen bonding with PNIPAM. The X-ray diffraction (XRD) pattern of PNIPAM showed its characteristic

diffraction peak at 2θ = 7.5 and 20.5° and a small hump at 41.3°. The diffraction peak of CNP-PNIPAM was found at 2θ = 18°. However, in the case of MusCAMLR, the diffraction peaks were found at 2θ = 7.5, 20.5°, while the diffraction peak of CNP-PNIPAM and the small hump at 41.3° completely disappeared. This indicates probably the successful penetration of CNP-PNIPAM inside the PNIPAM polymer matrix (Figure 1k).[22] A similar observation was also obtained in CNP + PNIPAM (SI Figure S1c), where it showed a diffraction peak at 2θ = 7.5, 20.5, and 40.9° with the disappearance of the diffraction peak of CNP at 2θ = 18°. The calculated d spacing values of PNIPAM, CNP + PNIPAM, and MusCAMLR at different diffraction angles (2θ) are provided in SI Table.S1, supporting the same conclusion of incorporation of CNP and CNP-PNIPAM in the PNAIPAM network. Raman spectroscopic characterization as represented in Figure 1l with the allocation of all vibrational modes[23,24] showed a decrease in
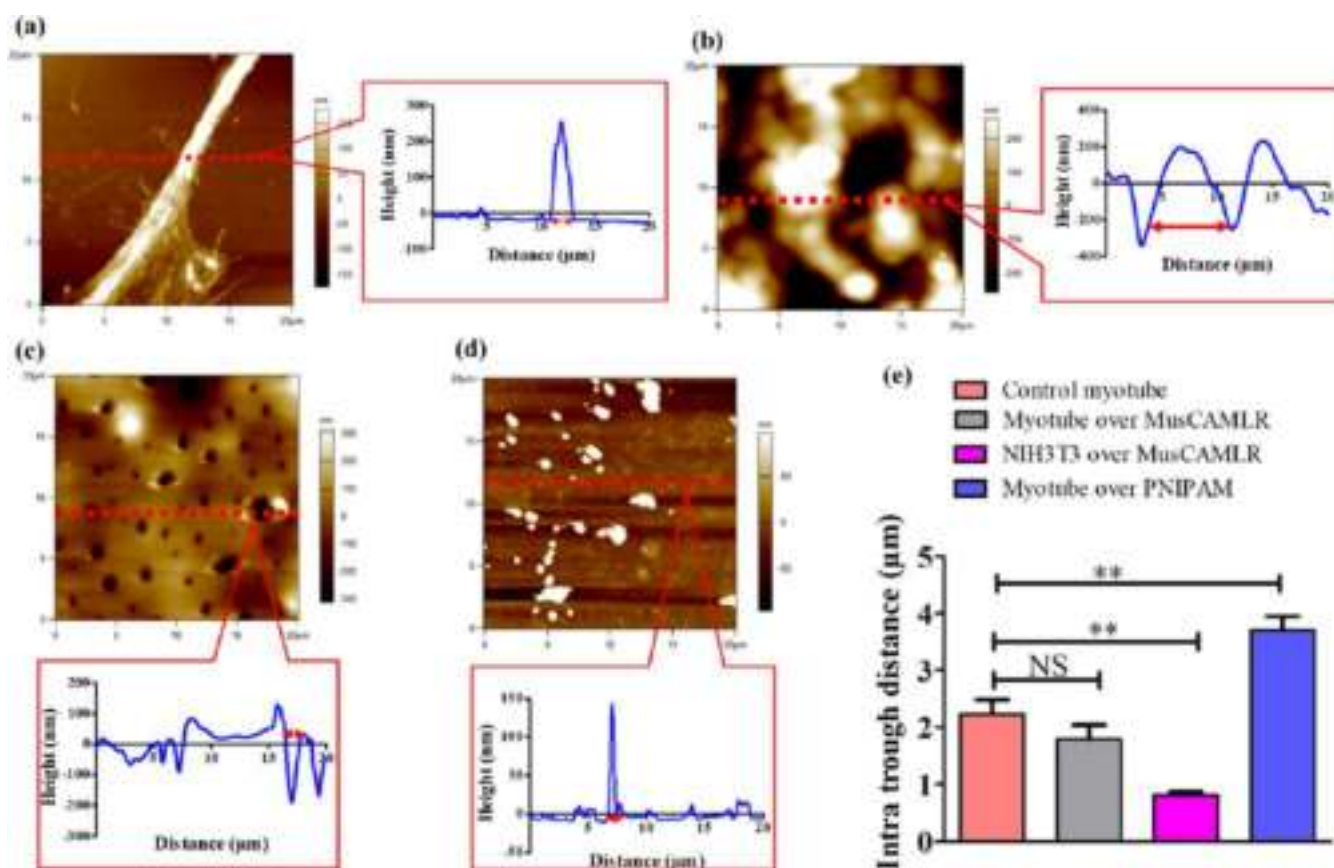
Figure 4. AFM images and representative surface profile plot of (a) control myotube, (b) interaction of PNIPAM with the myotube, (c) interaction of MusCAMLR with the myotube, and (d) interaction of MusCAMLR with NIH/3T3 cells. The double-headed red arrow indicates the intratrough distance in the surface profile plot in (a–d). (e) Measurement of intratrough distance from analysis of the surface profile in (a–d). Biostatistical analysis represents ** = significance with $p < 0.001$ and NS = not significant.

the intensity in CNP + PNIPAM, which was further decreased in the case of MusCAMLR with respect to PNIPAM. This indicates the interaction of CNP with PNIPAM, which was further increased after addition of CNP-PNIPAM with PNIPAM (MusCAMLR).[25]

The evaluation of surface morphology showed an uncontrolled surface arrangement of PNIPAM without any specific pattern of growth, which was transformed to sphere-like arrangement over the surface after addition of CNP. Interestingly, incorporation of CNP-PNIPAM produces very controlled and repetitive sandwich-like projection over the surface of MusCAMLR (Figure 2a). This indicated the anisotropic surface topography of MusCAMLR. To further explore the phenomenon of anisotropic expansion, temperature-dependent confocal microscopic investigation was carried out by exploiting the fluorescence property of CNP and CNP-PNIPAM. It was hypothesized that CNP or CNP-PNIPAM should arrange itself according to the orientation of the PNIPAM matrix at 37 °C, if an anisotropic expansion had to happen in the network. It was found that indeed, these CNP-PNIPAM particles were arranged linearly in the longitudinal direction (Figure 2b), ensuring the anisotropic expansion phenomenon in MusCAMLR, which started appearing after ∼3 min of exposure to 37 °C (SI Figure S3), whereas CNP particles were arranged in a different manner in the case of CNP + PNIPAM (SI Figure S1d). The representative structures of MusCAMLR and CNP+PNIPAM

based on the aforesaid investigation are shown in Figures 2c and S1e, respectively.

Evaluation of MusCAMLR's Interaction with Muscle Cells. Scanning electron microscopy (SEM)-based investigation was performed on different frameworks to visualize the interaction of muscle cells with PNIPAM, CNP + PNIPAM, and MusCAMLR. In the first set of experiments, C2C12 myoblasts were grown over a surface coated with PNIPAM, CNP + PNIPAM, and MusCAMLR. Interestingly, a network-like structure was found over the surface of MusCAMLR (Figure 3aiii), which was significantly different from the morphology appearing either in PNIPAM or CNP + PNIPAM samples (Figure 3ai,aii). Bright-field microscopic images also indicated the network formation over the surface of MusCAMLR, when C2C12 myoblasts were grown over it (SI Figure S4). It was hypothesized that this distinguishable network-like structure appeared over the surface of Mus-CAMLR as a signature of mechanical interactions when cells were alive and growing. To test this hypothesis, another set of experiments were designed where fixed C2C12 myoblast cells were subsequently mixed with PNIPAM, CNP + PNIPAM, and MusCAMLR, in different samples. Here, none of the samples presented network-like structures as seen in SEM investigations (Figure 3aiv–avi). These experiments proved the impact of mechanical interactions of live cells to change the morphology of the prepared samples. A thiazolyl blue tetrazolium bromide (MTT)-based assay was performed after growing the cells in similar conditions over PNIPAM-, CNP +
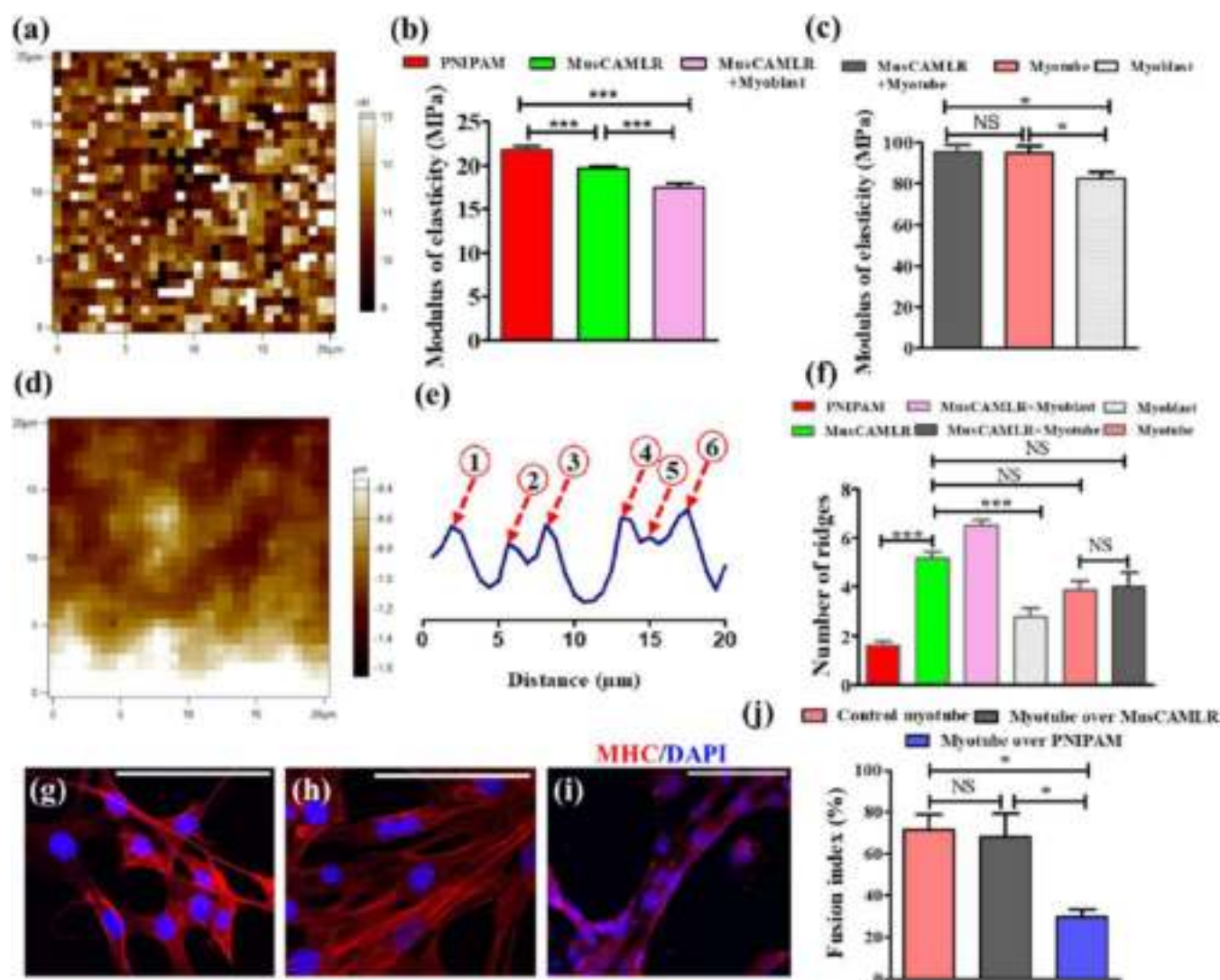
F

Figure 5. Mechanical compatibility and differentiation ability of muscle cells on the surface of MusCAMLR. (a) Force map of MusCAMLR obtained from AFM investigation. (b) Analysis of the modulus of elasticity from the AFM force map of PNIPAM, MusCAMLR, and myoblast grown over MusCAMLR (MusCAMLR + Myoblast). Biostatistical analysis represents *** = significance with $p < 0.0001$. (c) Analysis of modulus of elasticity from the AFM force map of myotubes grown over MusCAMLR (MusCAMLR + myotube), myotube, and myoblast alone. Biostatistical analysis represents * = significance with $p < 0.01$ and NS = not significant. (d) Force−height map obtained from MusCAMLR. (e) Representative surface force−height profile as obtained from MusCAMLR. Red arrows indicating the number of ridges over the surface of the material. (f) Calculation of the average number of ridges from the surface force−height profile of PNIPAM, MusCAMLR, MusCAMLR + myoblast, MusCAMLR + myotube, control myoblast, and control myotube. Biostatistical analysis represents *** = significance with $p < 0.0001$ and NS = not significant. (g) Confocal microscopic images of myotubes by staining with Alexa Flour 594-phalloidin over the surface of PNIPAM and (h) MusCAMLR. Scale bar in (g, h) = 100 μm. (i) MHC-stained confocal microscopic image of myotubes differentiated over MusCAMLR. Scale bar = 100 μm. (j) Measurement of fusion index. Biostatistical analysis represents * = significance with $p < 0.01$ and NS= not significant.

PNIPAM-, and MusCAMLR-coated surfaces to further support this observation. It was found that a significantly higher percentage (∼75%) of myoblast cells were metabolically active when grew over the MusCAMLR surface compared to PNIPAM- or CNP + PNIPAM-coated surfaces (Figure 3b). This investigation deciphered that the network-like surface morphology formed over the surface of MusCAMLR was probably because of the mechanical interaction of growing myoblasts cells in the presence of MusCAMLR.

The myogenic potential of C2C12 myoblasts was utilized to generate myotubes and used further to explore this interaction. This differentiated system was utilized because of its resemblance with the myofiber of skeletal muscles, and results could provide enough indication about the response of

MusCAMLR *in vivo*.[26] Alexa Flour 594-phalloidin-stained confocal microscopy images of the C2C12 cells grown for 7 days in differentiation medium revealed elongated cytoskeletal morphology and thus ensured the myotube differentiation (Figure 3c).[27] The expression of the myosin heavy chain (MHC) is a marker required for differentiation of myoblasts to form multinucleated myotubes.[28−30] The immunostained differentiated myotubes were investigated by using the MHC antibody after examining the cytoskeletal morphology. The appearance of multiple nucleated tubes having comparatively intense fluorescence intensities with respect to the myoblast ensures the differentiation (Figure 3d,e). Induced myotube differentiation over a MusCAMLR-coated surface was subjected to SEM investigation and found to have a
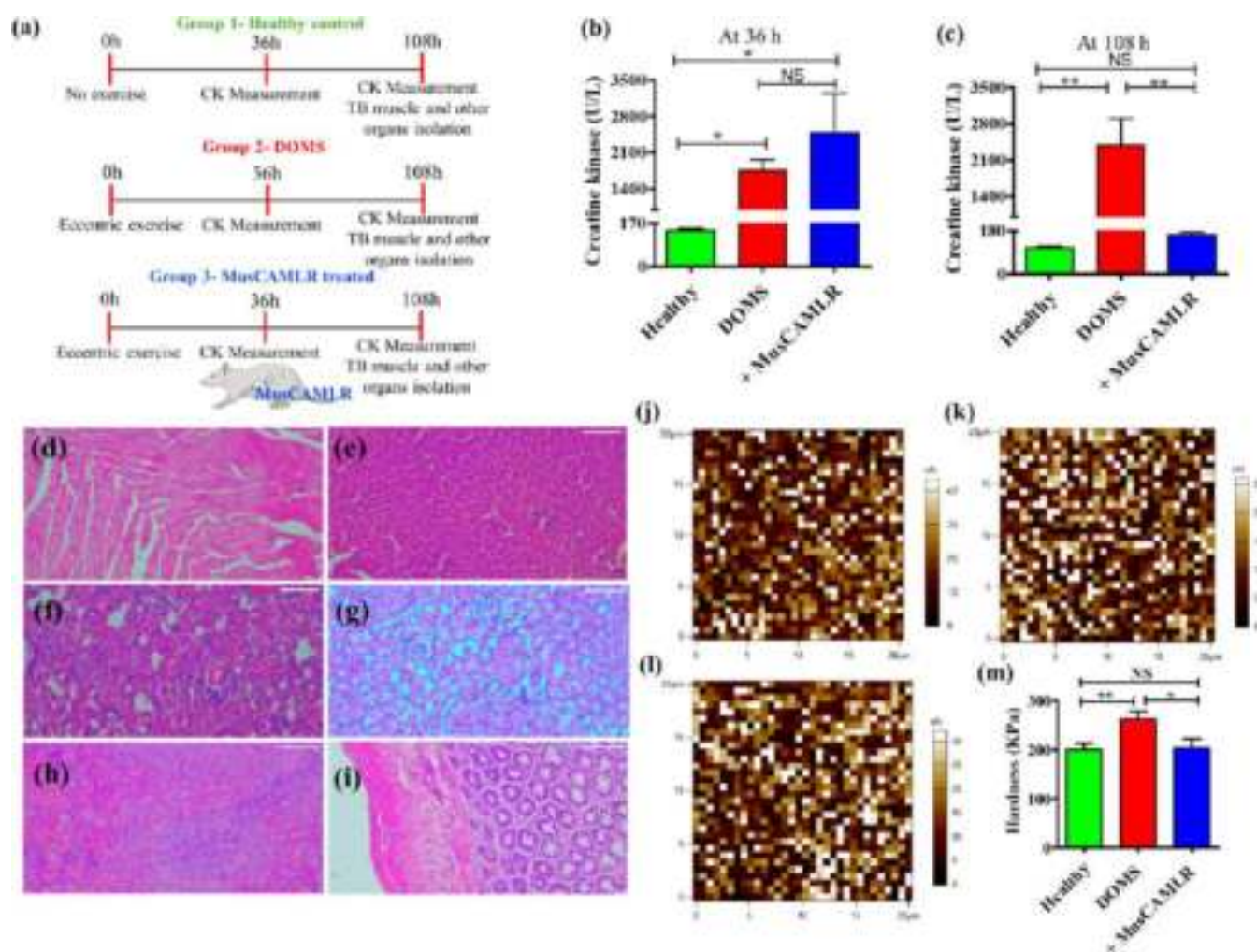
Figure 6. *In vivo* application of MusCAMLR on mechanically damaged skeletal muscle (DOMS) animal model. (a) Schematic representation of the timeline for eccentric exercise, CK measurement, MusCAMLR treatment, and excision of different organs from animals of three different groups. (b) Serum creatine kinase level at 36 h (before application of MusCAMLR) and (c) at 108 h (i.e., 72 h after application of MusCAMLR). Biostatistical analysis represents ** = significance with $p < 0.002$, * = significance with $p < 0.01$ and NS = not significant. (d) H&E-stained microscopic images of the heart, (e) liver, (f) lung, (g) kidney, (h) spleen, and (i) intestine. Scale bar in (d, e) = 100 μm. (j) Force map of muscle tissue from healthy, (k) DOMS, and (l) MusCAMLR-treated animals. (m) Analysis of tissue hardness from the force maps of healthy, DOMS, and MusCAMLR-treated animals. Biostatistical analysis represents ** = significance with $p < 0.01$, * = significance with $p < 0.05$, and NS = not significant.

network-like surface morphology (Figure 3f) with a significantly reduced diameter in comparison to the network formed in the presence of myoblasts (Figure 3h). It was important to investigate whether this network formation is specific to muscle cells or promiscuous in nature. To answer this question, fibroblast cells were chosen as control cells. They provide a right control due to their presence as integral resident cells in skeletal muscles.[31] NIH/3T3 mouse fibroblast cells were grown over a MusCAMLR-coated surface for electron microscopy studies. The SEM investigation revealed that there was no network formation in the presence of NIH/3T3 cells (Figure 3g). This study confirmed that the network formation was peculiar and specific to muscle cells in cellular and differentiated states (myoblasts and myotubes). Evaluation of these samples by atomic force microscopy (AFM) as represented in Figure 4a−d and the analysis of the surface profile (SI Figures S5−S8) revealed that the average intratrough distance over the surface of the myotube grown over MusCAMLR was equivalent to control myotubes grown

on regular cell culture plate surfaces, whereas myotubes grown over PNIPAM or NIH/3T3 grown over MusCAMLR was not of any significant similarity (Figure 4e).

Mechanical Similarity and Myoblast Differentiation Ability of MusCAMLR. In general, success of a material prepared for biological applications would depend on the structural and functional similarity with the biological tissue of concern. Here, as skeletal muscles are the tissues in focus, to ensure the mechanical similarity of MusCAMLR with muscle tissue, which would be required to make it suitable for better interactions by being in a similar biological scenario, nanomechanical analysis was performed using an AFM-based nanoindentation technique. It was found from the force mapping analysis of PNIPAM (SI Figure S9a), MusCAMLR (Figure 5a), and myoblasts grown over MusCAMLR (SI Figure S9b) that the modulus of elasticity was significantly low in the case of MusCAMLR and further decreased when myoblasts were grown over MusCAMLR, with respect to PNIPAM (Figure 5b). The force mapping analysis of myotube
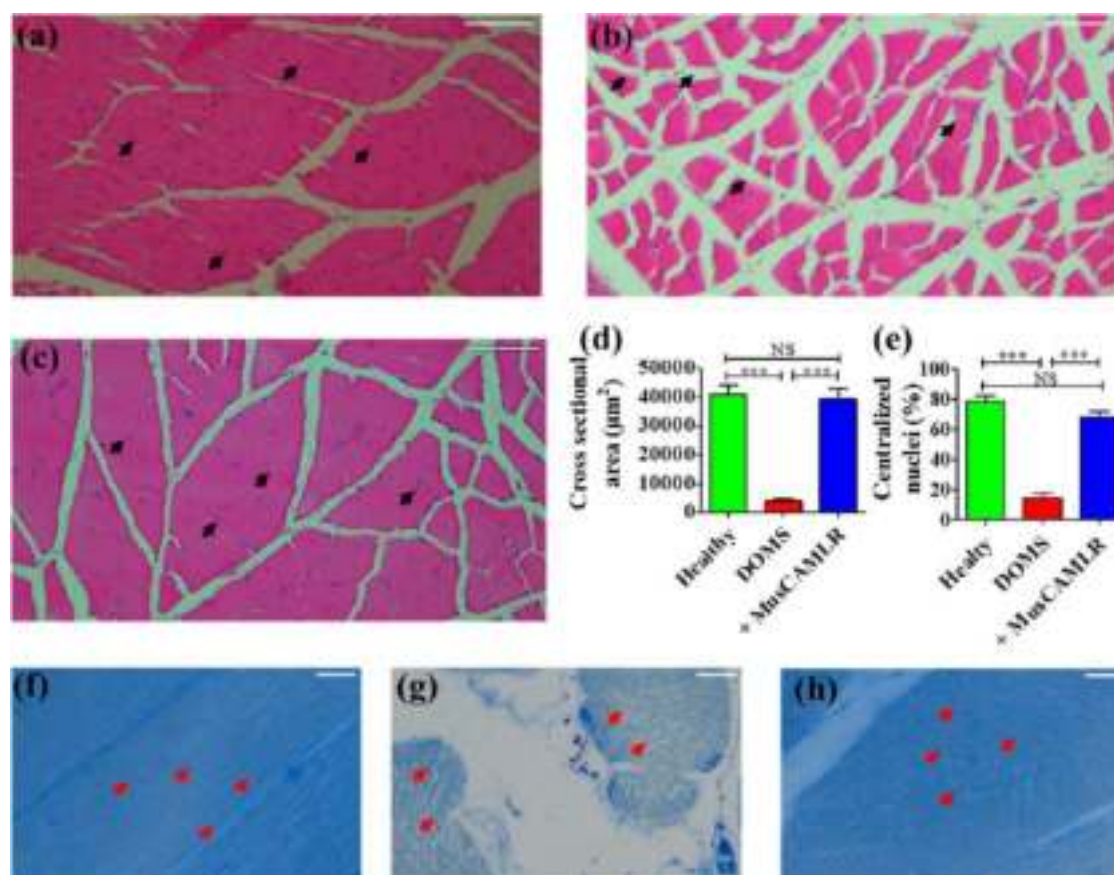
Figure 7. Recovery of structural integrity of skeletal muscles after MusCAMLR treatment. Representative H&E-stained cross-section of TB muscle from (a) healthy, (b) DOMS, and (c) MusCAMLR-treated animals. Scale bar in (a, c) = 100 μm. Black arrows indicate the location of nuclei. (d) Calculated cross-sectional area from the cross-sections of TB muscle. (e) Percentage of centralized nuclei from the cross-sections of TB muscle. (f) Representative toluidine blue-stained longitudinal sections of TB muscle from healthy, (g) DOMS, and (h) MusCAMLR-treated group. Scale bar in (f−h) = 10 μm. Red arrows indicating the demarcation of the sarcomere. Biostatistical analysis represents *** = significance with $p < 0.0001$ and NS = not significant.

differentiated over MusCAMLR gives an equivalent modulus of elasticity as control myotubes, which was significantly different from the modulus of elasticity of myoblasts (Figures 5c and S9c−e). This study interprets the excellent mechanical compatibility of myotube differentiated over the surface of MusCAMLR. The analysis of force−height map of Mus-CAMLR (Figure 5d,e), PNIPAM, myoblasts grown over MusCAMLR, myotubes grown over MusCAMLR, control myotubes, and control myoblasts (SI Figures S10a−e and S11) deciphered that the average numbers of ridges over the surface of MusCAMLR, myotubes grown over MusCAMLR, and control myotubes were almost the same (Figure 5f). This dictated that the spatial range of force was of the same order; thus, high complementarity could be excepted for the functioning of the material. Furthermore, an evaluation was performed for the differentiation ability of myoblasts over the surface of PNIPAM and MusCAMLR by visualizing the cytoskeletal morphology and quantifying the fusion index as a measure of extent for the myotube differentiation process. Confocal microscopic investigation by staining with Alexa Flour 594-phalloidin showed that the myotube differentiated over the surface of MusCAMLR (Figure 5h) indeed gives better elongated cytoskeletal morphology than the myotube differentiated over the surface of PNIPAM (Figure 5g). Furthermore, immunocytochemical investigation using the anti-MHC antibody showed the generation of multinucleated

tubes with comparatively higher fluorescence intensity over MusCAMLR (Figure 5i) with respect to PNIPAM (SI Figure S12). Analysis of microscopic images obtained by Giemsa staining (SI Figure S13) showed that myotubes differentiated over the surface of MusCAMLR had a very high fusion index, which was equivalent to values from control myotubes, whereas myotubes grown over the PNIPAM surface had a significantly lower fusion index. It could be interpreted that MusCAMLR could better maintain the differentiation of myoblasts *in vitro* (Figure 5j).

***In Vivo* Application of MusCAMLR on Mechanically Damaged Skeletal Muscles in the Developed Animal Model.** For examining the role of MusCAMLR in rescuing mechanically damaged skeletal muscles, a delayed onset muscle soreness (DOMS) animal model was developed using eccentric exercise as a mechanical stimulus.[32] Since eccentric exercise leads to lengthening of muscle fibers, this kind of muscle damages is also known as strain injuries, which result in disruption of contractile elements of muscle fibers, leakage of muscle proteins in plasma, activation of immune responses, and reduction of muscle performance.[33,34] Measurement of serum creatine kinase (CK) before and after application of MusCAMLR and measurement of other tissue parameters were carried out as per the timeline represented in Figure 6a. It was found that the serum CK level increases significantly at 36 h after the induction of muscle damage in group 2 (DOMS
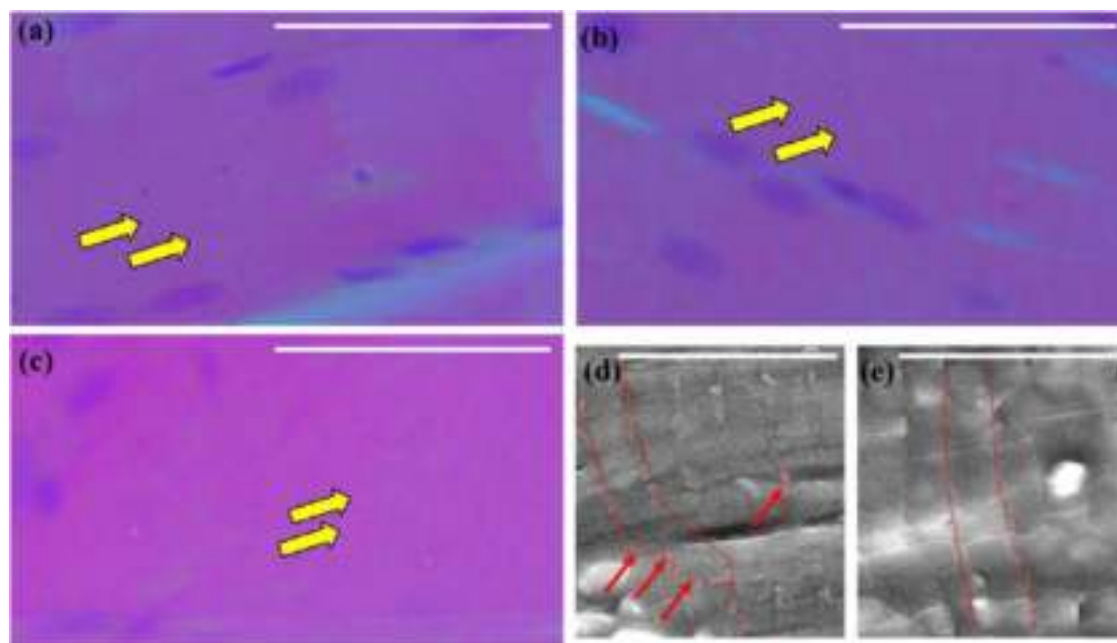
Figure 8. Arrangement of sarcomere in the longitudinal section of skeletal muscles. H&E-stained longitudinal section of skeletal muscles from (a) healthy group, (b) DOMS group, and (c) MusCAMLR-treated group. Yellow arrows (a–c) indicating the demarcation of the sarcomere's lining and scale bar = 50 μm. Representative SEM images of the sarcomere from the longitudinal section of the animals of (d) DOMS and (e) MusCAMLR-treated group. The red line (d, e) represents demarcation of the sarcomere; red arrows indicate the diffused structure of the Z-line and scale bar = 20 μm.

group) and group 3 (MusCAMLR-treated group) before the application of MusCAMLR (Figure 6b). It was observed that the intramuscular injection of MusCAMLR in the triceps brachii (TB) muscle resulted in the recovery of serum CK levels within 72 h of application, i.e., at a time point of 108 h (Figure 6c). After these observational time points, animals were sacrificed and investigated for biocompatibility of MusCAMLR by using hematoxylin and eosin (H&E) staining of different vital organs including the heart, liver, lung, kidney, spleen, and intestine. As results suggest, no significant sign of toxicity, immune activation, and other adverse effects of the tissues were noted (Figure 6d–i). A similar observation was also prominent from H&E-stained images of different organs (heart, liver, lung, kidney, spleen, intestine) from the DOMS and healthy groups of animals (SI Figures S14 and S15). This indicated the noticeable biocompatible nature of MusCAMLR. The analysis of force map data from muscle tissues of healthy, DOMS, and MusCAMLR-treated animal groups (Figure 6j–l) showed a significant increase in tissue hardness in the TB muscle of the DOMS group,[35] which was reduced to the normal level within 72 h after treatment of MusCAMLR (Figure 6m).

Recovery of the Structural Integrity of Skeletal Muscle. To evaluate the ability of MusCAMLR to rescue the structural alteration in mechanically injured muscles, both cross-sections as well as longitudinal sections of TB muscles were analyzed. Analysis of the muscle cross-section by H&E staining (Figure 7a–c) revealed that the cross-sectional area (Figure 7d) and the percentage of centralized nuclei (Figure 7e) were reduced significantly in damaged muscles of the DOMS group. This implied the induced atrophy of the damaged muscle,[36] which was rescued after application of MusCAMLR. To further evaluate the Z line streaming, toluidine blue staining,[33] H&E-staining, and electron micro-scopic investigation from the longitudinal section of TB muscle

were executed. Toluidine blue-stained images obtained from healthy TB muscle (Figure 7f) showed very distinct and demarcated boundaries of the sarcomere, which was disrupted and diffused in the mechanically damaged TB muscle from the DOMS group, indicating the Z-disk disruption (Figure 7g). The recovery of demarcated prominent boundaries of the sarcomere after MusCAMLR treatment denotes the rescuing of structural integrity of TB muscles (Figure 7h). The H&E-stained images of the longitudinal section of skeletal muscles also showed disruption of the regular arrangement of the sarcomere in the muscle from the DOMS group, possibly because of Z-line streaming. It was found to be rescued after MusCAMLR treatment (Figure 8a–c). A similar observation was also achieved from the images obtained through SEM and TEM investigations (Figures 8d,e, and S16).

■ DISCUSSION

This study demonstrates the modulation of isotropic gelation behavior of PNIPAM[37] to prepare nondrug MusCAMLR for efficiently rescuing the mechanically damaged skeletal muscles. It was found that the PNIPAM matrix could attain structural anisotropy by incorporation of CNP-PNIPAM-like physio-logical conditions of the anisotropic orientation in the skeletal muscles. The avoidance of complex tools such as thermally induced phase separation, 3D printing, etc., to prepare anisotropic scaffolds[13,38] and chemical conjugation to tune the physiological responses, e.g., co-polymerization with different polymers, ionic liquids in the presence of nanoparticle systems,[16,39] etc., brought wonderful ease in the PNIPAM-based gel system, MusCAMLR. The reversible expansion–contraction of hydrodynamic diameter indicates the possible primary mechanism of interaction with myofibers at physiological temperature (Figure 1g). The sandwich-like surface morphology of MusCAMLR provides

the hands-on proof of structural anisotropy and the influence of CNP-PNIPAM as an additive for controlling the material morphology (Figure 2a). The fluorescence property of CNP-PNIPAM in the PNIPAM matrix of MusCAMLR enabled the orientation to the whole system, which is expected to strengthen the most anticipated way of expansion to support longitudinally arranged myofibers (Figure 2b). A remarkable change in the surface morphology, i.e., from a sandwich-like surface to a special material network in the presence of growing myoblasts (Figure 3aiii), was perhaps because of the transmission of force during cytoskeletal organization, transcellular adhesion, etc.[41] Although a significant change in the surface morphology was observed even in the case of PNIPAM and CNP + PNIPAM (Figure 3ai,aii), MusCAMLR was found to have the best cell viability (Figure 3b) and anisotropic features. A similar network structure with a different network diameter also appeared in the presence of differentiated myotubes (Figure 3f). AFM-based force mapping investigation showed that the force–height profile of PNIPAM and MusCAMLR was different, which in turn governs the differences in the spatial range of acting forces (Figure 5f). Similarly, the differences in the force–height profile of MusCAMLR with myoblasts and similarity with myotubes probably decipher its suitability to interact mechanically with myotubes. Presumably, similarity and dissimilarity of Mus-CAMLR with myotubes and myoblasts, respectively, with respect to the experienced mechanical forces could be the reason behind the formation of special material networks with different diameters. Properly elongated cytoskeletal morphology and mechanical compatibility of myotubes ensure the competence of MusCAMLR to support the myotube growth. It became only possible because of the anisotropic feature of MusCAMLR. The development of the in vivo mechanically damaged muscle model is generally carried out by using drugs, snake venom like cardiotoxin, and other genetically diseased models,[42,43] which causes extensive damage of myofibers. Here, the purpose of the development of eccentric exercise-induced DOMS model was to mimic the real-life scenario (Figure 6a, and SI video S1).[44] The TB muscle was chosen for the application of MusCAMLR, as it is an extensor muscle and shows a greater extent of damage after downhill running.[45] The recovery of structural parameters, e.g., serum CK level, muscle cross-sectional area, hardness, etc., upon insertion of MusCAMLR into the TB muscle proved its potential to rescue damaged muscles probably by supporting proliferation and differentiation of resident myoblasts, as was seen in vitro. An easy method of preparation, simpler in vivo delivery through intramuscular injection, highly promising outcome in terms of restoring the structural and mechanical properties in a mechanically damaged DOMS model makes the MusCAMLR system beneficial for wider skeletal muscle applications. These results establish the possible potential of MusCAMLR to rescue patients with higher extent muscle damages that occurred due to various reasons. Further investigation with this system can lead to the development of a nondrug alternative therapeutic tool for the treatment of patients with muscular dystrophy, etc. Ultimately, the outcomes of the experiments presented here clearly demonstrate that the engineered MusCAMLR is capable of supporting the growth, differentiation of myoblasts, and further recovery of the damaged muscles. The excellent mechanical compatibility and tuned anisotropic properties of the MusCAMLR also provide a direction toward the goal of achieving muscular

mimics. To the best of our knowledge, the nanocarbon-enforced anisotropic MusCAMLR reported in the article is a novel material as a nondrug therapeutic alternative for the treatment of mechanically damaged DOMS model. The conventional treatment strategies of DOMS generally include cryotherapy, application of electric stimulation, use of ultrasounds, and use of anti-inflammatory drugs, especially NSAIDs.[46−50] However, the pain perception was not found to be associated with the extent of skeletal muscle damage.[2] Although NSAIDs were found to reduce the soreness and pain sensation to some extent, their ability to rescue the damaged muscle microstructure is not well established.[46,47,51,52] Considering these established facts, we did not find suitable gold-standard treatment controls for comparing the efficiency of MusCAMLR in the DOMS model. We also believe that the use of any of the presently used interventions would most likely be not beneficial to compare the recovery of structural integrity of skeletal muscles. However, we will be considering some of these controls for our future studies where the functional outcome of MusCAMLR will be the primary objective.

■ CONCLUSIONS

The primary criterion for a biomaterial to be used in the skeletal muscle tissue engineering application is the ability to firmly hold the longitudinally aligned myofibers and facilitate their regeneration. For such an application, anisotropic materials are desirable, as they achieve a closure mimic of the native skeletal muscle tissue. Although various hydrogels are widely being applied for multiple bioengineering applications, the isotropic gelation pattern limits their utility in skeletal muscle tissue engineering. The outcomes of the experiments presented here clearly demonstrate that the optimized amount of hydrophilic nanosized carbon particles with specific surface passivation can influence the gelation pattern of the PNIPAM hydrogel without any covalent chemical conjugation. This wonderful ease in the preparation methodology decreases the possibility of batch-to-batch variation and thereby enhances the probability of translation. Transition of surface morphologies, e.g., sandwich-like structure to a distinguishable material network in the presence of muscle cells, ensures responsiveness of the MusCAMLR to biological cues. We believe that careful modulation of isotropic gelation of PNIPAM enables engineered MusCAMLR to support the growth and differentiation of myoblasts and further recover the damaged muscles. The excellent mechanical compatibility and tuned anisotropic properties of the MusCAMLR also provide a direction toward the goal of achieving muscular mimics.

■ METHODS

Materials. Poly(N-isopropyl acrylamide) (PNIPAM; average molecular weight (M_n) = ~40,000) was purchased from Sigma-Aldrich. Sucrose (molecular weight (M_w) = 342.30) was purchased from Merck Life Science, India.

Synthesis of CNPs and CNP-PNIPAM. Carbon nanoparticles (CNPs) were synthesized by a hydrothermal method[17,18] using 10% (w/v) sucrose in 50 mL of Milli-Q water ($0.2 \times 10^{−6}$ m, 18 MΩ·cm) using a microwave−ultrasonic−ultraviolet synthesis/extraction/reactor system (Nu-Tech, Model: NuWav- Pro, India) at a temperature of 130 °C and power of 200 watt for 1 h. CNP and PNIPAM copreparation, i.e., CNP-PNIPAM, was carried out by adding 0.1% (w/v) PNIPAM with 10% (w/v) sucrose in 20 mL of Milli-Q water at 150 °C temperature for 45 min under 130 watt power inside the

pressure chamber of the microwave−ultrasonic−ultraviolet synthesis/extraction/reactor system.

Preparation of the Polymer−Carbon Composites CNP + PNIPAM and MusCAMLR. The sample of CNP + PNIPAM was prepared by mixing of CNP with PNIPAM (1:4; w/w) in 5 mL volume of Milli-Q water. The sample of MusCAMLR was prepared by mixing ∼same ratio of CNP-PNIPAM with PNIPAM in 5 mL volume of Milli-Q water.

Temperature-Dependent Dynamic Light Scattering (DLS). A Nanoseries Malvern Zetasizer particle analyzer was used to obtain the hydrodynamic diameter of PNIPAM, CNP, CNP + PNIPAM, and MusCAMLR. The average hydrodynamic diameter was taken from the peak values of size distribution by intensity at 32, 34, and 37 °C temperature.

Measurement of ζ-Potential. The ζ-potential was measured using a Malvern Zetasizer particle analyzer at 25 °C.

Transmission Electron Microscopy (TEM) Study. Samples were dropcast on a copper-coated carbon film grid and allowed to dry overnight. The same grid was subjected to transmission electron microscopy (TEM; Technai120 KV, lanthanum hexaboride filament) to visualize the anhydrous morphology of the samples.

Spectroscopic Characterization. FT-IR spectroscopy was performed using a Perkin Elmer Spectrum Two spectrophotometer. Raman spectra were recorded using Spectra Pro 2500i Raman spectroscopy under a 50× objective under an exposure of 40 mW laser power (λ = 532). XRD investigation was performed with an X-ray diffractometer (XRD, PANalytical) using Cu Kα radiation (λ = 1.54 Å). UV−vis absorption was recorded at 25, 32, 34, and 37 °C temperature from 220 to 800 nm at an interval of 0.5 nm using an UV−vis spectrophotometer (UV 2450, Shimadzu). The fluorescence emission spectra were recorded in an En Spire 2300 plate reader at an excitation wavelength of 360 nm.

Cell Culture. C2C12 (mouse myoblast) and NIH/3T3 (mouse fibroblast) cells were cultured in growth medium (GM) containing DMEM (Thermo Fisher Scientific) supplemented with 10% fetal bovine serum (FBS) and 1% antibiotic mixture of penicillin−streptomycin−neomycin (PSN) (Thermo Fisher Scientific) inside a CO_2 incubator containing 5% CO_2 and temperature of 37 °C. Cells were passaged by trypsinization using 0.05% trypsin EDTA (Thermo Fisher Scientific) and phosphate-buffered saline (PBS). The differentiation of C2C12 myoblasts was induced by switching from GM to differentiation medium (DM) containing DMEM supplemented with (0.5−1) % FBS and the antibiotic mixture penicillin−streptomycin−neomycin (PSN) when cells reached ∼80% confluency. DM of growing cells was changed everyday, and cells were allowed to differentiate for 6−7 days.[29]

Confocal Microscopy Investigation. A 50 μL aliquot of PNIPAM, CNP + PNIPAM, and MusCAMLR suspension was taken on a glass slide. A coverslip was placed over the material suspension and sealed throughout its boundary. Samples were exposed to 37 °C during observation under a confocal microscope. In the case of biological samples, cells were treated as per plan and at the end of the incubation fixed with 4% (w/v) paraformaldehyde permeabilized with 0.1% Triton X-100 and then stained with Alexa Flour 594-phalloidin (Invitrogen) at 1:100 dilution in PBS containing 1% BSA(w/v). It was followed by mounting the samples with DAPI-containing mounting media (Fluoroshield; Sigma-Aldrich). Images were obtained using a Zeiss LSM 700 confocal microscope.

Scanning Electron Microscopy (SEM) Investigation. PNIPAM, CNP, CNP + PNIPAM, CNP-PNIPAM, and MusCAMLR samples were placed on an aluminum foil and dried inside a vacuum desiccator overnight. Then, aluminum foil-containing samples were placed on copper stubs using carbon tapes. All the samples were spray-coated with gold and imaged under a Zeiss scanning electron microscope. The interaction of cells with the prepared composite materials was investigated in two different conditions including interaction with fixed and living cells, using SEM. In the case of fixed cell studies, ∼5000 cells (C2C12) were collected in 250 μL of PBS and were fixed with 4%(w/v) paraformaldehyde (Sigma-Aldrich), and excess of paraformaldehyde was washed with PBS. After that, cells

were resuspended in PBS and mixed with PNIPAM, CNP + PNIPAM, and MusCAMLR separately in centrifuge tubes. Then, the mixture of cells and materials was placed on aluminum foil, and HMDS (SRL, India) was applied and removed immediately for completion of the critical drying process. Samples were vacuum-desiccated for 24 h. Aluminum foil containing the cell−material mixture was placed on copper stubs using carbon tape followed by visualization by SEM. In the case of live cell interaction studies, a 200 μL aliquot of stock concentration of PNIPAM, CNP + PNIPAM, and MusCAMLR was spread over autoclaved (0.5 cm × 0.5 cm) aluminum foil separately and placed in a 24-well plate for 2 h inside a CO_2 incubator (temperature of 37 °C) to form the gel. Around 20,000 cells (C2C12) per well were seeded in coated wells and allowed to grow for 24 h. After 24 h, the spent medium was aspirated, and cells were washed with PBS and fixed with 4% (w/v) paraformaldehyde (Sigma-Aldrich). As mentioned above, HMDS was applied on all samples for critical drying and then kept inside a vacuum desiccator for 24 h. After that, similar protocol was followed to obtain images in the case of fixed cell experiments. The interaction study between NIH/3T3 and MusCAMLR was performed by growing NIH/3T3 cells in a well coated with MusCAMLR. In the case of myotube, C2C12 myoblasts were allowed to differentiate over MusCAMLR in the presence of DM for 6−7 days on a 12 mm autoclaved circular glass coverslip. The same concentration of MusCAMLR was taken, and similar protocols were followed to obtain scanning electron micrographs as in the case of C2C12 myoblasts.

MTT Assay. The working concentrations of PNIPAM, CNP, CNP + PNIPAM, CNP-PNIPAM, and MusCAMLR were taken in a well of a 96-well plate and allowed to form the gel inside a CO_2 incubator for 2 h. The C2C12 cells (5000 cells/well) were seeded and allowed to grow for 20 h. Then, 20 μL of thiazolyl blue tetrazolium bromide (MTT) solution (5 mg/mL) was added to each well and incubated for 4 h. After incubation time, all the medium was aspirated, and 100 μL of DMSO (Molychem, Mumbai, India) was added to each well to dissolve the produced formazan crystal. After that, the absorbance of samples was measured using an En Spire 2300 plate reader at 572 nm. The percentage of cell viability was calculated by using the following formula[53]

$$\text{percent of cell viability} = \frac{\text{absorbance of treated} - \text{absorbance of blank}}{\text{absorbance of control} - \text{absorbance of blank}} \times 100$$

AFM Investigation. AFM studies were conducted in force mapping and tapping modes under an atomic force microscope (Oxford Instruments, Asylum Research AFM). A 50 μL volume of PNIPAM and MusCAMLR suspensions was taken on a coverslip and spread appropriately throughout the surface of the coverslip. Similarly, C2C12 myoblasts and myotubes were allowed to grow over the MusCAMLR-coated coverslip and fixed with 4% (w/v) paraformaldehyde. Myoblasts and myotubes grown over uncoated coverslips were also used for force mapping as controls. Additionally, NIH/3T3 grown over MusCAMLR was imaged under AFM for comparison purposes. An area of ∼20 μm × 20 μm was scanned for each sample in the force mapping mode to obtain a spatially resolved elastic modulus and height profile data. The tapping mode was utilized to obtain the AFM images of different samples used in this study. A silicon nitride probe (Micro Cantilever, Olympus, Japan) of spherical geometry was used with a spring constant of 1.17−3.51 nN/nm and resonant frequency 61.6−90.0 kHz, with a nominal radius of 100 nm. The force trigger point used in the study was ∼50 nN to get a satisfactory indentation depth. The Hertz model[11] (eq 1) was used to find the modulus of elasticity from the force map data by fitting the force curve.

$$F = \frac{4}{3}\frac{E\sqrt{r_{\text{tip}}}}{(1-\nu^2)}d^{3/2} \tag{1}$$

where F is the indentation force, r_{tip} is the radius of the indenter, E is Young's modulus of the sample, ν is the Poisson's ratio, and d is the indentation depth.

The modulus of elasticity was calculated (from eq 1) from the force map of the scanned surface of each sample by taking the average of randomly selected points (85). The surface profile was analyzed from the height−force map at an interval of 2 μm throughout the scanned distance, and then, the average number of ridges on the surface was also counted. The height profiles from the AFM images of myotubes, myotubes grown over PNIPAM and MusCAMLR, and NIH/3T3 grown over MusCAMLR were analyzed by measuring the intratrough distance over the surface at an interval of 2 μm. All the presented analysis was performed in Igor Pro (6.37, MFP3D 15.00.92) software.

Differentiation of Myoblasts to Myotubes over the MusCAMLR-Coated Surface. The working concentrations of PNIPAM and MusCAMLR were coated over a freshly cleaned glass coverslip and kept at 37 °C for 1 h to form the hydrogel. Approximately 40×10^4 cells were seeded over the coated surface and allowed to differentiate for 7 days at the same conditions as mentioned above. The morphology of the differentiated cytoskeleton was investigated by staining with Alexa Flour 594-phalloidin under a confocal microscope. Giemsa staining was performed for the quantification of myotube formation.[54] Cells fixed with 100% methanol were stained with Giemsa stain (Merck Specialities Private Limited) for 10 min and then washed with Milli-Q water. Microscopic images were obtained at some randomly selected fields under an inverted light microscope. The fusion index was calculated using ImageJ software as the percentage of total nuclei present inside the differentiated myotube.

Immunocytochemistry. Immunocytochemistry (ICC) was performed as per the previously reported protocol.[55] In brief, differentiated C2C12 myotubes and myoblasts (grew for 24 h) were fixed with 4% (w/v) paraformaldehyde, followed by washing with 1× PBS two times. Freshly prepared blocking solution containing 1% BSA (w/v) and 0.2% Triton X-100 in PBS was applied on each coverslip and incubated for 30 min. MHC antibody (R&D system) was added to the samples (1:100 dilution) and incubated at 4 °C for overnight incubation. Thereafter, cells were washed twice with wash buffer (0.1% BSA (w/v) in 1× PBS) and incubated with Alexa Flour 594 conjugated with a secondary anti-mouse antibody (1:1000 dilution) for 1 h at room temperature. After this incubation, cells were washed twice with wash buffer and mounted with DAPI-containing mounting media. Images were obtained by using a Zeiss LSM 700 confocal microscope.

Animal Studies. A batch of 15 male Sprague−Dawley rats (age: 8−10 weeks, weight: 220−250 g) was procured from the CSIR-Central Drug Research Institute, Lucknow, India. All the in vivo studies reported in this work were done in accordance with the approval of the Institutional Animal Ethics Committee (IAEC) of IIT Kanpur (Approved protocol No. IITK/IEAC/2021/1140). Animals were kept at 2−3/cage in a room maintained with a 12 h light/dark cycle and temperature range of 22−24 °C. All animals had access to food and water on an ad libitum basis. They were randomly assigned into 3 groups (5 animals/ group), namely group 1 as the healthy control group, group 2 as the damaged muscle group/DOMS group, and group 3 as the MusCAMLR-treated group. Skeletal muscle damage in animals was induced by eccentric exercise according to the previously reported protocol.[32] Briefly, animals from the DOMS group and MusCAMLR-treated group were allowed to run eccentrically in a rodent treadmill (Orchid Scientific, India) at 16 m/min and −16° incline for 90 min. Blood samples were collected through a retro-orbital technique from all the groups after 36 and 108 h of the induction of muscle damage. MusCAMLR treatment was applied through intramuscular injection in the triceps brachii muscles of the MusCAMLR-treated group after 36 h of muscle damage (immediately after withdrawing blood samples). Each injection of MusCAMLR contained 200 mg per kg body weight. The serum creatine kinase level was measured by a commercial pathology laboratory. Animals from all the groups were sacrificed after 108 h of observation, and triceps brachii muscles were collected for further studies. Other organ tissues,

e.g., heart, liver, kidney, lung, intestine, and spleen, were also collected to investigate whether any toxicities were associated with MusCAMLR treatment or not.

H&E Staining. Paraffin-embedded tissue sections (10 μm) were stained with H&E by following a standard protocol.[56] In brief, tissue sections were deparaffinized with two washes of xylene for 5 min each. After this treatment, samples were rehydrated with descending grade alcohol treatment starting from absolute alcohol to 70% alcohol for 5 min each followed by washing with running water for 5 min. After that, samples were stained with hematoxylin solution for 5 min, washed with running water for 5 min, and allowed to differentiate with 1% acid alcohol for 30 s, followed by washing with running water for 5 min. Then, 95% alcohol was applied, and counterstain of eosin Y solution was applied for the next 30 s. Samples were dehydrated with ascending grade alcohol treatment starting from 95% alcohol to absolute alcohol treatment for 5 min each, washed with two changes of xylene, and mounted with xylene-based mounting medium. Finally, morphological characteristics of tissue samples were observed under a light microscope. Images obtained by H&E staining from the triceps brachii muscle tissues were analyzed using ImageJ software for the measurement of fiber cross-sectional area, percentage of centralize nuclei, etc.

Measurement of Tissue Hardness. Paraffin-embedded tissue sections (10 μm) were taken on a coverslip and further deparaffinized with the application of xylene. Tissue hardness was measured by force mapping mode under AFM (area scanned: 20 μm × 20 μm). A silicon probe (Oxford instruments) was used with a spring constant of 0.6−3.5 nN/nm and resonant frequency of 50−90.0 kHz with a nominal radius of 7 nm. The force trigger point was 3 nN to get a satisfactory indentation depth. Tissue hardness was calculated using Igor Pro (6.37, MFP3D 15.00.92) software.

Assessment of the Sarcomere's Morphology. SEM was performed to observe the morphology of the sarcomere. Deparaffinized tissue sections were gold-coated and visualized under a Zeiss scanning electron microscope. For TEM and toluidine blue-stained microscopic evaluation, glutaraldehyde-fixed TB muscles were post-fixed with 1% osmium tetroxide (SRL Pvt. Ltd. India). Ascending grade alcohol treatments were performed for dehydration of tissues and then embedded in eponate 12 resin (TED PELLA, INC.). Toluidine blue (Sigma-Aldrich) staining was performed by taking a 1 μm section with the help of a glass knife.[33,57] Ultrathin sections (∼100 nm) were taken, stained with uranyl acetate (Sigma-Aldrich, India), and observed under TEM (Technai120 KV, lanthanum hexaboride filament).[33,58]

Statistical Analysis. A two-way analysis of variance (ANOVA) test with the Bonferroni post-test was applied to compare the difference of more than one parameter in more than two groups. One-way ANOVA followed by Tukey's multiple comparison test was applied to compare the significance difference between more than two groups of one parameter. The two-tailed Student's t-tests was performed to compare the significance difference between two groups. Data were represented with mean ± SEM wherever applicable. Statistical analysis was performed by using GraphPad PRISM software (Version 5.01).

■ ASSOCIATED CONTENT

ⓈⒾ Supporting Information

The Supporting Information is available free of charge at https://pubs.acs.org/doi/10.1021/acsami.3c01889.

> Characterization of PNIPAM and CNP + PNIPAM; calculated d spacing values of PNIPAM, CNP + PNIPAM, and MusCAMLR; temperature-dependent UV−vis spectra of different samples; confocal microscopic images of MusCAMLR at different time points obtained at 37 °C; bright-field microscopic images of MusCAMLR and myoblast grown over MusCAMLR; analysis of the surface height profile of myotubes, myotubes grown over PNIPAM, myotubes grown over

MusCAMLR, NIH/3T3 grown over MusCAMLR; force maps, force−height maps and representative force-height profiles of PNIPAM, myoblast grown over MusCAMLR, myotubes grown over MusCAMLR, myotubes, and myoblasts; MHC antibody-stained confocal microscopic image of myotubes differentiated over PNIPAM; Giemsa-stained light microscopy images of C2C12 myotubes for the quantification of the fusion index; H&E-stained microscopic images of different vital organs excised from the animals of the DOMS group and healthy group; and representative TEM images of the sarcomere from the longitudinal section of the animals of healthy, DOMS, and MusCAMLR-treated groups (PDF)

Rat performing eccentric exercise in a motor-driven rodent treadmill (MP4)

■ AUTHOR INFORMATION

Corresponding Author

Santosh Kumar Misra − *Department of Biological Sciences & Bioengineering, Indian Institute of Technology Kanpur, Kanpur 208016 Uttar Pradesh, India; The Mehta family Centre for Engineering in Medicine, Indian Institute of Technology Kanpur, Kanpur 208016 Uttar Pradesh, India;* ⊙ orcid.org/0000-0002-3313-4895; Phone: +91-512-679-4013; Email: skmisra@iitk.ac.in

Author

Niranjan Chatterjee − *Department of Biological Sciences & Bioengineering, Indian Institute of Technology Kanpur, Kanpur 208016 Uttar Pradesh, India*

Complete contact information is available at:
https://pubs.acs.org/10.1021/acsami.3c01889

Author Contributions

This project was conceptualized by S.K.M. and planned by S.K.M. and N.C. Experiments were performed by N.C. The article was written by N.C. and edited by S.K.M.

Notes

The authors declare no competing financial interest.
The authors declare no competing interests. TOC and Scheme [1] were created with BioRender.com. All figures in the article file are author-created and include no copyrighted sources.

■ REFERENCES

(1) Pedersen, B. K.; Febbraio, M. A. Muscles, Exercise and Obesity: Skeletal Muscle as a Secretory Organ. *Nat. Rev. Endocrinol.* **2012**, *8*, 457−465.

(2) Stauber, W. T.; Clarkson, P. M.; Fritz, V. K.; Evans, W. J. Extracellular Matrix Disruption and Pain after Eccentric Muscle Action. *J. Appl. Physiol.* **1990**, *69*, 868−874.

(3) Dziki, J.; Badylak, S.; Yabroudi, M.; Sicari, B.; Ambrosio, F.; Stearns, K.; Turner, N.; Wyse, A.; Boninger, M. L.; Brown, E. H. P.; Rubin, J. P. An Acellular Biologic Scaffold Treatment for Volumetric Muscle Loss: Results of a 13-Patient Cohort Study. *npj Regener. Med.* **2016**, *1*, No. 16008.

(4) Skuk, D.; Roy, B.; Goulet, M.; Chapdelaine, P.; Bouchard, J.-P.; Roy, R.; Dugré, F. J.; Lachance, J.-G.; Deschênes, L.; Senay, H.; Sylvain, M.; Tremblay, J. P. Dystrophin Expression in Myofibers of Duchenne Muscular Dystrophy Patients Following Intramuscular Injections of Normal Myogenic Cells. *Mol. Ther.* **2004**, *9*, 475−482.

(5) Cheung, K.; Hume, P. A.; Maxwell, L. Delayed Onset Muscle Soreness. *Sports Med.* **2003**, *33*, 145−164.

(6) Grasman, J. M.; Zayas, M. J.; Page, R. L.; Pins, G. D. Biomimetic Scaffolds for Regeneration of Volumetric Muscle Loss in Skeletal Muscle Injuries. *Acta Biomater.* **2015**, *25*, 2−15.

(7) Wolf, M. T.; Dearth, C. L.; Sonnenberg, S. B.; Loboa, E. G.; Badylak, S. F. Naturally Derived and Synthetic Scaffolds for Skeletal Muscle Reconstruction. *Adv. Drug Delivery Rev.* **2015**, *84*, 208−221.

(8) Kim, J. H.; Seol, Y.-J.; Ko, I. K.; Kang, H.-W.; Lee, Y. K.; Yoo, J. J.; Atala, A.; Lee, S. J. 3D Bioprinted Human Skeletal Muscle Constructs for Muscle Function Restoration. *Sci. Rep.* **2018**, *8*, No. 12307.

(9) Brazile, B.; Lin, S.; Copeland, K.; Butler, J.; Cooley, J.; Brinkman-Ferguson, E.; Guan, J.; Liao, J. Ultrastructure and Biomechanics of Skeletal Muscle ECM: Implications in Tissue Regeneration. In *Bio-Instructive Scaffolds for Musculoskeletal Tissue Engineering and Regenerative Medicine*; Elsevier, 2017; pp 139−160.

(10) Smoak, M. M.; Mikos, A. G. Advances in Biomaterials for Skeletal Muscle Engineering and Obstacles Still to Overcome. *Mater. Today Bio* **2020**, *7*, No. 100069.

(11) Schmidt, S.; Zeiser, M.; Hellweg, T.; Duschl, C.; Fery, A.; Möhwald, H. Adhesion and Mechanical Properties of PNIPAM Microgel Films and Their Potential Use as Switchable Cell Culture Substrates. *Adv. Funct. Mater.* **2010**, *20*, 3235−3243.

(12) de Almeida, P.; Jaspers, M.; Vaessen, S.; Tagit, O.; Portale, G.; Rowan, A. E.; Kouwer, P. H. J. Cytoskeletal Stiffening in Synthetic Hydrogels. *Nat. Commun.* **2019**, *10*, No. 609.

(13) Haque, M. A.; Kamita, G.; Kurokawa, T.; Tsujii, K.; Gong, J. P. Unidirectional Alignment of Lamellar Bilayer in Hydrogel: One-Dimensional Swelling, Anisotropic Modulus, and Stress/Strain Tunable Structural Color. *Adv. Mater.* **2010**, *22*, 5110−5114.

(14) Volpi, M.; Paradiso, A.; Costantini, M.; Święszkowski, W. Hydrogel-Based Fiber Biofabrication Techniques for Skeletal Muscle Tissue Engineering. *ACS Biomater. Sci. Eng.* **2022**, *8*, 379−405.

(15) Jain, K.; Vedarajan, R.; Watanabe, M.; Ishikiriyama, M.; Matsumi, N. Tunable LCST Behavior of Poly (N-Isopropylacrylamide/Ionic Liquid) Copolymers. *Polym. Chem.* **2015**, *6*, 6819−6825.

(16) Gupta, S.; Singh, A.; Matsumi, N. Controlled Phase Behavior of Thermally Sensitive Poly(N-Isopropylacrylamide/Ionic Liquid) with Embedded Au Nanoparticles. *ACS Omega* **2019**, *4*, 20923−20930.

(17) Kundu, S.; Chatterjee, N.; Chakraborty, S.; Gupta, A.; Goswami, D.; Misra, S. K. Poly-Lysinated Nanoscale Carbon Probe for Low Power Two-Photon Bioimaging. *Spectrochim. Acta, Part A* **2022**, *270*, No. 120778.

(18) Chatterjee, N.; Kumar, P.; Kumar, K.; Misra, S. K. What Makes Carbon Nanoparticle a Potent Material for Biological Application? *WIREs Nanomed. Nanobiotechnol.* **2022**, *14*, No. e1782.

(19) Misra, S. K.; Srivastava, I.; Tripathi, I.; Daza, E.; Ostadhossein, F.; Pan, D. Macromolecularly "Caged" Carbon Nanoparticles for Intracellular Trafficking via Switchable Photoluminescence. *J. Am. Chem. Soc.* **2017**, *139*, 1746−1749.

(20) Evanghelidis, A.; Beregoi, M.; Diculescu, V. C.; Galatanu, A.; Ganea, P.; Enculescu, I. Flexible Delivery Patch Systems Based on Thermoresponsive Hydrogels and Submicronic Fiber Heaters. *Sci. Rep.* **2018**, *8*, No. 17555.

(21) Shi, Y.; Ma, C.; Peng, L.; Yu, G. Conductive "Smart" Hybrid Hydrogels with PNIPAM and Nanostructured Conductive Polymers. *Adv. Funct. Mater.* **2015**, *25*, 1219−1225.

(22) Zhu, C.-H.; Lu, Y.; Peng, J.; Chen, J.-F.; Yu, S.-H. Photothermally Sensitive Poly(N-Isopropylacrylamide)/Graphene Oxide Nanocomposite Hydrogels as Remote Light-Controlled Liquid Microvalves. *Adv. Funct. Mater.* **2012**, *22*, 4017−4022.

(23) Sanz, B.; von Bilderling, C.; Tuninetti, J. S.; Pietrasanta, L.; Mijangos, C.; Longo, G. S.; Azzaroni, O.; Giussi, J. M. Thermally-Induced Softening of PNIPAm-Based Nanopillar Arrays. *Soft Matter* **2017**, *13*, 2453−2464.

(24) Nigro, V.; Ripanti, F.; Angelini, R.; Sarra, A.; Bertoldo, M.; Buratti, E.; Postorino, P.; Ruzicka, B. Molecular Mechanisms Driving the Microgels Behaviour: A Raman Spectroscopy and Dynamic Light Scattering Study. *J. Mol. Liq.* **2019**, *284*, 718−724.

(25) Gartia, M. R.; Misra, S. K.; Ye, M.; Schwartz-Duval, A.; Plucinski, L.; Zhou, X.; Kellner, D.; Labriola, L. T.; Pan, D. Point-of-Service, Quantitative Analysis of Ascorbic Acid in Aqueous Humor for Evaluating Anterior Globe Integrity. *Sci. Rep.* **2015**, *5*, No. 16011.

(26) Hupkes, M.; Jonsson, M. K. B.; Scheenen, W. J.; Rotterdam, W.; Sotoca, A. M.; Someren, E. P.; Heyden, M. A. G.; Veen, T. A.; Os, R. I. R.; Bauerschmidt, S.; Piek, E.; Ypey, D. L.; Zoelen, E. J.; Dechering, K. J. Epigenetics: DNA Demethylation Promotes Skeletal Myotube Maturation. *FASEB J.* **2011**, *25*, 3861−3872.

(27) White, J.; Barro, M. V.; Makarenkova, H. P.; Sanger, J. W.; Sanger, J. M. Localization of Sarcomeric Proteins During Myofibril Assembly in Cultured Mouse Primary Skeletal Myotubes. *Anat. Rec.* **2014**, *297*, 1571−1584.

(28) Ku, S. H.; Park, C. B. Myoblast Differentiation on Graphene Oxide. *Biomaterials* **2013**, *34*, 2017−2023.

(29) Rashid, M. M.; Runci, A.; Polletta, L.; Carnevale, I.; Morgante, E.; Foglio, E.; Arcangeli, T.; Sansone, L.; Russo, M. A.; Tafani, M. Muscle LIM Protein/CSRP3: A Mechanosensor with a Role in Autophagy. *Cell Death Discovery* **2015**, *1*, No. 15014.

(30) Relaix, F.; Zammit, P. S. Satellite Cells Are Essential for Skeletal Muscle Regeneration: The Cell on the Edge Returns Centre Stage. *Development* **2012**, *139*, 2845−2856.

(31) Chapman, M. A.; Meza, R.; Lieber, R. L. Skeletal Muscle Fibroblasts in Health and Disease. *Differentiation* **2016**, *92*, 108−115.

(32) Armstrong, R. B.; Ogilvie, R. W.; Schwane, J. A. Eccentric Exercise-Induced Injury to Rat Skeletal Muscle. *J. Appl. Physiol.* **1983**, *54*, 80−93.

(33) Stupka, N.; Lowther, S.; Chorneyko, K.; Bourgeois, J. M.; Hogben, C.; Tarnopolsky, M. A. Gender Differences in Muscle Inflammation after Eccentric Exercise. *J. Appl. Physiol.* **2000**, *89*, 2325−2332.

(34) Garrett, W. E. Muscle Strain Injuries. *Am. J. Sports Med.* **1996**, *24*, S2−S8.

(35) Yanagisawa, O.; Sakuma, J.; Kawakami, Y.; Suzuki, K.; Fukubayashi, T. Effect of Exercise-Induced Muscle Damage on Muscle Hardness Evaluated by Ultrasound Real-Time Tissue Elastography. *SpringerPlus* **2015**, *4*, No. 308.

(36) Swist, S.; Unger, A.; Li, Y.; Vöge, A.; von Frieling-Salewsky, M.; Skärlén, Å.; Cacciani, N.; Braun, T.; Larsson, L.; Linke, W. A. Maintenance of Sarcomeric Integrity in Adult Muscle Cells Crucially Depends on Z-Disc Anchored Titin. *Nat. Commun.* **2020**, *11*, No. 4479.

(37) Wu, J.; Lin, Y.; Sun, J. Anisotropic Volume Change of Poly(N-Isopropylacrylamide)-Based Hydrogels with an Aligned Dual-Network Microstructure. *J. Mater. Chem.* **2012**, *22*, No. 17449.

(38) Jana, S.; Levengood, S. K. L.; Zhang, M. Anisotropic Materials for Skeletal-Muscle-Tissue Engineering. *Adv. Mater.* **2016**, *28*, 10588−10612.

(39) Brazel, C. S.; Peppas, N. A. Synthesis and Characterization of Thermo- and Chemomechanically Responsive Poly(N-Isopropylacrylamide-Co-Methacrylic Acid) Hydrogels. *Macromolecules* **1995**, *28*, 8016−8020.

(40) Valencia, L.; Enríquez, F. J.; Valencia, M.; Díaz, R. Tuning the LCST of PNIPAM via Random Oxidation-Sensitive Thioether Functionalities. *Macromol. Chem. Phys.* **2017**, *218*, No. 1600556.

(41) Discher, D. E.; Janmey, P.; Wang, Y. Tissue Cells Feel and Respond to the Stiffness of Their Substrate. *Science* **2005**, *310*, 1139−1143.

(42) Guardiola, O.; Andolfi, G.; Tirone, M.; Iavarone, F.; Brunelli, S.; Minchiotti, G. Induction of Acute Skeletal Muscle Regeneration by Cardiotoxin Injection. *J. Visualized Exp.* **2017**, No. e54515.

(43) Harris, J. B.; MacDonell, C. A. Phospholipase A2 Activity of Notexin and Its Role in Muscle Damage. *Toxicon* **1981**, *19*, 419−430.

(44) Plant, D. R.; Colarossi, F. E.; Lynch, G. S. Notexin Causes Greater Myotoxic Damage and Slower Functional Repair in Mouse Skeletal Muscles than Bupivacaine. *Muscle Nerve* **2006**, *34*, 577−585.

(45) Takekura, H.; Fujinami, N.; Nishizawa, T.; Ogasawara, H.; Kasuga, N. Eccentric Exercise-induced Morphological Changes in the Membrane Systems Involved in Excitation—Contraction Coupling in Rat Skeletal Muscle. *J. Physiol.* **2001**, *533*, 571−583.

(46) Connolly, D. A. J.; Sayers, S. E.; Mchugh, M. P. Treatment and Prevention of Delayed Onset Muscle Soreness. *J. Strength Cond. Res.* **2003**, *17*, 197−208.

(47) Donnelly, A. E.; McCormick, K.; Maughan, R. J.; Whiting, P. H.; Clarkson, P. M. Effects of a Non-Steroidal Anti-Inflammatory Drug on Delayed Onset Muscle Soreness and Indices of Damage. *Br. J. Sports Med.* **1988**, *22*, 35−38.

(48) Eston, R.; Peters, D. Effects of Cold Water Immersion on the Symptoms of Exercise-Induced Muscle Damage. *J. Sports Sci.* **1999**, *17*, 231−238.

(49) Tiidus, P. M. Massage and Ultrasound as Therapeutic Modalities in Exercise-Induced Muscle Damage. *Can. J. Appl. Physiol.* **1999**, *24*, 267−278.

(50) Yackzan, L.; Adams, C.; Francis, K. T. The Effects of Ice Massage on Delayed Muscle Soreness. *Am. J. Sports Med.* **1984**, *12*, 159−165.

(51) Nieman, D. C.; Dumke, C. L.; Henson, D. A.; McAnulty, S. R.; Gross, S. J.; Lind, R. H. Muscle Damage Is Linked to Cytokine Changes Following a 160-Km Race. *Brain, Behav., Immun.* **2005**, *19*, 398−403.

(52) Nieman, D. C.; Henson, D. A.; Dumke, C. L.; Oley, K.; McAnulty, S. R.; Davis, J. M.; Murphy, E. A.; Utter, A. C.; Lind, R. H.; McAnulty, L. S.; Morrow, J. D. Ibuprofen Use, Endotoxemia, Inflammation, and Plasma Cytokines during Ultramarathon Competition. *Brain, Behav., Immun.* **2006**, *20*, 578−584.

(53) Misra, S. K.; Ohoka, A.; Kolmodin, N. J.; Pan, D. Next Generation Carbon Nanoparticles for Efficient Gene Therapy. *Mol. Pharmaceutics* **2015**, *12*, 375−385.

(54) Veliça, P.; Bunce, C. M. A Quick, Simple and Unbiased Method to Quantify C2C12 Myogenic Differentiation. *Muscle Nerve* **2011**, *44*, 366−370.

(55) Niu, M.; Li, L.; Su, Z.; Wei, L.; Pu, W.; Zhao, C.; Ding, Y.; Wazir, J.; Cao, W.; Song, S.; Gao, Q.; Wang, H. An Integrative Transcriptome Study Reveals Ddit4/Redd1 as a Key Regulator of Cancer Cachexia in Rodent Models. *Cell Death Dis.* **2021**, *12*, No. 652.

(56) Misra, S. K.; Ye, M.; Ostadhossein, F.; Pan, D. Pro-Haloacetate Nanoparticles for Efficient Cancer Therapy via Pyruvate Dehydrogenase Kinase Modulation. *Sci. Rep.* **2016**, *6*, No. 28196.

(57) Ghnenis, A. B.; Czaikowski, R. E.; Zhang, Z. J.; Bushman, J. S. Toluidine Blue Staining of Resin-Embedded Sections for Evaluation of Peripheral Nerve Morphology. *J. Visualized Exp.* **2018**, No. 58031.

(58) Stupka, N.; Tarnopolsky, M. A.; Yardley, N. J.; Phillips, S. M. Cellular Adaptation to Repeated Eccentric Exercise-Induced Muscle Damage. *J. Appl. Physiol.* **2001**, *91*, 1669−1678.

O

WIREs
NANOMEDICINE AND NANOBIOTECHNOLOGY   WILEY

What makes carbon nanoparticle a potent material for biological application?

Niranjan Chatterjee | Piyush Kumar ⬤ | Krishan Kumar | Santosh K. Misra ⬤

Department of Biological Sciences & Bioengineering and The Mehta Family Centre for Engineering in Medicine, Indian Institute of Technology Kanpur, Kanpur, Uttar Pradesh, India

Correspondence
Santosh K. Misra, Biological Sciences & Bioengineering, and The Mehta Family Centre for Engineering in Medicine, Indian Institute of Technology Kanpur, Kanpur, Uttar Pradesh 208016, India.
Email: skmisra@iitk.ac.in

Edited by: Dipanjan Pan, Associate Editor and Nils G. Walter, Co-Editor-in-Chief

Abstract

Carbon materials are generally utilized in the form of carbon allotropes and their characteristics are exploited as such or for improving the thermal, electrical, optical, and mechanical properties of other biomaterials. This has now found a broader share in conventional biomaterial space with the generation of nanodiamond, carbon dot, carbon nanoparticles (CNPs), and so forth. With properties of better biocompatibility, intrinsic optical emission, aqueous suspendability, and easier surface conjugation possibilities made CNPs as one of the fore most choice for biological applications especially for use in intracellular spaces. There are various reports available presenting methods of preparing, characterizing, and using CNPs for various biological applications but a collection of information on what makes CNP a suitable biomaterial to achieve those biological activities is yet to be provided in a significant way. Herein, a series of correlations among synthesis, characterization, and mode of utilization of CNP have been incorporated along with the variations in its use as agent for sensing, imaging, and therapy of different diseases or conditions. It is ensembled that how simplified and optimized methods of synthesis is correlated with specific characteristics of CNPs which were found to be suitable in the specific biological applications. These comparisons and correlations among various CNPs, will surely provide a platform to generate new edition of this nanomaterial with improvised applications and newer methods of evaluating structural, physical, and functional properties. This may ensure the eventual use of CNPs for human being for specific need in near future.

This article is categorized under:

    Nanotechnology Approaches to Biology > Nanoscale Systems in Biology
    Diagnostic Tools > Biosensing
    Diagnostic Tools > In Vitro Nanoparticle-Based Sensing
    Therapeutic Approaches and Drug Discovery > Emerging Technologies

KEYWORDS
bioimaging, biosensing, carbon nanoparticles, drug delivery

1 | INTRODUCTION

The prominence of carbon is dictated by its natural abundance across the biological system than all the other known elements in the periodic table (Hirsch, 2010). Carbon has received huge attention as a material in synthetic research because of its catenation property and binding capabilities with other elements in various ways. These characteristics have endowed carbon with a wide range of physical and chemical properties. Carbon has been acclaimed for having allotropes of significant importance. These allotropes are structurally distinct forms of elemental carbon organized in a variety of ways rendering them as different materials (Karthik et al., 2014). The allotropes of carbon starting from diamond, graphite, and fullerene to graphene, carbon nanotubes (CNTs), carbon dots (CDs), and carbon nanoparticles (CNPs) have found many different applications in fields of biomedical importance. Earlier, graphite and diamond were the two widely known allotropes of carbon until the discovery of fullerene by Kroto et al. (1985). The relatively higher peculiar specific susceptibility of graphite (-5.1×10^{-6}) compared to diamond (-0.49×10^{-6}) makes electrical conductivity in graphite comprehensible, as stated by C. V. Raman (Raman, 1929). The fullerene, graphene, and CNT have received significant attention owing to their suitability for different biomedical applications such as biosensing, drug delivery, and therapeutics (Bhattacharya et al., 2016; Figure 1). In general, the evolution of nanocarbon family and their important biological applications can be traced back to the decade of 1980 (Figure 2). The synthesis of CNTs and graphene by Iijima (1991) and Novoselov et al. (2004), respectively led to a new era of applications of nanocarbon-based materials. Graphene was reported as a remarkable carbon allotrope having the capacity to construct three-dimensional graphite, one-dimensional CNTs, and zero-dimensional fullerene. The electrical conductivity, elevated mechanical strength, and improved young modulus of graphene was regarded as useful properties in a nanomaterial to be exploited for medical implants and biosensing applications (Choudhary et al., 2014).

The sp^2 hybridized single-layered sheet of graphene offers high surface area to volume ratio which can interact with variety of molecules including DNA bases through π–π interaction (Rao et al., 2009). This type of interaction has the potential for non-covalent functionalization to improve the aqueous solubility of carbon materials via hydrophilic moieties present as part of the biomolecules (Subrahmanyam et al., 2009). Such carbon nanomaterials (CNMs) have been represented as a two-dimensional graphene sheet containing sp^2 hybridized carbon consisting of a hexagonal lattice (Clancy et al., 2018). The folded structure of graphene sheets was found to give rise to the high aspect ratio entities, having structure of nanotubes and named as CNTs. However, these developed materials had enhanced properties but needed to be further modified with chemical species to make them usable in biological systems due to inability to be solubilized or suspendable in an aqueous medium. This requirement led to the generation of new category of carbon materials called CNPs (Sun et al., 2006). In very less time after its generation, CNPs as an evolving nanomaterial of carbon has attained a significant interest by optimizing different synthetic strategies, which eventually could increase its aqueous availability for biological applications including drug carrier, gene therapy, and so forth (Misra, Chang, et al., 2015). Additionally, novel methods of characterizations have been utilized to predict better outcomes from biological applications of these CNMs. Properties achieved by optimized synthetic protocols and suitably used characterization methods, CNMs have gained enough reputation in the field of biomedical sciences but need further attention to reach end users including research labs and clinics as commercial sensing, bioimaging, and therapeutic agents. In this regard, many reviews of scientific research have been published discussing various synthesis methods and biological properties of CNPs with good details, but they lack descriptive correlations among synthesis, properties, and applications in the progression of CNP as a material of biological significance. In this review, it is presented that what led to improvement in certain synthetic procedures for CNPs, how novel characterization methods could help in correlating biological properties to certain physical or chemical properties and which biological application could be preferential for a specific CNP in the course of achieving current lot of CNPs. It also highlights that how CNPs compatibility with advanced optical study tools and modifiable surface characteristics have made them desirable material for sensing, imaging, and therapy with minimum hindrance and negligible side effects.

1.1 | Types of CNMs and their introduction to biological system

After appearing in the decade of the 1980s on the map of scientific applications, various carbon allotropes were produced or purified. Among some of the very first applications, fullerenes were used as an antiviral agent (Schinazi et al., 1993). Growing through various classes and characteristics, CNMs have reached a very significant position with
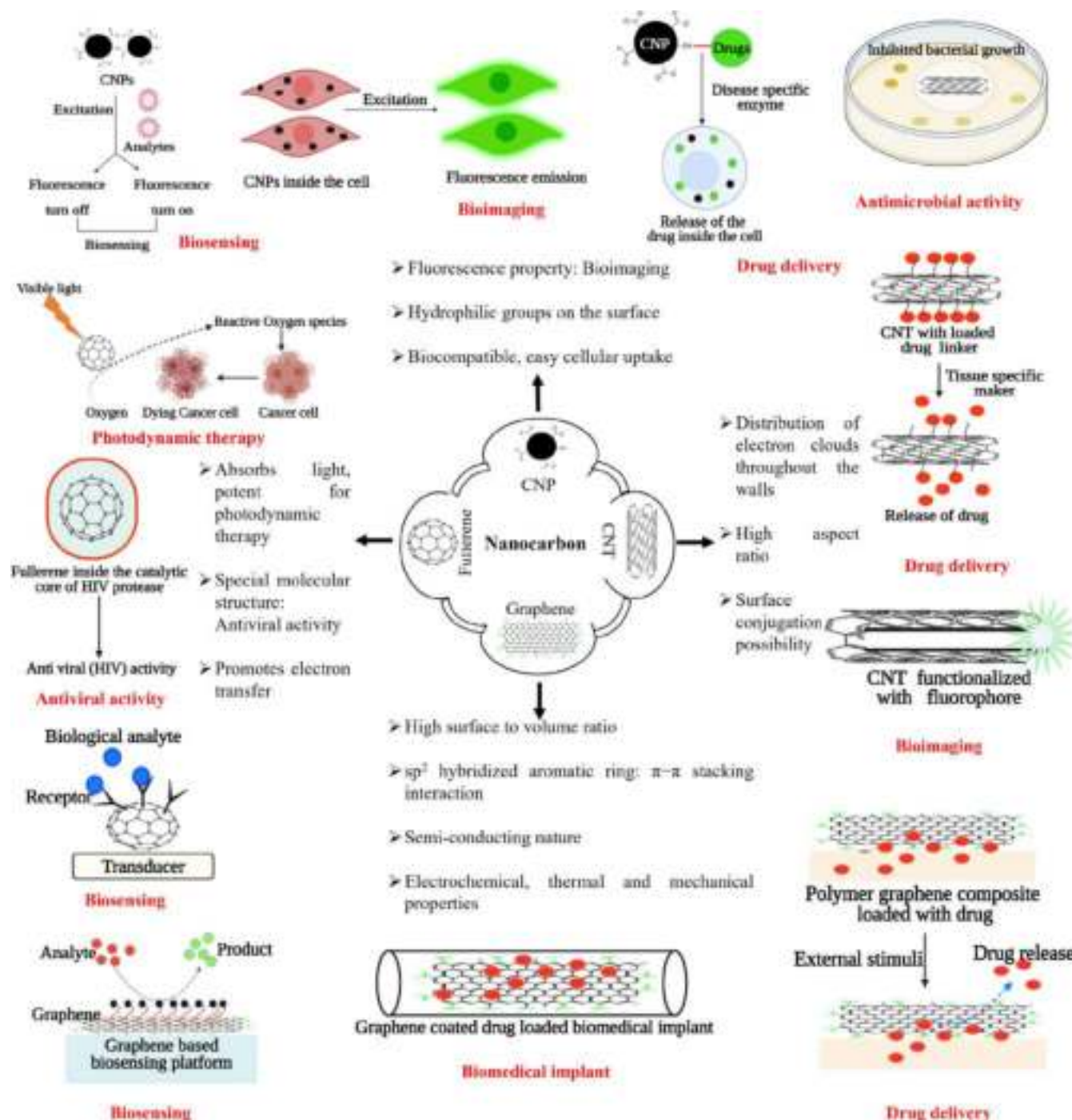
FIGURE 1 Schematic illustration depicting some key features of different nanoforms of carbon, namely, CNP, CNT, graphene with their biological application especially in biosensing, bioimaging, drug delivery, and therapy illustration depicting some different nanoforms of carbon and their application. Image created with BioRender.com

biological significance (Figure 2). Some of the basic features of CNMs classify them in various interesting categories of diamond-like, graphitic, nanotubes, fullerenes, dots, and nanoparticles.

Diamond is regarded as one of the most famed gemstones in human society for many centuries. It is the hardest known material with face-centered cubic crystal structure having thermal conductivity, optical transparency, and chemical inertness (Ferro, 2002; Karthik et al., 2014). Diamond and diamond-like carbon (DLC) exhibit biological interactions by surface coating with higher surface roughness and structural symmetry. The presence of very good biocompatibility and higher degree of mechanical strength increases its′ utility in bioimplants. (Hauert, 2003;
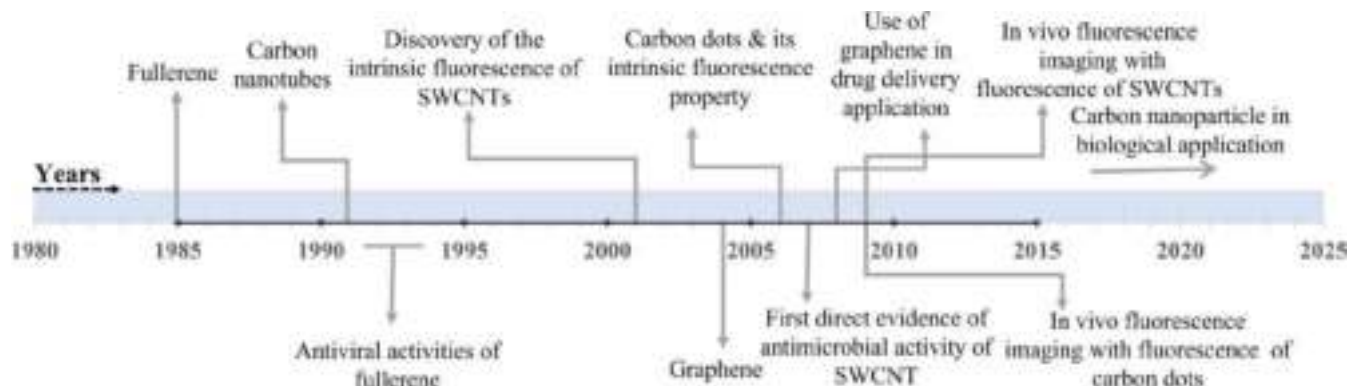
FIGURE 2 A timeline sketch depicting year-wise evolution in the nanocarbon family and their biological application (Bakry et al., 2007; Hong et al., 2015; Kang et al., 2007; Liu, Peng, & Li, 2008; Shen et al., 2012)

Lackner & Waldhauser, 2010). The surface coating of non-crystalline diamond on silicon (100) substrates prevents platelet aggregation which indicates its potential for cardiovascular devices as well (Narayan et al., 2006). DLC is also used for antimicrobial application by incorporating a variety of toxic materials like copper, silver, and so forth (Hauert, 2003).

On the other side, discovery of fullerene by Kroto et al. (1985) manifested great interest in researchers because of its distinct structural and physicochemical properties. The C_{60} form of fullerene was found to be more stable compared to others forms of fullerene because of the peculiar arrangement of carbon atoms. From biomedical perspective, fullerene and its polymer composites displayed antioxidant activities by acting as a scavenger of free radical produced in excess amount during many diseases like cancer (Goodarzi et al., 2017). Derivatized fullerene has been shown to be a potent candidate for photodynamic therapy. Photodynamic therapy is essentially meaning a nonthermal photochemical procedure which need the presence of photosensitizer, oxygen, and visible light simultaneously. Generally, pristine C_{60} is not soluble in biological fluids, water, and so forth which prevent its efficient photoactivation due to the formation of nano aggregates, but when it is functionalized by attaching some hydrophilic or amphiphilic side chain with the spherical core of C_{60}, it enhances the solubility in water as well as in biological media which in turn also improved its photochemical activity in biological system. Upon interaction with light, transition happens from ground state to short-lived singlet excited state (lifetime ~1.3 ns) and from there to triplet state of long lifetime (lifetime ~50–100 μs). It then reacts with dissolved oxygen which catalyzes the production of reactive oxygen species (Goodarzi et al., 2017; Sharma et al., 2011). It is also reported that fullerene can exhibit antiviral activity against HIV, semliki forest virus, and so forth (Bakry et al., 2007). However, the application of some fullerene derivatives has also raised concern regarding their biocompatibility as it can be accumulated in cell membranes and interior affecting the cell functions. This undesirable reactive species formation leads to oxidative damage of the cells (Goodarzi et al., 2017).

Hollow cylinders of graphitic carbon sheet closed by five-membered rings at either end, were found to be source of some interesting carbon materials, called as CNTs (Iijima, 1991). The most important characteristic of CNTs is their aspect ratio wherein the electron clouds are distributed throughout the walls making available π electrons for possible interactions. The CNT-based nanocomposites have been shown to possess improved strength, for example, the addition of 1% CNT in polyester resin can improve the tensile strength, as well as stiffness of the composite (Choudhary et al., 2014; Ramanathan et al., 2008). It was reported that CNT can be modified chemically for its biological application. The CNTs have been reported to cross the biological barrier in plants. Tripathi et al. (2011) showed that hydrophilic CNTs could stimulate the growth of plant, *Cicer arietinum*. Kang et al. (2007) reported for the first time that single-walled carbon nanotube (SWCNT) can show strong antimicrobial activity by damaging the membrane of bacteria. CNTs have prominently been used for drug delivery application because of the presence of higher drug loading capacity, and chemical stability. Addition of functional moieties on the surface of CNTs makes it target-specific thereby reducing the chances of side effects and unwanted toxicities of the loaded drugs. One such study has experimentally demonstrated the delivery of anticancer drug inside the cancer cell by design of the SWCNT-based drug carrier. This carrier comprised of SWCNT functionalized with moieties causes tumor-specific uptake and anticancer drug connected through a linker which can be cleaved inside the tumor cell (Chen et al., 2008). The pH-dependent fluorescence of SWCNT is observed when it is functionalized non-covalently with fluorescein-polyethylene glycol. The increased

fluorescence with increasing pH was utilized for bioimaging and sensing purposes. (Nakayama-Ratchford et al., 2007). It is also reported that single-stranded DNA (ssDNA) labeled with fluorescent dye on being added to SWCNT led to quenching of the fluorescence. Fluorescence intensity was restored in the presence of a particular target like protein or DNA because of the competitive binding of the target with SWCNT (Yang et al., 2008). This is to note that Iijima et al. (1999) reported a new class of carbon allotrope in the course of investigation of CNT production by CO_2 laser ablation, named as carbon nano-horns (CNHs). They found some horn-like projection from the center of the particle, which were essentially composed of single-layered graphene sheets. Single-walled carbon nano-horns (SWCNHs) have received a significant attention because of its easier dispersibility compared to SWCNTs and the ability to improve mechanical properties of the gels of pyridyl-appended oligo(p-phenylenevinylene) derivatives triggered by Ag^+ ions (Bhattacharjee et al., 2015).

Another important carbon-based material with nanoscale dimensions came into the picture with the discovery of graphene. It is known as the simplest allotropic form of carbon and designated as the thinnest material synthesized till now (Priyadarsini et al., 2018). The family of graphene can be perceived as multi-layered graphene, graphene sheet, oxidized graphene (GO), and reduced form of graphene oxide (rGO). After the successful production of graphene in 2004, it emerged as a distinct and extraordinary nanocarbon material to be researched because of its distinctive electrochemical, thermal, and mechanical properties. The presence of high surface-to-volume ratio of graphene sheet is also important in sensing as well as drug delivery applications. The presence of sp^2 hybridized aromatic ring structure help in loading the aromatic drug by non-covalent $\pi-\pi$ stacking interaction (Liu, Peng, & Li, 2008; Shen et al., 2012). Exploration of various biomedical applications of graphene extended toward the tumor therapy, drug delivery, and theranostics. Graphene became exciting nanocarbon material to be widely used in the field of drug delivery by increasing the bioavailability of the drug as well as by stimuli-responsive drug release with certain modifications (Song et al., 2020). One such exciting application has been reported by He et al. (2015). They demonstrated a NIR laser-guided drug carrier by preparing the assembly of mesoporous silica grafted with alkyl chains loaded with one of the potent anticancer drug doxorubicin and capped by reduced graphene oxide (RGO) through non-covalent interaction. Exposure to near-infrared (NIR) radiation led to the generation of local heat causes removal of the RGO cap which results in the release of the drug (He et al., 2015). It has also been reported that polyethylene glycol (PEG) functionalized nanographene sheets (NGS) can be used for in vivo photothermal therapy to cause the destruction of cancer cell. It could be achieved by its higher accumulation in tumor tissue through enhanced permeability and retention (EPR) effect. The EPR effect occurs by the mechanism of rapidly growing cancer tissues, which recruit new blood vessels to sustain the adequate supply of nutrients and oxygen. These types of blood vessels are quite distinct from normal as it has larger pores with a diameter of around 0.1–3 μm with incomplete endothelial lining which makes it leaky. These leaky vasculatures are responsible for enhanced accumulation of nano-size material inside the cancer tissue (Nakamura et al., 2016). They also have proved the application of the same system for in vivo imaging when it was labeled with a NIR fluorescent dye Cy7 (Yang et al., 2010). The utility of graphene in biosensing was experimentally demonstrated in many ways, for example, the detection of ascorbic acid in aqueous humor for determining the integrity of the anterior globe. The specificity of this sensor was achieved by positioning the enzyme ascorbate oxidase on graphene-based poly(styrene)-block-poly (acrylic acid) composite (Gartia et al., 2015). Moitra, Bhagat, et al. (2021) introduced graphene oxide in the preparation of biosensor because of its unique physicochemical property for volatile pheromone sensing in olive fruit pest (*Bactocera oleae*). Apart from this, graphene is also known to be effective for personalized 3D printed cardiovascular drug-eluting stent for the controlled release of anticoagulant and anti-restenosis drugs in the patients suffering from coronary artery disease (Misra, Ostadhossein, et al., 2017).

These carbon-based nanomaterials with various advantageous characteristics to be materials of choice for biological applications have been found to possess numerous limitations and weaknesses, as well. Some of these shortcomings fall in the category of aqueous insolubility/in-suspendability, non-biodegradability, biotoxicity, inability to chemical conjugations, and costly methods of preparations and use. Keeping these all areas for possible improvements, a new class of CNMs has been developed in recent past. CNP is one such material. As this is one of the most advanced carbon forms and encompasses various improvements compared to other carbon forms for biological applications, CNPs need better understanding in detail that what makes CNP a potent material for biological applications. CNPs based on their size range, surface, optical and electrical properties can be named as CDs, CNPs, carbon nanospheres (CNSPs), and so forth. Interestingly, Xiong et al., 2019 reported the synthesis of carbon nanorod (CNR) with dual emissive property (blue and yellow emissions) having a length of ∼50 nm and diameter of 20 nm using citric acid and polyhedral oligomeric silsesquioxanes (POSS) with various organic functional groups. It has also been demonstrated that the mixing of CDs passivated with electron-donating and accepting group tends to make a combination of rod- and ring-like structure as

observed under atomic force microscopy (Srivastava, Khamo, et al., 2019; Srivastava, Sar, et al., 2019). These materials have been synthesized by various top-down and bottom-up methods. In top-down approach, CNPs are synthesized from graphene oxide, graphite powder, carbon nanotube, coal soot, and so forth whereas, in bottom-up methods, CNPs are synthesized from smaller precursor, for example, by carbonization of certain organic molecules, and so forth (Baker & Baker, 2010). Some of the extensively used synthetic procedures include electrochemical oxidation, chemical oxidation, thermal oxidation, step-wise chemical fusion, laser ablation, ultrasonic method, and arc discharge, and so forth (Jaiswal, Ghosh, & Chattopadhyay, 2012; Misra et al., 2018). The physicochemical characterization of CNPs prepared by thermal oxidation process using hot plate method contain hydroxyl (—OH), carboxyl group (—COOH), and so forth on its surface with negative zeta potential (Misra, Ohoka, et al., 2015). The synthesized CNPs with diameter <10 nm has been categorized as CDs (Ray et al., 2021), which is basically made up of central crystalline core and amorphous shell. The central nanocrystalline core were found to be composed of sp^2 hybridized carbon whereas outer amorphous shell contains functional groups of different types (Semeniuk et al., 2019). They represent a huge potential in the field of bioimaging, because of fluorescence properties, and therapeutic applications. This is found to be possible due to its ability to passivate or attach drugs for controlled drug delivery (Hong et al., 2015; Misra, Chang, et al., 2015; Misra, Ostadhossein, et al., 2017). Fang et al. have shown the tunability in the fluorescence emission of CDs in the presence of $KMnO_4$ and ascorbic acid. They further utilized this phenomenon for the detection of alkaline phosphatase and α-fetoprotein (Fang et al., 2018). In another study, Victoria et al. have tuned the residual chirality of CDs and have observed better antimicrobial activity for D-CDs than L-CDs (Victoria et al., 2020). These characteristics can be achieved by introducing various raw components in different steps of synthesis. Thus, materials and methods of synthesis and conditions followed in a particular protocol can tune the properties and final fate of CNPs. This warrants a thorough discussion on various materials and methods used for the synthesis of CNPs and comparison with other nanomaterials with similar properties in biological systems. CNPs/CQDs/CDs show potential for biological applications as they show enhanced biocompatibility and biodegradability in comparison to other conventional quantum dots (QDs; Table 3). These comparisons would also help in deciding the optimum nanomaterials for a particular task to be performed in a certain biological system. It has been reported that nonsimilar to other QDs such as CdSe and PbS, CNMs generate very nonconsequential by-products on degradation (Gil et al., 2021; McHugh et al., 2018) and show higher bioavailability in the biological system due to their inherent water suspendability or solubility (Li et al., 2019). These inherent properties such as aqueous solubility and low photobleaching of CNPs/CQDs/CDs further helps in making their synthesis process more warranted by eliminating the surface functionalization step which is often required in other QDs and nanoparticles for their application in biological systems (Kumar et al., 2020). The ease of synthesis of CNPs/CQDs/CDs can be realized by a range of organic precursors available for their synthesis whereas, other QDs rely majorly on synthetic inorganic compounds. They are also environmentally friendly, as they do not require extreme conditions and harmful chemicals for their synthesis, which are commonly required for the synthesis of QDs. Further studies with computer simulations can be tools for better understanding of molecular-level interactions and possibilities of various manipulations as achieved in case of certain peptides (Moitra et al., 2017).

1.1.1 | Synthesis of CNMs

The variety of methods for the synthesis of CNPs can be broadly characterized as "top-down" or "bottom-up" methods based on the size and chemistry of starting precursor and the final product (Figure 3). The top-down approaches involve breaking down of macroscopic materials into small-sized particles using physical or chemical processes whereas, in the bottom-up approach smaller molecules are polymerized or carbonized to form nanoscale particles (Wang et al., 2019). The summary of commonly used methods has been tabulated below focusing on the precursor, methods, and conditions employed to achieve CNPs of varied sizes (Table 1).

1.2 | Top-down approaches

1.2.1 | Electrochemical oxidation

The electrochemical oxidation mediated synthesis protocol involves the use of the source material as an anode and cathode submerged in an electrolyte. It has been reported to be used for synthesis of CNPs from materials such as
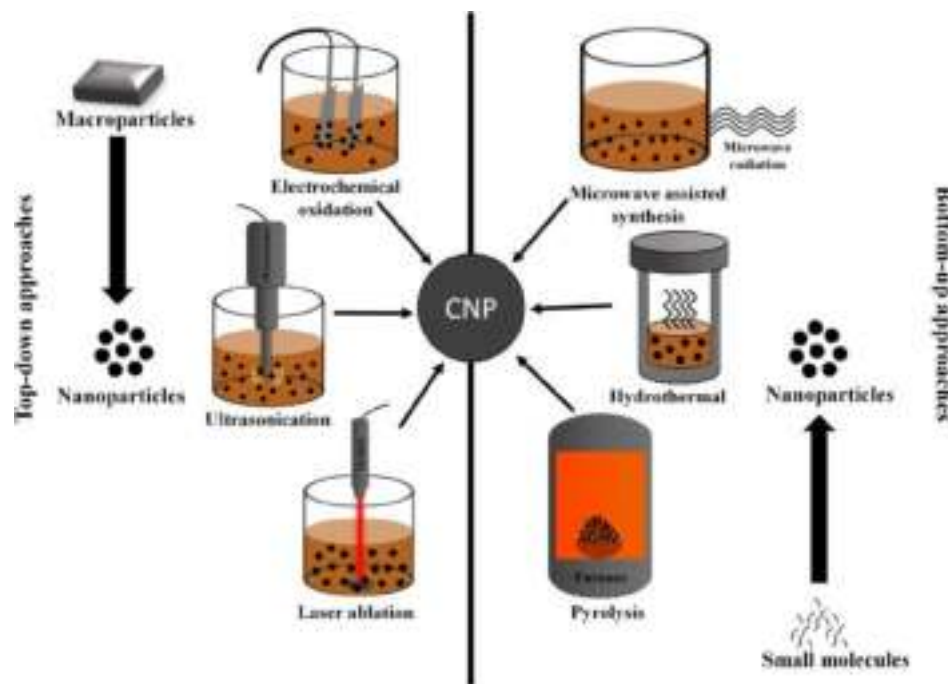
FIGURE 3 Schematic representation of popular methods to fabricate CNPs (CNP) in top-down and bottom-up approaches

graphite, alcohols, and CNTs (Deng et al., 2014; Zhao et al., 2008; Zhou et al., 2007). This method gives an advantage of being low cost and susceptible to easier manipulations. The properties of the resulting nanoparticles can be influenced by varying the applied voltage (Deng et al., 2014).

1.2.2 | Ultrasound-assisted synthesis

Microscopic chemical entities can be broken down into smaller particles with the use of external energy such as ultrasonic sound waves. Das et al. have used ultrasonication to produce CDs of varied sizes from coal. In this procedure, the sonicated solution was filtered using a 0.22 μm polytetrafluoroethylene membrane, and dialysis was performed. The process was found to yield particles in the range of 1–4, 1–6, 2–5, and 10–30 nm with environmental safety and biological applications (Das et al., 2019). Boruah et al. have also used the ultrasonic-assisted wet chemical-oxidation method to produce carbon quantum dots (CQDs) from sugarcane bagasse, garlic, and taro peels (Boruah et al., 2020).

1.2.3 | Laser ablation

This method uses a laser to irradiate the target surface and increases the temperature to form a plasma state which then crystalizes to form nanoparticles (Wang et al., 2019). Kazemizadeh et al. have reported the synthesis of CNPs through laser ablation method from graphite using Yd:NAG (1064 nm) laser (Kazemizadeh et al., 2017). The method has been further used by Yogesh et al. to synthesize CNPs from activated carbon powder (Yogesh et al., 2017) and charcoal (Yogesh et al., 2021).

1.3 | Bottom-up approaches

1.3.1 | Microwave-assisted synthesis

The microwave-assisted synthesis of CNPs has high attention in recent years due to the easiness of the procedure and high yield of the production. This provides a facile method to synthesize CNPs using even a regular domestic

TABLE 1 Summary of different methods and materials employed for CNP synthesis

S. No.	Method	Precursor	Conditions	Size	References
Top-down methods					
1	Electrochemical oxidation	Graphite	50 V, 4 days	1–9 nm	Zhang et al. 2013
		Graphite	3 V	1.9 and 3.2 nm	Zhao et al., 2008
		Low-molecular-weight alcohols	3–9 V, 4 h	2.1, 2.9, 3.5, and 4.3 nm	Deng et al., 2014
		Acetonitrile, toluene, and tetrabutylammonium perchlorate (TBAP)	2.2 to −1.6 V	N.A.	Bian et al. 2020
		graphite	15–60 V	4.5 nm	Ming et al. 2012
2	Ultrasonic treatment	Sugarcane bagasse; taro peels and garlic peels	H_2O_2, 40 KHz, ~700 W, 3–4 h	8–12 nm	Boruah et al., 2020
		Coal	40 KHz, 6 h	1–4 nm 1–6 nm 2–5 nm 10–30 nm	Das et al., 2019
3	Laser ablation	Graphite	Yd:NAG laser (1064 nm), frequency: 5 Hz, pulse: 10 ns	~30 nm	Kazemizadeh et al., 2017
		Activated carbon powder	Second harmonic Yd:NAG laser (532 nm), frequency: 10 Hz, pulse: 10 ns, 30 min under stirring at 450 rpm	14 nm and 3.7 nm	Yogesh et al., 2017
		Charcoal powder in ethanol	Yd:NAG laser (1064 nm), frequency: 10 Hz, pulse: 10 ns, 20 min	21 nm	Yogesh et al., 2021
Bottom-up methods					
4	Microwave assisted	Trisodium citrate and sodium thiosulphate	600 W, 6 min	~ 4–5 nm	Gupta, Verma, Khan, Tiwari, et al., 2016
		PEG and chitosan	600 W, 3 min	8 nm	Gupta et al. 2012
		Citric acid monohydrate, thiourea; boric acid	600 W, 5 min	3.5 nm	Pal et al., 2019
		Sucrose, sulfuric acid and ortho-phosphoric acid	130°C, 10 min	4.6 nm	Kainth et al., 2020
		Potato dextrose agar	600 W, 3 min	4.3 nm	Gupta, Verma, Khan, Tiwari, et al., 2016
		Acacia concinna seeds (shikakai)	800 W, 2 min	2.5 nm	Bhamore, Jha, Singhal, et al., 2018
		Bougainvillea plant	1400 W, 10 min	~2–6 nm	Khare et al., 2018
		Lignin	600 W, 10 min	4.6 nm	Rai et al., 2017
		Lassi	800 W, 6.5 min	11.57 nm	Kumar et al., 2018
		Citric acid	750 W, 2 min	5–10 nm	Khan et al., 2015
		Charcoal	200°C, 600 W	3–7.6 nm	Patidar et al., 2017
		PEG	900 W, 10 min	4.5 nm	Jaiswal, Ghosh, & Chattopadhyay, 2012
		Sucrose and ortho-phosphoric acid	100 W, 3 min 40 s	3–10 nm	Chandra et al., 2011

TABLE 1 (Continued)

S. No.	Method	Precursor	Conditions	Size	References
5	Hydrothermal/ Solvothermal	*Hylocereus undatus* fruit extract	180°C, 12 h	2.5 nm	Arul et al., 2017
		Apple juice	150°C, 12 h	4.5 nm	Mehta et al., 2015
		Tulsi (*Ocimum tenuiflorum*) leaves	200°C, 4 h	5 nm	Bhatt et al., 2018
		Pyrus pyrifolia fruit	180°C, 6 h	2 nm	Bhamore, Jha, Singhal, et al., 2018
		Citric acid	250°C, 5 h	8–12 nm	Sharma et al., 2016
		Tamarindus indica	210°C, 5 h	3.4 nm	Bano et al., 2018
		Glucose; ascorbic acid; β-alanine	150°C, 5 h	N.A.	Gogoi et al., 2019
		Onion waste	120°C, 15 lbs pressure, 2 h	15 nm	Bandi et al., 2016
		Pomelo (*citrus grandis*)	200°C, 7 h	3 nm	Ramar et al., 2018
		Colocasia esculenta	170° C, 5 h	3.2 nm	Gogoi et al., 2017
		1,7′-Dimethyl-2′-propyl-1H,3′H-[2,5′] bibenzoimidazolyl (DPBI)	220°C, 3 h	N.A.	Prasad et al., 2016
		Milk	170°C, 12 h	~2.5 nm	Misra, Mukherjee, et al., 2016
		Lychee waste	180°C, 5 h with water and ethanol	3.13 nm	Sahoo et al., 2020
6	Pyrolysis	Papaya waste (*Carica paya*)	200°C, 15 min	~7 nm	Pooja et al., 2019
		Finger millet ragi (*Eleusine coracana*)	300°C, 3 h	~3–8 nm	Murugan et al., 2019
		Bitter apple	~300°C, 2 h	N.A.	Aggarwal et al., 2020
		Aloe vera leaf	250°C, 2 h	1.5–3.7 nm	Sarkar et al., 2017
		Pasture grass; sucrose and hair	850°C, 6 h under N_2	9–13 nm	Kapri et al., 2018

Abbreviations: N.A., Not available.

microwave oven (Jaiswal, Ghosh, & Chattopadhyay, 2012; Wang et al., 2011). The method has been used to yield CNPs in a relatively short period of time (Bhamore, Jha, Park, & Kailasa, 2018; Gupta, Verma, Khan, Tiwari, et al., 2016; Khan et al., 2015; Mehta et al., 2017; Pal et al., 2019). The sources as common as sucrose, PEG, bougainvillea plant (Khare et al., 2018), lassi (Kumar et al., 2018), citric acid (Khan et al., 2015; Pal et al., 2019), lignin (Rai et al., 2017), potato dextrose agar (PDA; Gupta, Verma, Khan, Tiwari, et al., 2016), and charcoal (Patidar et al., 2017) has been employed for the synthesis of CNPs using this method. Along with household microwaves, specialized microwave synthesizers have also been reported for the synthesis of the CNPs. Li et al. have used a microwave-assisted hydrothermal-synthesis system from SINEO using glucose and PVA for CNP synthesis (Li et al., 2016). The commercial synthesizers can offer better reaction control and safety conditions (Schwenke et al., 2015).

1.3.2 | Hydrothermal/solvothermal treatment

The hydrothermal method is among the most common methods used for the synthesis of CNPs. Hydrothermal method involves the heating of the carbon source dissolved in water, buffers, or other solvents at high temperatures in a teflon

lined stainless steel container. Typically, the source solution is heated till a dark brown solution is achieved which is further processed via dialysis/filtration to yield a monodisperse particle population. The method has been adapted for a large number of raw materials ranging from, apple juice (Mehta et al., 2017), tulsi leaves (Bhatt et al., 2018), and *Pyrus pyrifolia* fruit (Bhamore, Jha, Singhal, et al., 2018). The method has also been found useful to introduce heteroatoms such as nitrogen in CNPs synthesized from sucrose (Naik et al., 2019), *Lantana camara* (Bandi et al., 2018), fruit extract of *Hylocereus undatus* (dragon fruit; Arul et al., 2017); boron and fluorine to citric acid CDs (Tiwari et al., 2020), nitrogen and sulfur to rose petal CDs (Sharma et al., 2016).

1.3.3 | Pyrolysis

CNPs have also been synthesized by pyrolysis of various carbon precursors. The source material is heated at a high temperature to yield a carbonized product. Pooja et al. have synthesized CDs from the papaya waste and have employed these CDs for chromium sensing (Pooja et al., 2019). Pyrolysis has also been exploited for the synthesis of CNPs from finger millet ragi (Murugan et al., 2019), bitter apple (Aggarwal et al., 2020), *Aloe vera* leaf (Sarkar et al., 2017) and Pasture grass, sucrose, and hair (Kapri et al., 2018).

2 | CHARACTERIZATION OF CNPs

Based on the required features expected from the produced CNPs, evaluation of chemical, physical, or physicochemical characterizations need to be performed. CNPs are generally characterized by different tools and techniques of spectroscopy, microscopy, and analytical techniques. These techniques are crucial in terms of defining different types of properties, namely, scanning electron microscopy (SEM), atomic force microscopy (AFM) is mainly used to define morphology and micro/nanostructure whereas dynamic light scattering (DLS) and TEM are applied for the measurement of hydrodynamic and anhydrous diameter (Figure 5b). TEM is also applicable for studying the ordered-ness of the composition depending on the presence of diffraction pattern of electron (Semeniuk et al., 2019). The AFM uses the interaction of probe with the surface under investigation to map the surface based on the van der Waals force (attraction) and electrostatic force (repulsion) experienced by the probe (Liang et al., 2020). It can elucidate the properties such as surface topology, friction, and conductivity to name a few. Pudza et al. used AFM in association with HR-TEM to determine the nature of CDs morphological structure (Pudza et al., 2020). The interpretation of the height profile from the 2D images of the surface could be correlated to the dimension of the particles (Hou et al., 2017). The mapping
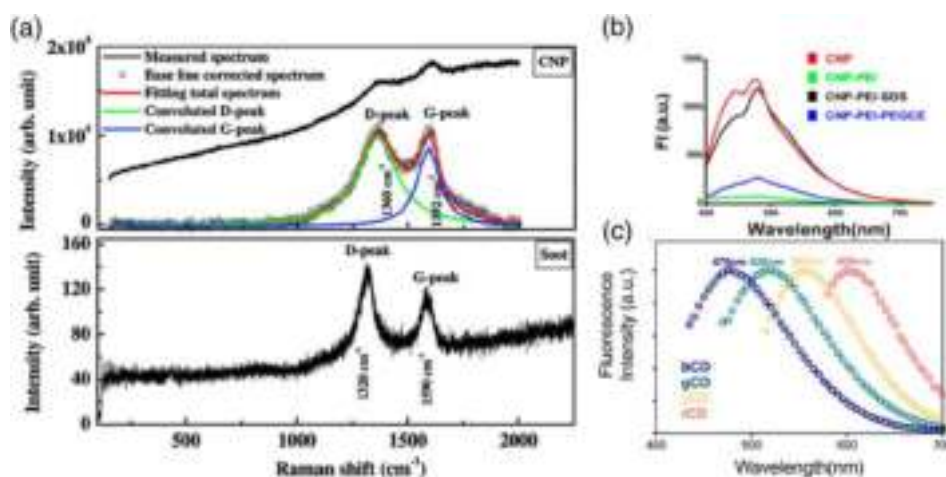

FIGURE 4 Representative (a) Raman spectra of CNPs synthesized from soot. Reprinted (adapted) with permission from Ray et al. (2009). Copyright© 2009, American Chemical Society. (b) Emission spectra of CNPs synthesized from agave nectar (CNP), CNP-PEI, CNP-PEI-SDS, and CNP-PEI-PEGCE. Reprinted (adapted) with permission from Misra, Ostadhossein, et al. (2017). Copyright© 2017, American Chemical Society. (c) Emission spectra of CDs synthesized by solvothermal methods followed by separation through polarity-based chromatography. Reprinted (adapted) with permission from Nguyen et al. (2020). Copyright© 2020, American Chemical Society
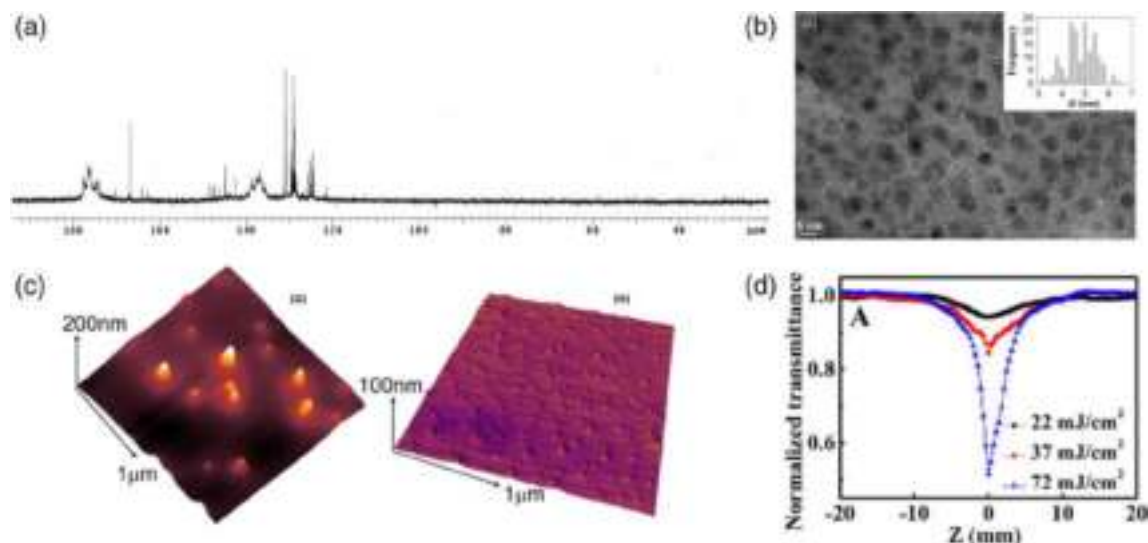
FIGURE 5 Representative (a) ^{13}C NMR spectrum and (b) TEM micrograph of CNPs prepared from carbon soot. (Reprinted (adapted) with permission from Tian et al. (2009). Copyright$^{©}$ 2009, American Chemical Society). (c) AFM height profile of the synthesized colloidal carotene carbon nanoparticles. (Reprinted with permission from Misra, Mukherjee, et al. (2016), under a Creative Commons Attribution 4.0 International License Copyright$^{©}$ 2016 Springer Nature). (d) Z scan data of CNPs for the determination of nonlinear optical property. Reprinted with permission from Tan et al. (2014). Copyright$^{©}$ 2013 Elsevier Ltd

of the particle can also indicate the behavior of the particles on the surface as has been discussed by Wu et al. The discrepancy between the size of the particles for TEM and height from AFM were suggested to arise from the probable aggregation of the particles on the solid surface (Wu et al., 2013). Misra et al. used AFM to determine the size of the colloidal carotene CNPs and have corroborated with the results obtained from TEM (Figure 5c; Misra, Mukherjee, et al., 2016; Misra, Ostadhossein, et al., 2016). Apart from TEM, x-ray diffraction is an important tool for studying the crystallinity of CNPs. The broader peak at 23° could indicate the presence of amorphous carbon whereas the peak at around 41° indicated the diffraction pattern of graphitic carbon structure (Hou et al., 2015; Prasad et al., 2016). The Raman spectroscopy for CNPs synthesized from carbon soot was described by the presence of G (Graphitic) and D (Disordered graphitic) mode which is present approximately at 1592 and 1360 cm^{-1} (Figure 4a). The ratio of the intensity of D band (I_D) and intensity of G band (I_G; $I_D/I_G = 2$) could provide information about the non-crystallinity of these CNPs as well as sp^3 versus sp^2 hybridization of carbon (Ray et al., 2009; Semeniuk et al., 2019). The compositional analysis by x-ray photoelectron spectroscopy (XPS) of CNPs was reported by Ray et al., 2009. The composition of CNPs could be established with the presence of carbon (59%), oxygen (37%), and nitrogen (4%). The presence of nitrogen was probably because of nitric acid oxidation during the synthetic process.

Fourier-transform infrared (FTIR) spectra are crucial to decipher the surface functional groups based on the specific stretching vibration of the type of chemical bond present in the molecule. It has been reported that the surface of CNPs synthesized from agave nectar, a natural carbohydrate source by hydrothermal method contains O—H, C—H, C=O, and C—O—C at ~3400, ~2900, ~1700, and ~1200 cm^{-1}, respectively (Misra, Srivastava, et al., 2017). FTIR spectra of CNPs synthesized from carbon soot in presence of nitric acid indicate the presence of C—O—C, C=C at ~1100 and 1265 cm^{-1} wavenumber, respectively. The peak position at 1400–1650 cm^{-1} and at the wave number 1735 cm^{-1} attributed to C—H and conjugated C—N, C=N, and N—O bond. The band position at 2335 and 2360 cm^{-1} ascribed to —CN group. The presence of a small band at 1835 cm^{-1} is attributed to the C=N stretching vibration (Ray et al., 2009). FTIR spectral representation of CNPs indicates that the presence of functional groups is dependent on the precursor and the method of synthesis. The insights into the structural elucidation of CNPs could also be gained using Nuclear Magnetic Resonance (NMR) spectroscopy (Figure 5a). The ^{13}C NMR spectroscopic technique can easily distinguish between aliphatic (sp^3) and aromatic (sp^2) carbons. The sp^3 hybridized carbon resonates (8–80 ppm) at a different frequency than sp^2 bonded carbon (90–180 ppm) resulting in different chemical shift values. The emergence of peak at ~138 ppm represents internal sp^2 bonded carbons. The presence of terminal sp^2 bonded carbons in the structure of CNPs reveals a peak at ~114 ppm, however, if these are oxidized to carboxylic and/or carbonyl functionalities, other peaks are

observed in the range between 170 and 180 ppm (Tian et al., 2009). Similarly, ^{1}H NMR spectroscopy can give information on presence of aromatic and aliphatic protons present on the surface of CNPs (Ghosh et al., 2019; Khanam et al., 2013). A complete structural assignment of organic modifiers was successfully performed by Philippidis et al. (2013) using solution 1D and 2D high-resolution NMR spectroscopy. Interestingly, Duan et al. (2020) investigated the structure of carbon dot prepared using citric acid and ethylenediamine by means of solid-state 13C, 13C{1H}, 1H–13C, 13C{14N}, and 15N solid-state NMR experiments. This tool helped in the structural elucidation of nanoparticle matrix and quantitatively proved the presence of a molecular fluorophore, 5-oxo-1,2,3,5-tetrahydroimidazo[1,2-a] pyridine-7-carboxylic acid (IPCA) which was previously reported to be responsible for the fluorescy of these CDs. Therefore, NMR is a highly suitable technique to study the nanoparticle core and its chemical composition along with the surface functionalization.

The optical properties of CNPs are analyzed mainly by the analysis of their absorption and emission spectrum obtained from Ultraviolet–Visible (UV–Vis) and fluorescence spectroscopy. CNPs synthesized from food caramels (bread, jaggery and sugar, and honey) shows two peaks between 240 and 400 nm at nearly 280–300 nm which could be correlated to $\pi \rightarrow \pi^*$ transition and at 340–380 nm probably due to the $n \rightarrow \pi^*$ transition (Sk et al., 2012; Wu et al., 2013). The pattern of UV–Vis absorption spectra was reported to change depending on different types of modification like the polarity of the synthesized CNPs, surface passivation, and the precursor of the synthetic method (Nguyen et al., 2020; Sk et al., 2012).

Measurement of photoluminescence is another method frequently used for interpreting optical properties of CNPs. This is determined by exciting the CNPs at different wavelengths causing emission at various higher wavelengths. It was reported that the CNP synthesized from agave nectar demonstrates the emission peaks at ∼488 nm when it is excited at 365 nm wavelength. The addition of cationic polymer polyethylenimine (PEI) with CNP leads to a decrease in fluorescence intensity which is again recovered by the addition of an anionic sodium dodecyl sulfate (SDS) as it pulls the positively charged PEI due to counter-ionic interaction. Upon addition of nonanionic surfactant polyethylene glycolcetylether (PEGCE) no such drastic change was observed (Misra, Ostadhossein, et al., 2017; Figure 4b). This observation was very significant in explaining the origin of optical emission by CNPs as a surface phenomenon (Li et al., 2014; Misra, Srivastava, et al., 2017). It is also reported that the mechanism of photoluminescence is dependent on sp^2 hybridized domain size as well as the richness of oxidized surface defects (Nguyen et al., 2020). The concept of quantum confinement effect (QCE) of nanostructure can also explain the luminescence property of CNPs. The QCE is defined as the restriction of the movement of the electron when nanostructures are formed because of the discrete energy level of electrons. This causes increase in the band gap between the highest occupied molecular orbital (HOMO) to the lowest unoccupied molecular orbital (LUMO) as the sized of nanoparticle decreased (Semeniuk et al., 2019). The presence of oxygen-containing surface defects is another reported feature for the fluorescence emission of CNPs. Nguyen et al. (2020) has experimentally shown that CNPs synthesized by solvothermal method yields CNPs with different polarity having different fluorescence spectra. It contains CDs with spectra ranging from blue to red. The oxygen-rich groups increased up to 29% increment of oxidation when they progressed from blue to red CNPs (Figure 4c). The introduction of extra electronic state with lesser band gap by surface oxidation than the core of the CNP is key player for the red-shifted emission (Nguyen et al., 2020). This observation can be correlated by another investigation by Ding et al. (2016). They experimentally demonstrated that separation of CNPs through silica column chromatography synthesized from Urea and p-phenylenediamine by hydrothermal method exhibit blue, green, yellow, and red fluorescence emissions. The presence of an increased number of carboxyl groups and the degree of oxidation on the surface were the contributing components for more surface defects in CNPs for shifting the emission toward the red fluorescence (Ding et al., 2016). Additionally, CNPs synthesized from three isomers of phenylenediamines by solvothermal method followed by the separation with a silica column chromatography were found to emit red, green, and blue luminescence under UV excitation. This diverse emission of photoluminescence was found to be because of the differences in amount of nitrogen content and sizes of CNPs (Jiang et al., 2015). Apart from the single-photon absorption, the phenomenon of two-photon absorption is also reported in the case of CNP. Two-photon excitation is one of the optical phenomena, where the excitation of fluorophore is accomplished by simultaneous absorption of two photons (usually in IR range). The fluorescence emission by two-photon absorption happens if the total energies of two-photon is equal or greater than the difference of energy between the excited state and ground state. The curiosity to the two-photon property of CNP achieves a unique interest in the field of bioimaging because of the ability of deep tissue penetration and less phototoxic damage (Pan et al., 2016). This property is dependent on the optical nonlinearity and near-infrared fluorescence emission (NIR). One of the tools for the characterization of optical nonlinearity is Z scan technique. Tan et al. (2014) have reported the strong nonlinear response of CNPs by the application of Z scan technique. They observed the optical limiting effect in the Z scan curve which is defined as the decrease in transmittance with the increment in input fluency (Figure 5d). It has been reported that carbon dot prepared from the solution of glutathione in formamide through

microwave mediated heating shows two-photon absorption property which is characterized by a linear increase in two-photon fluorescence intensity with the square of the laser power (Pan et al., 2015, 2016).

3 | BIOLOGICAL APPLICATIONS OF CNPs

The unique properties of CNPs such as biocompatibility (Das et al., 2019; Yan et al., 2006) and innate fluorescence have led to their applications in diverse fields of biological research (Figure 6). They have found applications from sensing the presence of heavy metals in contaminated water bodies to imaging in the biological systems. CNPs are found to inherently possess excellent photoluminescence properties with an added advantage of having low toxicity and good biocompatibility. The photostability and their ability to interact with various groups have made CNPs a good alternative for bioimaging. They can also be used to monitor the distribution of drugs in the human body (Wen et al., 2015). The luminescent carbon nanoparticles (LCNs) synthesized from molasses have been shown to have altered properties on surface passivation with different chemistries. The surface passivation with multi-arm PEG was used to prepare NIR-emitting imaging probes whereas, passivation with PNIPAM a temperature-responsive polymer has resulted in a drug carrier particle system capable of delivering drug effectively to cancer cells (Mukherjee et al., 2015). Unique combination of optical, surface functionalization, and drug interaction characteristics of CNPs need to be understood better for progressing toward better products of biomedical importance.

3.1 | Bioimaging

Bioimaging is a set of techniques used to visualize the biological system from outside without or minimally perturbing the system. During the process of bioimaging interactions between light and matter are utilized to map the intricate
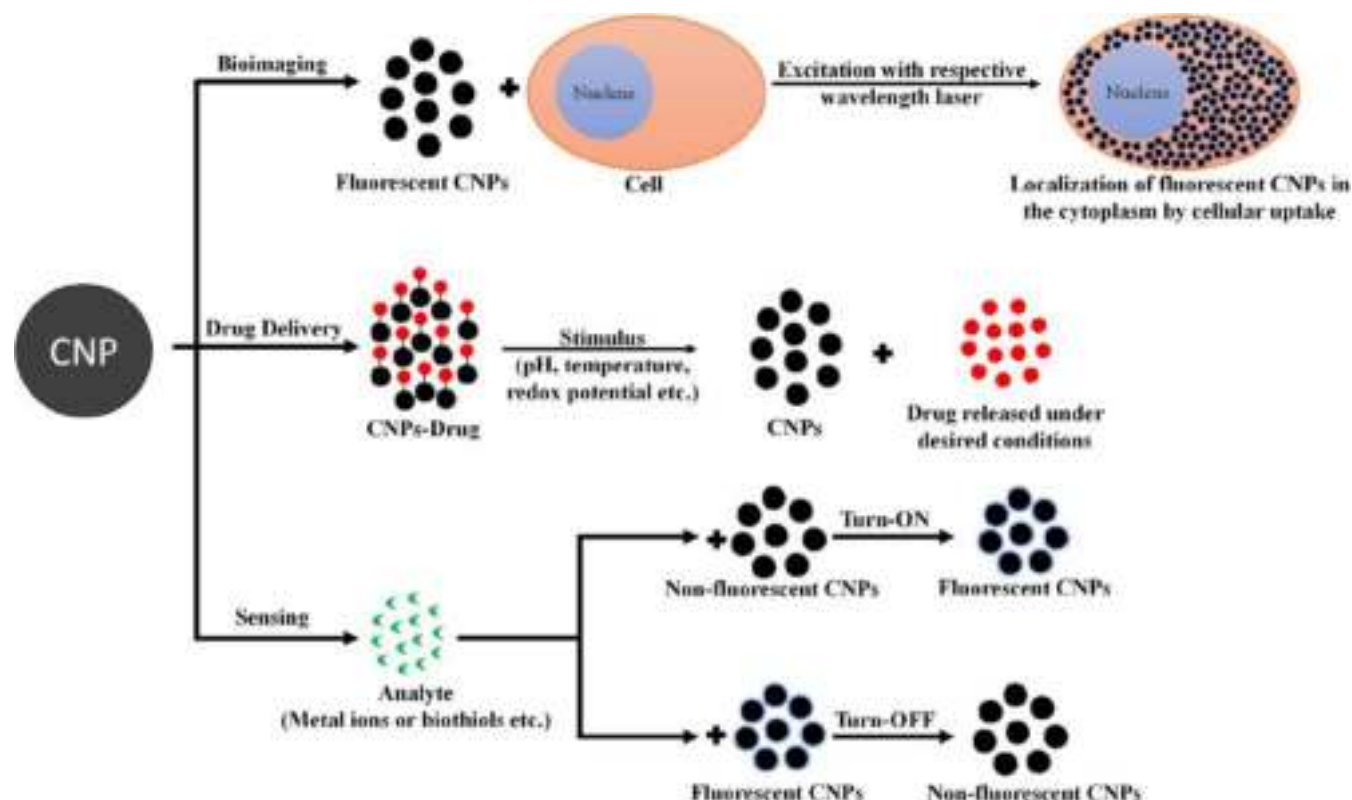

FIGURE 6 Schematic representation for major applications of CNPs. The CNPs can be used as a bioimaging probe due to their excellent biocompatibility. The CNPs can accumulate in the cytoplasm of the cells by endocytosis. The CNPs can be further modified with stimulus (pH, temperature, or redox potential) responding functional groups to serve as drug carrier, which enables them to release drugs under desired conditions. The CNPs can also respond to the presence of analytes such as metal ions and biothiols by changing their fluorescence

details of the system of interest. In order to aid the process of imaging various materials which cause the least interference to the system can be introduced to distinctly mark the area of interest by enhancing the contrast with respect to the background. Nanoparticle-based fluorescent probes have emerged as an efficient and reliable alternative to conventional molecular probes due to their versatility and robust nature. They can offer better signal and stability under different conditions in comparison to conventional fluorescent proteins and small molecules (Baker, 2010; Pu et al., 2014). Among various nanoparticles such as noble metal (gold and silver) nanoparticles, quantum dots, and fluorescently doped silica, CNMs provide an option to have tunable and biocompatible bioimaging probes. A comprehensive insight into this application, one of the carbon materials, CDs have been synthesized by Ali et al. (2020). The application of CNP as an imaging probe paves the easy way to translate the inherent property of fluorescence into action. As discussed previously, the particles prepared from different sources and methods may give different optical properties to the resulting nanoparticles. The photophysical properties of the CDs have been studied in bulk as well as at the single-molecule level by Srivastava, Khamo, et al. (2019). In the study, the authors have suggested the presence of electron acceptor and donor groups on the surface of CDs influence its photophysical properties. The synthesized fluorescent carbon nanoparticles (FCN) from carbohydrates using different methods were found to have different solubilities and optical properties. The as-synthesized FCNs can be transformed into functionalized FCNs that retain their fluorescence for various bio-labeling applications (Bhunia et al., 2013). Bhunia et al. reported that FCNs functionalized with TAT peptide and folate, increased the cell labeling and uptake in folate receptor-positive cells (Figure 7a). They also reported blue and green fluorescence FCNs derived from vitamin B_1 (Bhunia et al., 2014) and red fluorescent CDs from functiona+lization of hydrophobic FCNs derived from ascorbic acid with PEG, arginine, histidine, biotin, and folic acid for imaging in different cell lines (Ali et al., 2016). The hydrophobic CNPs synthesized from ascorbic acid after functionalization with polar functional groups and dispersion in polar medium show red emission when excited with blue and green lasers. These red-emitting FCNs have been used for cell labeling applications in CHO cells. Functionalization with folate made the FCN selective to the folate receptor-expressing cells. This was shown by comparing the selective labeling of folate receptor overexpressing KB cells compared to CHO cells with low expression of folate receptors (Ali
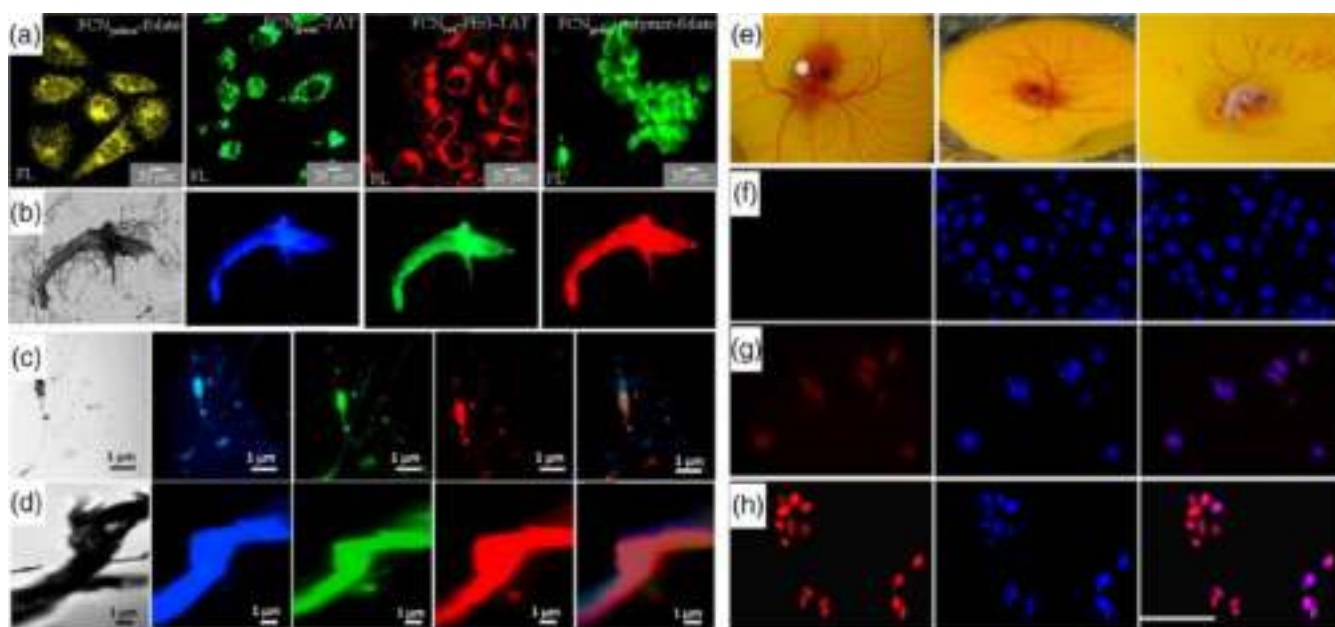

FIGURE 7 (a) Labeling of HeLa cells using different fluorescent CNs (Bhunia et al. (2013), Reprinted under a Creative Commons Attribution-NonCommercial-NoDerivs 3.0 Unported License Copyright© 2013 Springer Nature), (b) CDs as fluorescent probes for imaging *penicillium sp.* at different excitation wavelengths 405 nm (blue);488 nm (green) 561 nm (red; Reprinted with permission from Bhamore, Jha, Park, and Kailasa (2018), Copyright© 2018, Elsevier), (c) Imaging of *E. coli* and (d) *Aspergillus aculeatus* using CDs at different excitation wavelengths (Reprinted with permission from Bhamore et al. (2019), Copyright© 2019, Elsevier), (e) chick embryo grafted with MDA MB 231 cells resulting in vascularization and dissolution of tumor upon treatment with CQDs (Reprinted with permission from Prasad et al. (2016), Copyright© 2019, Elsevier), (f) control untreated cells and nuclear localization of anti-cancer drug, (g) doxorubicin in MCF7 cells upon free drug, and (h) Dox-CNP treatment (Reprinted with permission from Kumar et al. (2018), Copyright© 2018, American Chemical Society)

et al., 2016). Misra et al. have demonstrated the use of hyperspectral imaging to track the movement of phospholipid stabilized CNPs carrying drug inside MCF-7 cells. They have reported the ability of the technique to map and quantify the nanoparticles and drugs simultaneously without the use of fluorescent dyes (Misra et al., 2018).

For another important biological application of cancer cell-specific cellular internalization, CDs encapsulated in the folate-targeted nanoscale metal-organic framework (NMOF) were used as nanoprobes (Chowdhuri et al., 2016). The biocompatible CDs synthesized from the poly(vinyl alcohol) were also used as bioimaging probe in another case (Kundu et al., 2016). The CNPs functionalized with fluorescein, α-naphthylamine, and rhodamine B were used for the bioimaging of RBCs. The functionalization improved the fluorescence property of the particles while making them more biocompatible (Chandra et al., 2011). In similar studies, CDs synthesized hydrothermally from sources as simple as apple juice have been used to image bacteria such as *Mycobacterium tuberculosis* and *Pseudomonas aeruginosa* and fungus-like *Magnaporthe oryzae* with no toxic effects on the growth of the organisms (Mehta et al., 2015). The CDs synthesized from *Lantana camara* berries have shown their strong emission of red, blue, and green color in human breast adenocarcinoma MCF-7 and human embryonic kidney HEK-293 cells (Bandi et al., 2018). CDs prepared from Tulsi (*Ocimum tenuiflorum*) leaves have been successfully employed for the imaging of *Bacillus subtilis* and *Escherichia coli*. When excited with 405, 488, and 561 nm the particles show emission of blue, yellow, and red fluorescence, respectively (Bhatt et al., 2018). Bhamore et al. have used ultra-small fluorescent CDs synthesized from the *Acacia concinna* seeds (shikakai) for the bioimaging of *Penicillium sp*. Some of these CDs were found to enter the cell via endocytosis and got accumulated in the cytoplasm (Figure 7b; Bhamore, Jha, Park, & Kailasa, 2018). In another study, *Manikara zapota* fruit was used to synthesize multi-color emissive CDs, which have been proposed as bioimaging probe in bacterial (*E. coli*) and fungal cells (*Aspergillus aculeatus* and *Fomitopsis* sp.; Figure 7c,d). The CDs were found biocompatible when tested in Hela cells and showed blue, green, and yellow emission at excitation wavelengths of 443, 515, and 563 nm, respectively (Bhamore et al., 2019).

3.2 | Drug delivery

Delivery of drug, due to various reasons, requires a suitable carrier system which facilitates the improvement in functional effectivity and control to side effects. These properties have been achieved through different CNMs with loaded drugs or on being synthesized using some specific raw materials which have anti-cancer properties, intrinsically. In this direction, use of the CNMs for the delivery of cargo inside the cells has been reported in some previous studies. This includes the lipid-loaded perfluorocarbon nanoparticles (PFOB), which were shown to efficiently deliver therapeutic and imaging agents efficiently. The biocompatibility of these particles was studied in terms of complement activation using the hemolysis assay (Pham et al., 2014). A SWCNT-lipid formulation was reported to yield better transfection efficiency in comparison to commercially available transfection agent, Lipofectamine2000 (Misra et al., 2012). As Prasad et al. have demonstrated the inherent antitumor property of carbon quantum dots (CQDs) synthesized from 1,7′-dimethyl-2′-propyl-1H, 3′H-[2,5′] bibenzoimidazolyl (DPBI). Studies were performed against breast cancer cell line (MDA MB 231) in vitro and specific action against tumor cells in *ex ovo* chick chorioallantoic membrane (CAM) as an in vivo model. The activity of CQDs was found to be comparable to anticancer drug paclitaxel with no significant inhibitory effect against RBCs, WBCs, and normal embryonic epithelial cells. The chick embryo grafted with MDA MB 231 tumor on treatment with CQD resulted in tumor dissolution with normal development of limbs (Figure 7e; Prasad et al., 2016). The delivery system can be made more effective by coupling the carbon particles with drugs for various diseases. The controlled drug-delivery systems have gained traction for targeting specific cancer sites by incorporation of a sensing element in the drug delivery system. The sensing component of such as boronic acid–diol complex or hydrazine bond can respond to the changes occurring in its surrounding (pH) or to any given stimuli (Choi et al., 2018). CNPs presents a great opportunity for their functionalization due to the presence of various functional groups such as carboxylic and hydroxyl groups (Yang et al., 2011).

It is possible to modify the nature of the particles in an aqueous medium through surface functionalization. This approach can be effectively utilized by synthesizing bio-composites with cargo (drug) molecules for their effective internalization in the human cells. The surface chemistry of the CNPs has been exploited to study the interaction of the surface groups with the biological system to deliver drugs in cancer cell lines. Srivastava et al. (2017) have studied the effect of size and surface charge on the interaction between the CNPs and breast cancer cells. They have elucidated the selective endocytosis of the particles by the cancer cells with anionic phosphate passivated particles showing preference

toward metastatic cancer cells whereas, late-stage cancer cells had more susceptibility to internalize sulfonate functionalized particles.

In another study, CNPs coated with BSA were loaded with anticancer drug methotrexate. The formulation was tested to be hemocompatible and showed significant apoptosis against A549 lung cancer cell line (Muthukumar et al., 2014). The porous carbon nanospheres have been shown to deliver Doxorubicin (Dox), a potent anticancer drug through functionalization with polyethylenimine (PEI) and folic acid (FA) targeted towards Hela and MDA MB 231 cancer cells. The particles were selectively internalized by the cancer cells due to the presence of the excess amount of folate receptors in the cell surface (Kapri et al., 2018).

The CDs covalently functionalized with peptides through carbodiimide coupling method have been employed for bone tissue regeneration (Gogoi et al., 2017). The bio-nanohybrids formed by attachment of different peptides {SR-7 (angiogenic peptide), PS-11 (cell adhesion peptide), IP-3 (osteoblast differentiating peptide), and CK-23 (osteogenic peptide)} on CDs were mixed with tannic acid-based hyperbranched polyurethane matrix and blended with gelatin. The compatibility of the synthesized composite was tested against MG63 human osteoblast cell line and was found to have enhanced cytocompatibility of polyurethane while promoting the adherence and proliferation of the cells up to 7 days in vitro. Calcification and blood vessels were formed in mineralization and vascularization assays in vivo in murine model.

The cancer tissues can be targeted based on physiological cues of the cells and their microenvironment. As demonstrated by Kumar et al., the CNPs can be used as a carrier for the delivery of Dox in response to pH. A higher release of drug was observed at pH of 4.6 than pH 7.4 for a period of 24 h. The cytotoxicity studies revealed improvement in action of Dox against MCF-7 and SAS cancer cell lines for CNP-Dox treatment. The CNP-Dox showed improved localization of Dox in the nucleus (Figure 7f–h; Kumar et al., 2018). In a similar approach, mechanism of pH-dependent release of drug has been used for the delivery of glycopeptide antibiotic vancomycin using carbon quantum dots (CQD). Delivery was achieved in a calcium alginate hydrogel in gastrointestinal (GI) tract (Sarkar et al., 2017) for curcumin, an anticancer compound (Rai et al., 2017) and lisinopril a drug used in hypertension and renal diseases (Mehta et al., 2017).

3.3 | Sensing

Identification of the disease, severity, and post-therapy follow-ups are important features of any biomedical regimen. To achieve these goals sensing of biomolecules, biomechanisms, and phenomenon in biological systems need to be ascertained. CNPs have gained a significant reputation in field of sensing as well. In general, the emission property of the fluorophores is known to be highly influenced by the microenvironment around them. The interaction of fluorophore with a particular analyte present in the surrounding environment can change its fluorescence properties, which can serve as an indicator for the presence of that analyte. The interaction of metal nanoparticles such as gold and silver, semiconducting quantum dots, namely, CdSe, ZnS, CdSe/ZnS, and CdTe and CNTs with desired analytes have been used for such detection purposes (Chandra et al., 2020; Willner & Vikesland, 2018). Due to the inherent fluorescence property and availability of functional groups on the surface of CNPs, they have been used as sensors/probes for the detection of various heavy metals in polluted water bodies. The use of CNPs gives an added advantage of low toxicity over traditional semiconducting quantum dots (Jaiswal, Ghsoh, & Chattopadhyay, 2012). The fluorescent metallic as well as CNPs can be tuned by modifying the surface functional groups to respond to a particular analyte. The fluorescent particles can signal to presence of analytes by changing their fluorescent intensity. The fluorescence quenching and recovery are termed as "turn off" and "turn on" behavior, respectively (Baù et al., 2011). The CDs have also shown their potential to be used for the detection of various proteins in human serum. A machine learning-assisted array-based sensor has been developed by Pandit et al. (2019) for the detection of proteins. For this purpose, CDs having different surface passivation have been synthesized using substrates such as sucrose, gluconic acid, and PEG. The differences in the surface passivation have resulted in different interactions for all the proteins. The prepared CDs when arranged in an array on a 96-well plate give a signature pattern specific to that protein. These resulting patterns have been fed to machine-learning algorithms, which was able to differentiate all the eight proteins used in the study. Further, the application of CNPs for sensing has translated to their use in the biological systems for the detection of macromolecules such as nucleic acids and proteins. Li et al. have used CNPs to sense nucleic acid with selectivity down to a single-base mismatch. The study used a dye-labeled single-stranded DNA (ssDNA), which when got physically adsorbed on CNP surface via π–π interactions, quenched the fluorescence of the dye. In the presence of the target DNA, ssDNA pairing could result in the recovery of the fluorescence (Li et al., 2011). An aptamer-based biosensor for thrombin in

human serum has been reported by Wang et al., where Fluorescence Resonance Energy Transfer (FRET) phenomenon was utilized from upconverting phosphors (UCPs) to CNPs. The covalently attached aptamer to the UCPs, were reported to be interacting with π–π stacking interaction on CNP surface, which could lead to suppression of UCP fluorescence. It was achieved probable due to the close proximity of donor and acceptor entities. On the introduction of biomolecule thrombin into the system, aptamer attained a quadruplex structure to reduce the π–π interaction ending with restoration of UCP fluorescence. The sensor could detect thrombin in a linear range of 0.5–20 nM with an LOD of 0.18 nM in an aqueous buffer. Whereas an LOD of 0.25 nM was observed in the case of human serum (Wang et al., 2011). The CNPs have also been used for the development of a fluorometric immunoassay for the detection of plant *Citrus tristeza* virus (CTV). The immunoassay was able to detect up to 220 ng/ml of CTV (Shojaei et al., 2016).

In another set of studies, Sharma et al. have reported the use of turn-off mode of CNPs for the detection of palladium (Pd^{2+}) and mercury (Hg^{2+}) with the detection range of 5–100 and 1–18 μM, respectively. The limit of detection (LOD) was found to be 58 nM for Pd^{2+} and 100 nM for Hg^{2+} (Sharma et al., 2016). A much lower LOD of 6 nM for Hg^{2+} has been reported by Bano et al. using the CQDs with turn-off sensing with a detection range of 0 to 0.1 μM. The sensor can further act as a turn-on sensor for glutathione detection (Bano et al., 2018). Gupta et al. have also reported a similar LOD of 6.8 nM for Hg^{2+} using nitrogen-doped PEGylated CDs. They also observed a significant decrease in LOD to 18 pM after functionalization with DTT (Dithiothreitol; Gupta et al., 2015).

The CNDs synthesized from microwave-assisted pyrolysis of trisodium citrate and sodium thiosulphate have shown a selective low detection limit of 32 pM for arsenic [As (III)] in the presence of other metal ions. When these CNDs were tested for selectivity towards biothiols, they showed a specific behavior towards glutathione (GSH) even in the presence of other bio-thiols such as cysteine (Cys) and homo-cysteine (H-cys) in blood plasma. The detection limit for GSH was found to be 43 nM (Gupta, Verma, Khan, & Nandi, 2016). In another highly sensitive sensing approach for As (III), ratiometric fluorescence response of carbon-based nanohybrid system comprising glutathione-functionalized reduced CDs (GSH-f-rCDs) and graphene quantum dots (GQDs) has been used by Gogoi et al. (2019). The reduced CDs used herein were produced using sodium borohydride and possessed superior fluorescence characteristics than pristine form. The color variation of the sensory liquid due to ratiometric change in intensity was observed to be dose-dependent with a lower limit of detection of 0.5 ppb. The strategy was also successfully employed to detect As (III) on nanohybrid coated test papers (Figure 8d; Gogoi et al., 2019).

The CNPs have also been used for the detection of pollutant ions such as fluoride ion in water (Boruah et al., 2020), sulfide ion (S^{2-}), and gold ion (Au^{3+}; Sharma, Kaur, Tiwari, Saini, & Mobin, 2018), Aluminium (Al^{3+}; Bhamore, Jha, Singhal, et al., 2018), iron (Fe^{3+}; Bandi et al., 2016; Kainth et al., 2020; Sahoo et al., 2020), copper (Cu^{2+}; Bhamore, Jha, Park, & Kailasa, 2018; Kumari et al., 2018; Murugan et al., 2019), and chromium (Pooja et al., 2019). Sharma et al. showed successful intracellular quenching of fluorescence of CDs upon sensing Au^{3+} with the help of flow cytometric analysis (Figure 8a–c; Sharma, Kaur, Tiwari, Saini, & Mobin, 2018). The other application of CNPs includes their use as a probe for sensing intracellular pH and cell imaging in cancer cells (Figure 8e; Pal et al., 2019; Sharma, Kaur, Tiwari, & Mobin, 2018). The nitrogen and sulfur co-doped CQDs have been applied for the detection of nitrophenols (Soni & Pamidimukkala, 2018). The carbon nanocubes (CNCs) of ∼5 nm have been derived from a natural source (mahua flowers) and employed for the detection of antibiotics, nitrofurazone, and sulfamethoxazole by modification of glassy carbon electrode with an LOD of 80 and 13 μM, respectively (Srinivasan et al., 2020). Besides sensing CNMs can also be used for removal of contaminants as has been shown in Figure 8f.

4 | CORRELATION OF SYNTHESIS, CHARACTERISTICS, AND BIOLOGICAL APPLICATION OF CNPs

From the beginning of acquiring from natural sources to preparation using synthetic protocols, CNMs have traveled a long road in achieving a niche as advance as shown by various CNPs developed in recent years. Reports of various used synthetic methods, characterization protocols and application in biological systems for CNPs are already available but a correlation in these different dimensions of existence for CNPs is required to generate a better next edition of it. In general, novel CNPs are produced with either intention of achieving a characteristic which might be able to influence various biological outcomes or by assembling various features on the same CNP which might be required to solve a specific biological problem. Both regimens can be successful only if optimized source and method of CNP synthesis is evaluated by appropriate characterization methods and utilized in most suitable biological systems using improvised protocols.
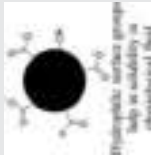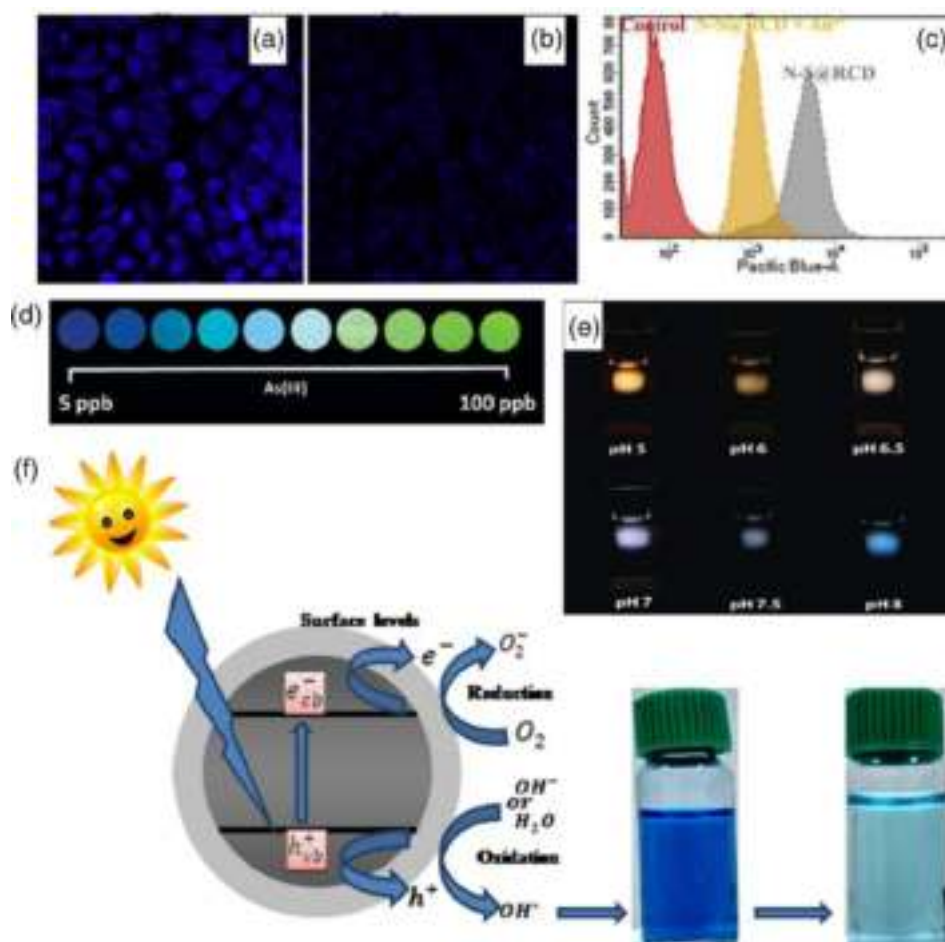
FIGURE 8 Confocal (panel a and b) and (c) flow cytometric analysis of HeLa cells treated with CDs and $CD^+ Au^{3+}$ (Reprinted with permission from Sharma, Kaur, Tiwari, and Mobin (2018), Copyright© 2018, Elsevier), (d) As (III) detection based on the change in the color of paper coated with GSH-f-rCD/GQD (Reprinted with permission from Gogoi et al. (2019), Copyright© 2019, Royal Chemical Society), (e) change in the color of the composite prepared using CDs/PVA at varied pH upon excitation at 380 nm (Reprinted with permission from Pal et al. (2019), Copyright© 2019, Wiley), (f) schematic illustration of electron transfer in the presence of sunlight and decoloration of MB dye (Reprinted with permission from Ramar et al. (2018). Copyright© 2018, Elsevier)

As reported by various research groups, CNPs produced through certain source materials and passivation via specific synthetic protocol could make them suitable for certain biological applications (Table 2). In some of the conditions, it was revealed that charge on the particle surface, as characterized as zeta potential, can greatly influence CNPs interaction with the surrounding environment during intracellular delivery. It established that the positively charged CNPs can be better internalized by certain cells but can bind nonspecifically to proteins in the blood stream as well (Breus et al., 2009; Park et al., 2011). On the other side, the negatively charged particles mostly enter the cells through specific receptors but provide the advantage of reduced interaction with proteins of blood plasma. Simultaneously, these negatively charged CNPs can interact with nuclei having pH of ∼0.3–0.5 units higher than cytosol. These features could be motivation for the synthesis of the zwitterionic CDs by Jung et al., 2015. It could be achieved from citric acid source passivated with β-alanine using microwave pyrolysis. CNPs produced by this combination possessed both positive and negative surface functional groups and could be delivered along the loaded drugs to the cell nucleus with minimal interaction with proteins of blood circulation. The zwitterionic particles show better colloidal stability over a wide pH range and are less prone to nonspecific protein aggregation, thus, resulting in the longer circulation time and enhanced tumor accumulation. The CDs were found to be internalized in the nucleus after the incubation period of 24 h which was confirmed by a strong fluorescent signal from the nucleus. This reveals the merely use of various combinations of different source materials can generate CNPs of combined characteristics and can provide biological efficiencies of choice (Table 2).

TABLE 2 Some important biological applications of CNPs and correlation with source material, passivating agent, mode of synthesis, and characteristics responsible for the probable mode of action

Source material	Passivating agent/conjugation	Method of synthesis	Property of CNPs	Methods of characterization	Biological efficiency	Probable mode of utilization	References
Citric acid	β-Alanine	one-step microwave pyrolysis	Nanometer-scale	DLS, TEM, AFM	Stability in blood circulation, Entry into the tumor tissue, enhanced permeability, and retention		Jung et al., 2015
	Diethylenetriamine, Dimethylmaleic acid (DMMA)	Thermal pyrolysis	Possibility of surface modification	FTIR, NMR	Stimuli-responsive drug carrier, Biosensing, intracellular hybridization		Feng et al., 2016, Ostadhossein & Pan, 2017
Agave nectar	Linear PEG, branched polyethylenimine (PEI)	Hydrothermal	Surface hydrophilicity/hydrophobicity/Stability	Zeta potential, Contact angle measurements	Solubility/suspendability in physiological fluid to help in circulation through blood		Srivastava et al., 2017
	PEG, poly-L-lysine	Hydrothermal	Biocompatibility	MTT assay	Interacts with physiological system with/without any toxicity		Reprinted from Misra, Chang, et al., 2015
	Cationic PEI, polypeptidic poly L-lysine (polyLys) and dendritic poly amidoamine (PAMAM+), anionic sodium dodecyl sulfate (SDS), nonionic polyethylene glycolcetylether (PEGCE)	Hydrothermal	Optical property	Absorption and fluorescence spectroscopy	Bioimaging		Misra, Ostadhossein, et al., 2017
Molasses	Poly (N-isopropylacrylamide), Multiarm polyethylene glycol	Hydrothermal		Raman imaging			Mukherjee et al., 2015
Ascorbic acid and L-arginine	Conjugation with Fluorescein isothiocyanate (FITC)	Hydrothermal	Nonlinear optical property	Two-photon microscopy	Deep tissue imaging		Reprinted with permission from Lesani et al., 2020

(Continues)

TABLE 2 (Continued)

Source material	Passivating agent/conjugation	Method of synthesis	Property of CNPs	Methods of characterization	Biological efficiency	Probable mode of utilization	References
1,2,4,5-Benzenetetracarboxylic acid	2,7-diaminofluorene	Solvothermal synthesis and separation through silica column chromatography	High polarity	Fluorescence spectroscopy	Bioimaging using emission in the red region		Reprinted with permission from Nguyen et al., 2020
			Low polarity	Fluorescence spectroscopy	Bioimaging using emission in the blue region		
Proline	Ethylenediamine and Folate acid	Hydrothermal	Selectively targeted and endocytosed by folate receptor-positive MCF-7 cells	Confocal microscopy	Selective targeting of folate-receptor expressing cancer cells		Reprinted with permission from Jiao et al, 2019
			Relatively less endocytosed by HepG2 cells presenting low number of folate receptors				
			Not endocytosed by folate receptor-negative PC-12 cells				
Maleic acid and butane1,4-diamine	Diblock copolymer poly[sodium (carboxylate sulfamate) isoprene]-b-poly(ethylene oxide) (CSS-IEO-3)	Hydrothermal	Fluorescence quenching in presence of Fe^{3+}	Titration followed by fluorescence spectroscopy	Metal ion (Fe^{3+}) sensing		Skaltsas et al., 2016, Skaltsas et al., 2017
Sucrose, nitrobenzene, and nitrosobenzene	Oligonucleotide	Hydrothermal	Red fluorescence CDs	Confocal microscopy	Detection and targeting of intracellular biomolecular targets including nucleic acids		Reprinted with permission from Srivastava et al., 2020
			Green fluorescence CDs				

TABLE 3 A comparison of properties associated with biological application between carbon nanomaterials and other QDs

S. No.	Property	CNPs/ CQD/CDs	Gold NPs/gold QDs	CdSe QDs	PbS QDs	Si QDs
1	Optical emission	Tunable, (Fathi et al., 2021, Srivastava et al., 2021)	Enabled upon specific encapsulation (Olesiak-Banska et al., 2019, Zheng et al., 2004)	Tunable (Liu, Robinson, et al., 2008)	Tunable (Hou et al., 2017)	Tunable (Dohnalová et al., 2013)
2	Quantum Yield	Low (Srivastava et al., 2021)	High (Zheng et al., 2004)	High (Zhou et al., 2015)	High (Peterson & Krauss, 2006)	High (May et al., 2012)
3	Biocompatibility	High (Gil et al., 2021), Misra, Chang, et al., 2015)	High (Bolaños et al., 2019)	Low (Improvement requires surface functionalization; McHugh et al., 2018)	Low (Gil et al., 2021, Moitra, Alafeef, et al., 2021)	High (Du et al., 2021, Erogbogbo et al., 2008)
4	Biodegradability	High (Srivastava, Khamo, et al., 2019)	Low (Balfourier et al., 2020)	low (McHugh et al., 2018)	Low (Gil et al., 2021)	High (Du et al., 2021)
5	Source material	Vast range of organic compounds	Limited to Au salts	Limited to Cd and Se precursors	Limited to Pb and S containing compounds	Limited to Si containing compounds
6	Bioavailability	High (Li et al., 2019)	Low (Improvement requires surface functionalization; Bolaños et al., 2019, Tsoi et al., 2016),	Poor (Improvement requires surface functionalization; McHugh et al., 2018, Tsoi et al., 2016)	Low (Improvement requires surface functionalization; Gil et al., 2021)	Poor (Improvement requires surface functionalization; Erogbogbo et al., 2008)

In another study, Feng et al. had synthesized charge-convertible CDs from citric acid with surface passivation with DMMA using thermal pyrolysis as synthetic method which can have changes in their surface charge depending on the surrounding pH. The anionic DMMA polymers were used on the surface of synthesized CDs which could undergo charge conversion to a cationic polymer under mildly acidic conditions as confirmed by zeta potential measurement. The conversion to a cationic polymer led to strong electrostatic repulsion thus resulting in release of the prodrug containing positively charged CDs. These released positively charged CDs have high affinity for the negatively charged cancer cell membrane which helps in better internalization in cancer cells. The negative charge on the surface of the drug carrier enables them to have longer circulation time. The particles were found to have enhanced accumulation in the tumor due to the EPR effect. The charge conversion property further reduces the internalization of the drug into the normal cells as the release occurs only in slight acidic environment of cancer cells thus helping in reducing the side effects (Feng et al., 2016). Success of these CNPs emphasizes that dual properties could even be achieved by introducing inter-convertible chemistries rather than mixing two separate components with individual properties while keeping all other protocols same (Table 2).

The surface charge and size of the particles can also influence the mode of internalization of the cells into the cells. The cancer cells at different stages of progression could be more susceptible to particles with a certain charge. As Srivastava et al. have shown that CNPs prepared from Agave Nectar passivated with PEG and PEI, could internalize the early stage MCF-7 breast cancer cell line, PEG and sulfonate functionalized particles followed a specific endocytic pathway. The pristine CNPs were found to enter the MCF-7 cells through a nonspecific internalization route, as they were nonresponsive to the inhibitors used to block the specific pathways. However, the CNPs presenting thiol groups on the surface did not gain significant entry inside the cells. The formation of carbonaceous core was confirmed using Raman spectroscopy whereas surface passivation was confirmed from FTIR and NMR. On the other hand, MDA-MB-231 a late-stage breast cancer cell line allowed the higher internalization of PEG400, positive, and phosphate group

bearing CNPs via the lipid raft-mediated pathway. They have also shown that the pristine CNPs enter the BT-549 cells via the clathrin-mediated pathway whereas high molecular weight PEGylated CNPs used multiple endocytic pathways and small molecular weight PEGylated CNPs followed energy-dependent pathway for internalization. The positively charged CNPs were found to enter the cell via the clathrin- and dynamin-dependent pathway whereas negatively charged particles did not show any specific pathway (Srivastava et al., 2017). This study was important to understand the role of passivating agents and modulation in the interaction pattern of CNPs with different cancer cells of different stages (Table 2).

Misra, Chang, et al. (2015) reported that surface passivation of PEI and PAMAM on CNPs, showed lower biocompatibility while neutral or negatively charged passivations were of excellent biocompatible nature as in the case of pristine CNPs. The application of excellent optical emission property of CNP prepared from the same natural source, agave nectar, by hydrothermal method could be used for bioimaging application which was applicable for drug delivery application with minimum cytotoxicity of its own in various cancer cell lines. It indicates that surface chemistry generated by a certain synthesis mechanism would be critical factor even in deciding biocompatibility and optical properties rather than the material used in the core of the CNP (Table 2).

An alternative method of generating variations in surface properties of CNPs by post-coating could be used successfully for sensing intracellular activities rather than passivating the system during the synthesis process. It was found that the use of different surface passivating agents can switch on and switch off the fluorescence emission of CNPs indicating that the presence of certain conditions inside the cells could be read via change in optical properties of CNP (Misra, Srivastava, et al., 2017). The presence of G and D bands in the Raman spectra of CNPs prepared with molasses and passivated with Poly (N-isopropylacrylamide)/Multiarm polyethylene glycol was valuable for Raman imaging inside the biological tissues (Mukherjee et al., 2015). Conjugation of fluorescein isothiocyanate on the surface of nitrogen-doped CNPs prepared from ascorbic acid and L-arginine by hydrothermal method could give two-photon optical property. It was characterized by obtaining the quadratic relationship between excitation laser power and fluorescence intensity. This property was found to be suitable for deep tissue imaging as shown by Lesani et al. (2020) inside the pig skin (Table 2).

Nguyen et al. (2020) have shown the effect of surface polarity on the emission pattern of the particles. The particles synthesized from 1,2,4,5-benzenetetracarboxylic acid and passivated with 2,7-diaminofluorene from solvothermal treatment were separated using silica column chromatography, where they were able to retrieve particles with four different polarities. As expected, the particles with high polarity due to the presence of more oxygen defects on the surface gave fluorescence emission in the red region of the spectrum whereas the less polar particles were found to have emission in blue, green, and yellow regions depending on their polarities. The effect of polarity on the emission of the particles can be used to fine-tune the optical properties to obtain particles having emission in the red region of the spectrum. This could provide an opportunity to synthesize particles with desired emission patterns using facile synthesis methods (Table 2).

The targeting efficiency of the surface-functionalized CNPs can be tested against different cell lines having various membrane receptors. The produced CNPs can be modified to target specific receptors present in the cancer cells. Jiao et al. have synthesized CNPs from proline and ethylenediamine, which were further conjugated with folate acid to make them targeted toward folate receptor expressing cells. They have shown the selectivity of the particles using the folate receptor expressing MCF-7 cells. The selectivity was confirmed using confocal microscopy wherein a strong signal was observed in the case of MCF-7 cells in comparison to HepG2 cells which have a smaller number of folate receptors on the surface. When tested in PC-12 cells, which do not express folate receptors, no fluorescence was observed indicating the internalization of particles selectively by the folate receptor-expressing cells via receptor-mediated endocytosis (Jiao et al., 2019). It revealed that though all the processes were same for synthesis of these CNPs, a varying biological property was achieved inside different cell systems (Table 2).

The use of optical properties of CNPs has been utilized in the field of sensing by different research groups as in by Skaltsas et al. where they had functionalized the amine rich surface of CQDs with diblock copolymer poly[sodium(carboxylate sulfamate) isoprene]-b-poly(ethylene oxide) (CSS-IEO-3) for the detection of Fe^{3+}. The interaction between Fe^{3+} and the anionic centers of CSS-IEO-3 resulted in the loss of emission from CQDs within CQD/CSS-IEO-3 mixture at 420 nm (Table 2). The decrease in the emission of CQDs could be correlated with the concentration of Fe^{3+} present in the system (Skaltsas et al., 2017). This approach can be translated to detection of other cations in biological systems with the use of CNPs carrying negatively charged surface with minimal change in preparation protocols.

In one of the other studies, Srivastava et al. employed the oligonucleotide conjugated CDs with red and green fluorescence for the detection of intracellular targets. They synthesized CDs through hydrothermal method using sucrose as the precursor molecule upon which the addition of nitrobenzene and nitrosobenzene resulted in red and green CDs,

respectively. The conjugation of CDs with complementary single-stranded oligonucleotides made them FRET pair, which on hybridization resulted in the quenching of their fluorescence (Table 2). The oligonucleotide conjugated CDs could be used as a probe for the detection of GADPH mRNA through the formation of duplex of GADPH mRNA and its complimentary single-stranded DNA on the CDs. This pairing resulted in the quenching of fluorescence detected using confocal microscopy (Srivastava et al., 2020). These representative examples of CNPs successfully correlate the source material, passivating agents, post coating materials, synthesis process, and characterization with eventual biological properties of CNPs. Further investigation and utilization of some of these variables in new combination might be able to generate a new edition of CNPs for better biological outcomes.

5 | CONCLUSION

CNMs have emerged as one of the most advanced materials for utilization in biological systems for various applications ranging from imaging, sensing to delivery of drugs. It has been established in the recent past that the materials and methods used to produce these CNMs and techniques of unique characterizations, establishes their use for specific application. This interesting controllability on the fate of produced CNMs, make it wanted by the research community. In this regard, a compilation and correlation of available data on material, method of CNM synthesis, advantages of certain characterizations, and advanced ways of utilizations in form of a review can guide some of the future studies. This review introduces the well-known carbon nanostructures, namely CNTs, fullerenes, and graphene, in terms of their revolutionary role and beneficent potential to impart material and medical benefits. It further covers the new form of nanocarbons, including CDs and CNPs about synthetic procedures, different properties, and diverse biological applications. Although in some previous reports, CNPs have been discussed for these aspects but still there is no comprehensive information available on correlation between these aspects which can reveal that's why and how CNPs have gained status of one of the best materials for various biological applications. Focus of this review introduces the brief, but progressive discussion about CNPs which can help in attaining the basic understanding about compositional and structural aspect of the carbon nanostructures. This has been associated with their distinct properties and use in bioimaging, drug delivery, and biosensing, which are considered as three of the most important domains for biological applications of a material. This review also emphasizes that research endeavors in the field of carbon nanostructures dealing with control over defined structures and size, specificity in surface chemistry, composition of bulk, unique optical property, aqueous suspendability, biocompatibility, and economic productivity is challenging but may provide significant flexibility to optimize it for specific purpose. Trend of advancement and adaptation of novel edition of CNPs by various research groups mainly indicates that fundamental understanding of this biocompatible nanoform of ubiquitous carbon can lead to exciting developments in future as well. It is expected that in this stint of finding novel, improvised, and specialized editions of CNPs, this collection of information will be able to contribute its own share.

CONFLICT OF INTEREST
The authors have declared no conflicts of interest for this article.

AUTHOR CONTRIBUTIONS
Niranjan Chatterjee: Writing – original draft (equal). **Piyush Kumar:** Writing – original draft (equal). **Krishan Kumar:** Writing – review and editing (supporting). **Santosh Misra:** Conceptualization (lead); resources (lead); supervision (lead); writing – review and editing (lead).

DATA AVAILABILITY STATEMENT
Data sharing is not applicable to this article as no new data were created or analyzed in this study.

ORCID
Piyush Kumar https://orcid.org/0000-0002-9124-5657
Santosh K. Misra https://orcid.org/0000-0002-3313-4895

RELATED WIREs ARTICLES
Functional carbon nanodots for multiscale imaging and therapy
Fluorescent carbon dots as intracellular imaging probes

FURTHER READING
Ray, S. C., & Jana, N. R. (2017). Chapter 1—Different synthesis process of carbon nanomaterials for biological applications. In *Carbon Nanomaterials for Biological and Medical Applications. Micro and Nano Technologies* (pp. 1–41). Elsevier. https://doi.org/10.1016/B978-0-323-47906-6.00001-1
Ray, S. C., & Jana, N. R. (2017). Chapter 3—Application of carbon-based nanomaterials as biosensor. In *Carbon Nanomaterials for Biological and Medical Applications. Micro and Nano Technologies* (pp. 87–127). Elsevier. https://doi.org/10.1016/B978-0-323-47906-6.00003-5

REFERENCES
Aggarwal, R., Saini, D., Singh, B., Kaushik, J., Garg, A. K., & Sonkar, S. K. (2020). Bitter apple peel derived photoactive carbon dots for the sunlight induced photocatalytic degradation of crystal violet dye. *Solar Energy*, *197*, 326–331.
Ali, H., Bhunia, S. K., Dalal, C., & Jana, N. R. (2016). Red fluorescent carbon nanoparticle-based cell imaging probe. *ACS Applied Materials and Interfaces*, *8*(14), 9305–9313.
Ali, H., Ghosh, S., & Jana, N. R. (2020). Fluorescent carbon dots as intracellular imaging probes. *WIREs Nanomedicine and Nanobiotechnology*, *12*(4), e1617.
Arul, V., Edison, T. N. J. I., Lee, Y. R., & Sethuraman, M. G. (2017). Biological and catalytic applications of green synthesized fluorescent N-doped carbon dots using Hylocereus undatus. *Journal of Photochemistry and Photobiology B: Biology*, *168*, 142–148.
Baker, M. (2010). Nanotechnology imaging probes: Smaller and more stable. *Nature Methods*, *7*(12), 957–962.
Baker, S. N., & Baker, G. A. (2010). Luminescent carbon nanodots: Emergent nanolights. *Angewandte Chemie International Edition*, *49*(38), 6726–6744.
Bakry, R., Vallant, R. M., Najam-ul-Haq, M., Rainer, M., Szabo, Z., Huck, C. W., & Bonn, G. K. (2007). Medicinal applications of fullerenes. *International Journal of Nanomedicine*, *2*(4), 639.
Balfourier, A., Luciani, N., Wang, G., Lelong, G., Ersen, O., Khelfa, A., Alloyeau, D., Gazeau, F., & Carn, F. (2020). Unexpected intracellular biodegradation and recrystallization of gold nanoparticles. *Proceedings of the National Academy of Sciences of the United States of America*, *117*(1), 103–113.
Bandi, R., Dadigala, R., Gangapuram, B. R., & Guttena, V. (2018). Green synthesis of highly fluorescent nitrogen-doped carbon dots from Lantana camara berries for effective detection of lead(II) and bioimaging. *Journal of Photochemistry and Photobiology B: Biology*, *178*, 330–338.
Bandi, R., Gangapuram, B. R., Dadigala, R., Eslavath, R., Singh, S. S., & Guttena, V. (2016). Facile and green synthesis of fluorescent carbon dots from onion waste and their potential applications as sensor and multicolour imaging agents. *RSC Advances*, *6*(34), 28633–28639.
Bano, D., Kumar, V., Singh, V. K., & Hasan, S. H. (2018). Green synthesis of fluorescent carbon quantum dots for the detection of mercury(ii) and glutathione. *New Journal of Chemistry*, *42*(8), 5814–5821.
Baù, L., Tecilla, P., & Mancin, F. (2011). Sensing with fluorescent nanoparticles. *Nanoscale*, *3*(1), 121–133.
Bhamore, J. R., Jha, S., Park, T. J., & Kailasa, S. K. (2018). Fluorescence sensing of Cu^{2+} ion and imaging of fungal cell by ultra-small fluorescent carbon dots derived from Acacia concinna seeds. *Sensors and Actuators, B: Chemical*, *277*(August), 47–54.
Bhamore, J. R., Jha, S., Park, T. J., & Kailasa, S. K. (2019). Green synthesis of multi-color emissive carbon dots from Manilkara zapota fruits for bioimaging of bacterial and fungal cells. *Journal of Photochemistry and Photobiology B: Biology*, *191*(December 2018), 150–155.
Bhamore, J. R., Jha, S., Singhal, R. K., Park, T. J., & Kailasa, S. K. (2018). Facile green synthesis of carbon dots from *Pyrus pyrifolia* fruit for assaying of Al^{3+} ion via chelation enhanced fluorescence mechanism. *Journal of Molecular Liquids*, *264*, 9–16.
Bhatt, S., Bhatt, M., Kumar, A., Vyas, G., Gajaria, T., & Paul, P. (2018). Green route for synthesis of multifunctional fluorescent carbon dots from Tulsi leaves and its application as Cr(VI) sensors, bio-imaging and patterning agents. *Colloids and Surfaces B: Biointerfaces*, *167*, 126–133.
Bhattacharjee, S., Samanta, S. K., Moitra, P., Pramoda, K., Kumar, R., Bhattacharya, S., & Rao, C. N. R. (2015). Nanocomposite made of an oligo (p-phenylenevinylene)-based trihybrid thixotropic metallo (organo) gel comprising nanoscale metal–organic particles, carbon nanohorns, and silver nanoparticles. *Chemistry—A European Journal*, *21*(14), 5467–5476.
Bhattacharya, K., Mukherjee, S. P., Gallud, A., Burkert, S. C., Bistarelli, S., Bellucci, S., Bottini, M., Star, A., & Fadeel, B. (2016). Biological interactions of carbon-based nanomaterials: From coronation to degradation. *Nanomedicine*, *12*, 333–351.
Bhunia, S. K., Pradhan, N., & Jana, N. R. (2014). Vitamin B1 derived blue and green fluorescent carbon nanoparticles for cell-imaging application. *ACS Applied Materials & Interfaces*, *6*(10), 7672–7679.
Bhunia, S. K., Saha, A., Maity, A. R., Ray, S. C., & Jana, N. R. (2013). Carbon nanoparticle-based fluorescent bioimaging probes. *Scientific Reports*, *3*, 1473.
Bolaños, K., Kogan, M. J., & Araya, E. (2019). Capping gold nanoparticles with albumin to improve their biomedical properties. *International Journal of Nanomedicine*, *14*, 6387–6406.
Boruah, A., Saikia, M., Das, T., Goswamee, R. L., & Saikia, B. K. (2020). Blue-emitting fluorescent carbon quantum dots from waste biomass sources and their application in fluoride ion detection in water. *Journal of Photochemistry and Photobiology B: Biology*, *209*(June), 111940.

Breus, V. V., Heyes, C. D., Tron, K., & Nienhaus, G. U. (2009). Zwitterionic biocompatible quantum dots for wide pH stability and weak non-specific binding to cells. *ACS Nano*, *3*(9), 2573–2580.

Chandra, A., Prasad, S., Gigli, G., & del Mercato, L. L. (2020). Fluorescent nanoparticles for sensing. In *Frontiers of nanoscience* (Vol. 16, 1st ed.). Elsevier Ltd..

Chandra, S., Das, P., Bag, S., Laha, D., & Pramanik, P. (2011). Synthesis, functionalization and bioimaging applications of highly fluorescent carbon nanoparticles. *Nanoscale*, *3*, 1533–1540.

Chen, J., Chen, S., Zhao, X., Kuznetsova, L. V., Wong, S. S., & Ojima, I. (2008). Functionalized single-walled carbon nanotubes as rationally designed vehicles for tumor-targeted drug delivery. *Journal of the American Chemical Society*, *130*(49), 16778–16785.

Choi, C. A., Lee, J. E., Mazrad, Z. A. I., In, I., Jeong, J. H., & Park, S. Y. (2018). Redox- and pH-responsive fluorescent carbon nanoparticles-MnO$_2$-based FRET system for tumor-targeted drug delivery in vivo and in vitro. *Journal of Industrial and Engineering Chemistry*, *63*, 208–219.

Choudhary, N., Hwang, S., & Choi, W. (2014). Carbon nanomaterials: A review. In B. Bhushan, D. Luo, S. R. Schricker, W. Sigmund, & S. Zauscher (Eds.), *Handbook of nanomaterials properties* (pp. 709–769). Springer.

Chowdhuri, A. R., Singh, T., Ghosh, S. K., & Sahu, S. K. (2016). Carbon dots embedded magnetic nanoparticles @chitosan @metal organic framework as a Nanoprobe for pH sensitive targeted anticancer drug delivery. *ACS Applied Materials and Interfaces*, *8*(26), 16573–16583.

Clancy, A. J., Bayazit, M. K., Hodge, S. A., Skipper, N. T., Howard, C. A., & Shaffer, M. S. (2018). Charged carbon nanomaterials: Redox chemistries of fullerenes, carbon nanotubes, and graphenes. *Chemical Reviews*, *118*(16), 7363–7408.

Das, T., Saikia, B. K., Dekaboruah, H. P., Bordoloi, M., Neog, D., Bora, J. J., Lahkar, J., Narzary, B., Roy, S., & Ramaiah, D. (2019). Blue-fluorescent and biocompatible carbon dots derived from abundant low-quality coals. *Journal of Photochemistry and Photobiology B: Biology*, *195*(January), 1–11.

Deng, J., Lu, Q., Mi, N., Li, H., Liu, M., Xu, M., Tan, L., Xie, Q., Zhang, Y., & Yao, S. (2014). Electrochemical synthesis of carbon nanodots directly from alcohols. *Chemistry—A European Journal*, *20*(17), 4993–4999.

Ding, H., Yu, S. B., Wei, J. S., & Xiong, H. M. (2016). Full-color light-emitting carbon dots with a surface-state-controlled luminescence mechanism. *ACS Nano*, *10*(1), 484–491.

Dohnalová, K., Poddubny, A. N., Prokofiev, A. A., De Boer, W. D., Umesh, C. P., Paulusse, J. M., Zuilhof, H., & Gregorkiewicz, T. (2013). Surface brightens up Si quantum dots: Direct bandgap-like size-tunable emission. *Light: Science & Applications*, *2*(1), e47.

Du, G., Li, G., Qiu, S., Liu, L., Zheng, Y., & Liu, X. (2021). Low-cost water soluble silicon quantum dots and biocompatible fluorescent composite films. *Particle & Particle Systems Characterization*, *38*(11), 2100173.

Duan, P., Zhi, B., Coburn, L., Haynes, C. L., & Schmidt-Rohr, K. (2020). A molecular fluorophore in citric acid/ethylenediamine carbon dots identified and quantified by multinuclear solid-state nuclear magnetic resonance. *Magnetic Resonance in Chemistry*, *58*(11), 1130–1138.

Erogbogbo, F., Yong, K. T., Roy, I., Xu, G., Prasad, P. N., & Swihart, M. T. (2008). Biocompatible luminescent silicon quantum dots for imaging of cancer cells. *ACS Nano*, *2*(5), 873–878.

Fang, X., Li, X. Q., Wang, H., Wu, X. M., & Wang, G. L. (2018). Tuning surface states to achieve the modulated fluorescence of carbon dots for probing the activity of alkaline phosphatase and immunoassay of α-fetoprotein. *Sensors and Actuators B: Chemical*, *257*, 620–628.

Fathi, P., Moitra, P., McDonald, M. M., Esch, M. B., & Pan, D. (2021). Near-infrared emitting dual-stimuli-responsive carbon dots from endogenous bile pigments. *Nanoscale*, *13*(31), 13487–13496.

Feng, T., Ai, X., An, G., Yang, P., & Zhao, Y. (2016). Charge-convertible carbon dots for imaging-guided drug delivery with enhanced in vivo cancer therapeutic efficiency. *ACS Nano*, *10*(4), 4410–4420.

Ferro, S. (2002). Synthesis of diamond. *Journal of Materials Chemistry*, *12*(10), 2843–2855.

Gartia, M. R., Misra, S. K., Ye, M., Schwartz-Duval, A., Plucinski, L., Zhou, X., Kellner, D., Labriola, L. T., ... Pan, D. (2015). Point-of-service, quantitative analysis of ascorbic acid in aqueous humor for evaluating anterior globe integrity. *Scientific Reports*, *5*(1), 1–15.

Ghosh, S., Ali, H., & Jana, N. R. (2019). Water dispersible red fluorescent carbon nanoparticles via carbonization of resorcinol. *ACS Sustainable Chemistry & Engineering*, *7*(14), 12629–12637.

Gil, H. M., Price, T. W., Chelani, K., Bouillard, J. S. G., Calaminus, S. D. J., & Stasiuk, G. J. (2021). NIR-quantum dots in biomedical imaging and their future. *iScience*, *24*, 102189.

Gogoi, S., Devi, R., Dutta, H. S., Bordoloi, M., & Khan, R. (2019). Ratiometric fluorescence response of a dual light emitting reduced carbon dot/graphene quantum dot nanohybrid towards as(iii). *Journal of Materials Chemistry C*, *7*(33), 10309–10317.

Gogoi, S., Maji, S., Mishra, D., Devi, K. S. P., Maiti, T. K., & Karak, N. (2017). Nano-bio engineered carbon dot-peptide functionalized water dispersible Hyperbranched polyurethane for bone tissue regeneration. *Macromolecular Bioscience*, *17*(3), 1–15.

Goodarzi, S., Da Ros, T., Conde, J., Sefat, F., & Mozafari, M. (2017). Fullerene: Biomedical engineers get to revisit an old friend. *Materials Today*, *20*(8), 460–480.

Gupta, A., Chaudhary, A., Mehta, P., Dwivedi, C., Khan, S., Verma, N. C., & Nandi, C. K. (2015). Nitrogen-doped, thiol-functionalized carbon dots for ultrasensitive hg(ii) detection. *Chemical Communications*, *51*(53), 10750–10753.

Gupta, A., Verma, N. C., Khan, S., & Nandi, C. K. (2016). Carbon dots for naked eye colorimetric ultrasensitive arsenic and glutathione detection. *Biosensors and Bioelectronics*, *81*, 465–472.

Gupta, A., Verma, N. C., Khan, S., Tiwari, S., Chaudhary, A., & Nandi, C. K. (2016). Paper strip based and live cell ultrasensitive lead sensor using carbon dots synthesized from biological media. *Sensors and Actuators, B: Chemical*, *232*, 107–114.

Hauert, R. (2003). A review of modified DLC coatings for biological applications. *Diamond and Related Materials*, *12*(3–7), 583–589.

He, D., Li, X., He, X., Wang, K., Tang, J., Yang, X., & Zou, Z. (2015). Noncovalent assembly of reduced graphene oxide and alkyl-grafted mesoporous silica: An effective drug carrier for near-infrared light-responsive controlled drug release. *Journal of Materials Chemistry B*, *3*(27), 5588–5594.

Hirsch, A. (2010). The era of carbon allotropes. *Nature Materials*, *9*(11), 868–871.

Hong, G., Diao, S., Antaris, A. L., & Dai, H. (2015). Carbon nanomaterials for biological imaging and nanomedicinal therapy. *Chemical Reviews*, *115*(19), 10816–10906.

Hou, B., Cho, Y., Kim, B. S., Ahn, D., Lee, S., Park, J. B., Lee, Y.-W., Hong, J., Im, H., Morris, S. M., Sohn, J. I., Cha, S. N., & Kim, J. M. (2017). Red green blue emissive lead sulfide quantum dots: Heterogeneous synthesis and applications. *Journal of Materials Chemistry C*, *5*(15), 3692–3698.

Hou, H., Banks, C. E., Jing, M., Zhang, Y., & Ji, X. (2015). Carbon quantum dots and their derivative 3D porous carbon frameworks for sodium-ion batteries with ultralong cycle life. *Advanced Materials*, *27*(47), 7861–7866.

Iijima, S. (1991). Helical microtubules of graphitic carbon. *Nature*, *354*, 56–58.

Iijima, S., Yudasaka, M., Yamada, R., Bandow, S., Suenaga, K., Kokai, F., & Takahashi, K. (1999). Nano-aggregates of single-walled graphitic carbon nano-horns. *Chemical Physics Letters*, *309*(3–4), 165–170.

Jaiswal, A., Ghosh, S. S., & Chattopadhyay, A. (2012). One step synthesis of C-dots by microwave mediated caramelization of poly (ethylene glycol). *Chemical Communications*, *48*(3), 407–409.

Jaiswal, A., Ghsoh, S. S., & Chattopadhyay, A. (2012). Quantum dot impregnated-chitosan film for heavy metal ion sensing and removal. *Langmuir*, *28*(44), 15687–15696.

Jiang, K., Sun, S., Zhang, L., Lu, Y., Wu, A., Cai, C., & Lin, H. (2015). Red, green, and blue luminescence by carbon dots: Full-color emission tuning and multicolor cellular imaging. *Angewandte Chemie*, *127*(18), 5450–5453.

Jiao, Y., Sun, H., Jia, Y., Liu, Y., Gao, Y., Xian, M., Shuang, S., & Dong, C. (2019). Functionalized fluorescent carbon nanoparticles for sensitively targeted of folate-receptor-positive cancer cells. *Microchemical Journal*, *146*, 464–470.

Jung, Y. K., Shin, E., & Kim, B. S. (2015). Cell nucleus-targeting zwitterionic carbon dots. *Scientific Reports*, *5*(1), 1–9.

Kainth, S., Maity, B., & Basu, S. (2020). Deciphering the interaction of solvents with dual emissive carbon dots: A photoluminescence study and its response for different metal ions. *Materials Science and Engineering C*, *108*(November 2019), 110443.

Kang, S., Pinault, M., Pfefferle, L. D., & Elimelech, M. (2007). Single-walled carbon nanotubes exhibit strong antimicrobial activity. *Langmuir*, *23*(17), 8670–8673.

Kapri, S., Majee, R., & Bhattacharyya, S. (2018). Chemical modifications of porous carbon Nanospheres obtained from ubiquitous precursors for targeted drug delivery and live cell imaging. *ACS Sustainable Chemistry & Engineering*, *6*(7), 8503–8514.

Karthik, P. S., Himaja, A. L., & Singh, S. P. (2014). Carbon-allotropes: Synthesis methods, applications and future perspectives. *Carbon Letters*, *15*(4), 219–237.

Kazemizadeh, F., Malekfar, R., & Parvin, P. (2017). Pulsed laser ablation synthesis of carbon nanoparticles in vacuum. *Journal of Physics and Chemistry of Solids*, *104*(December 2016), 252–256.

Khan, M. S., Pandey, S., Talib, A., Bhaisare, M. L., & Wu, H. F. (2015). Controlled delivery of dopamine hydrochloride using surface modified carbon dots for neuro diseases. *Colloids and Surfaces B: Biointerfaces*, *134*, 140–146.

Khanam, A., Tripathi, S. K., Roy, D., & Nasim, M. (2013). A facile and novel synthetic method for the preparation of hydroxyl capped fluorescent carbon nanoparticles. *Colloids and Surfaces B: Biointerfaces*, *102*, 63–69.

Khare, P., Bhati, A., Anand, S. R., Gunture, & Sonkar, S. K. (2018). Brightly fluorescent zinc-doped red-emitting carbon dots for the sunlight-induced Photoreduction of Cr(VI) to Cr(III). *ACS Omega*, *3*(5), 5187–5194.

Kroto, H. W., Heath, J. R., O'Brien, S. C., Curl, R. F., & Smalley, R. E. (1985). C 60: buckminsterfullerene. *Nature*, *318*(6042), 162–163.

Kumar, J. P., Konwarh, R., Kumar, M., Gangrade, A., & Mandal, B. B. (2018). Potential Nanomedicine applications of multifunctional carbon nanoparticles developed using green technology. *ACS Sustainable Chemistry & Engineering*, *6*(1), 1235–1245.

Kumar, K., Moitra, P., Bashir, M., Kondaiah, P., & Bhattacharya, S. (2020). Natural tripeptide capped pH-sensitive gold nanoparticles for efficacious doxorubicin delivery both in vitro and in vivo. *Nanoscale*, *12*(2), 1067–1074.

Kumari, A., Kumar, A., Sahu, S. K., & Kumar, S. (2018). Synthesis of green fluorescent carbon quantum dots using waste polyolefins residue for Cu^{2+} ion sensing and live cell imaging. *Sensors and Actuators, B: Chemical*, *254*, 197–205.

Kundu, A., Nandi, S., Das, P., & Nandi, A. K. (2016). Facile and green approach to prepare fluorescent carbon dots: Emergent nanomaterial for cell imaging and detection of vitamin B2. *Journal of Colloid and Interface Science*, *468*, 276–283.

Lackner, J. M., & Waldhauser, W. (2010). Diamond and diamond-like carbon coated surfaces as biomaterials. *BHM Berg-und Hüttenmännische Monatshefte*, *155*(11), 528–533.

Lesani, P., Singh, G., Viray, C. M., Ramaswamy, Y., Zhu, D. M., Kingshott, P., Lu, Z., … Zreiqat, H. (2020). Two-photon dual-emissive carbon dot-based probe: Deep-tissue imaging and ultrasensitive sensing of intracellular ferric ions. *ACS Applied Materials & Interfaces*, *12*(16), 18395–18406.

Li, H., Zhang, Y., Wang, L., Tian, J., & Sun, X. (2011). Nucleic acid detection using carbon nanoparticles as a fluorescent sensing platform. *Chemical Communications*, *47*(3), 961–963.

Li, X., Zhang, S., Kulinich, S. A., Liu, Y., & Zeng, H. (2014). Engineering surface states of carbon dots to achieve controllable luminescence for solid-luminescent composites and sensitive be 2+ detection. *Scientific Reports*, *4*(1), 1–8.

Li, Y., Bai, G., Zeng, S., & Hao, J. (2019). Theranostic carbon dots with innovative NIR-II emission for in vivo renal-excreted optical imaging and photothermal therapy. *ACS Applied Materials & Interfaces*, *11*(5), 4737–4744.

Li, Y., Chen, H., Dong, Y., Li, K., Li, L., & Li, J. (2016). Carbon nanoparticles/soy protein isolate bio-films with excellent mechanical and water barrier properties. *Industrial Crops and Products*, *82*, 133–140.

Liang, W., Shi, H., Yang, X., Wang, J., Yang, W., Zhang, H., & Liu, L. (2020). Recent advances in AFM-based biological characterization and applications at multiple levels. *Soft Matter*, *16*(39), 8962–8984.

Liu, L., Peng, Q., & Li, Y. (2008). Preparation of CdSe quantum dots with full color emission based on a room temperature injection technique. *Inorganic Chemistry*, *47*(11), 5022–5028.

Liu, Z., Robinson, J. T., Sun, X., & Dai, H. (2008). PEGylated nanographene oxide for delivery of water-insoluble cancer drugs. *Journal of the American Chemical Society*, *130*(33), 10876–10877.

May, J. L., Erogbogbo, F., Yong, K. T., Ding, H., Law, W. C., Swihart, M. T., & Prasad, P. N. (2012). Enhancing silicon quantum dot uptake by pancreatic cancer cells via pluronic® encapsulation and antibody targeting. *Journal of Solid Tumors*, *2*(3), 24.

McHugh, K. J., Jing, L., Behrens, A. M., Jayawardena, S., Tang, W., Gao, M., Langer, R., & Jaklenec, A. (2018). Biocompatible semiconductor quantum dots as cancer imaging agents. *Advanced Materials*, *30*(18), 1706356.

Mehta, V. N., Chettiar, S. S., Bhamore, J. R., Kailasa, S. K., & Patel, R. M. (2017). Green synthetic approach for synthesis of fluorescent carbon dots for Lisinopril drug delivery system and their confirmations in the cells. *Journal of Fluorescence*, *27*(1), 111–124.

Mehta, V. N., Jha, S., Basu, H., Singhal, R. K., & Kailasa, S. K. (2015). One-step hydrothermal approach to fabricate carbon dots from apple juice for imaging of mycobacterium and fungal cells. *Sensors and Actuators, B: Chemical*, *213*, 434–443.

Misra, S. K., Chang, H. H., Mukherjee, P., Tiwari, S., Ohoka, A., & Pan, D. (2015). Regulating biocompatibility of carbon spheres via defined nanoscale chemistry and a careful selection of surface functionalities. *Scientific Reports*, *5*, 14986.

Misra, S. K., Moitra, P., Chhikara, B. S., Kondaiah, P., & Bhattacharya, S. (2012). Loading of single-walled carbon nanotubes in cationic cholesterol suspensions significantly improves gene transfection efficiency in serum. *Journal of Materials Chemistry*, *22*(16), 7985–7998.

Misra, S. K., Mukherjee, P., Chang, H. H., Tiwari, S., Gryka, M., Bhargava, R., & Pan, D. (2016). Multi-functionality redefined with colloidal carotene carbon nanoparticles for synchronized chemical imaging, enriched cellular uptake and therapy. *Scientific Reports*, *6*(December), 1–16.

Misra, S. K., Ohoka, A., Kolmodin, N. J., & Pan, D. (2015). Next generation carbon nanoparticles for efficient gene therapy. *Molecular Pharmaceutics*, *12*(2), 375–385.

Misra, S. K., Ostadhossein, F., Babu, R., Kus, J., Tankasala, D., Sutrisno, A., Walsh, K. A., Bromfield, C. R., & Pan, D. (2017). 3D-printed multidrug-eluting stent from graphene-Nanoplatelet-doped biodegradable polymer composite. *Advanced Healthcare Materials*, *6*(11), 1700008.

Misra, S. K., Ostadhossein, F., Daza, E., Johnson, E. V., & Pan, D. (2016). Hyperspectral imaging offers visual and quantitative evidence of drug release from zwitterionic-phospholipid-nanocarbon when concurrently tracked in 3D intracellular space. *Advanced Functional Materials*, *26*(44), 8031–8041.

Misra, S. K., Srivastava, I., Khamo, J. S., Krishnamurthy, V. V., Sar, D., Schwartz-Duval, A. S., Soares, J., Zhang, K., & Pan, D. (2018). Carbon dots with induced surface oxidation permits imaging at single-particle level for intracellular studies. *Nanoscale*, *10*(39), 18510–18519.

Misra, S. K., Srivastava, I., Tripathi, I., Daza, E., Ostadhossein, F., & Pan, D. (2017). Macromolecularly "caged" carbon nanoparticles for intracellular trafficking via switchable photoluminescence. *Journal of the American Chemical Society*, *139*(5), 1746–1749.

Moitra, P., Alafeef, M., Dighe, K., Sheffield, Z., Dahal, D., & Pan, D. (2021). Synthesis and characterization of N-gene targeted NIR-II fluorescent probe for selective localisation of SARS-CoV-2. *Chemical Communications*, *57*(51), 6229–6232.

Moitra, P., Bhagat, D., Kamble, V. B., Umarji, A. M., Pratap, R., & Bhattacharya, S. (2021). First example of engineered β-cyclodextrinylated MEMS devices for volatile pheromone sensing of olive fruit pests. *Biosensors and Bioelectronics*, *173*, 112728.

Moitra, P., Subramanian, Y., & Bhattacharya, S. (2017). Concentration dependent self-assembly of TrK-NGF receptor derived tripeptide: New insights from experiment and computer simulations. *The Journal of Physical Chemistry B*, *121*(4), 815–824.

Mukherjee, P., Misra, S. K., Gryka, M. C., Chang, H. H., Tiwari, S., Wilson, W. L., Scott, J. W., Bhargava, R., & Pan, D. (2015). Tunable luminescent carbon Nanospheres with well-defined nanoscale chemistry for synchronized imaging and therapy. *Small*, *11*(36), 4691–4703.

Murugan, N., Prakash, M., Jayakumar, M., Sundaramurthy, A., & Sundramoorthy, A. K. (2019). Green synthesis of fluorescent carbon quantum dots from Eleusine coracana and their application as a fluorescence 'turn-off' sensor probe for selective detection of Cu^{2+}. *Applied Surface Science*, *476*(September 2018), 468–480.

Muthukumar, T., Prabhavathi, S., Chamundeeswari, M., & Sastry, T. P. (2014). Bio-modified carbon nanoparticles loaded with methotrexate possible carrier for anticancer drug delivery. *Materials Science and Engineering C*, *36*(1), 14–19.

Naik, V., Zantye, P., Gunjal, D., Gore, A., Anbhule, P., Kowshik, M., Bhosale, S. V., & Kolekar, G. (2019). Nitrogen-doped carbon dots via hydrothermal synthesis: Naked eye fluorescent sensor for dopamine and used for multicolor cell imaging. *ACS Applied Bio Materials*, *2*(5), 2069–2077.

Nakamura, Y., Mochida, A., Choyke, P. L., & Kobayashi, H. (2016). Nanodrug delivery: Is the enhanced permeability and retention effect sufficient for curing cancer? *Bioconjugate Chemistry*, *27*(10), 2225–2238.

Nakayama-Ratchford, N., Bangsaruntip, S., Sun, X., Welsher, K., & Dai, H. (2007). Noncovalent functionalization of carbon nanotubes by fluorescein–polyethylene glycol: Supramolecular conjugates with pH-dependent absorbance and fluorescence. *Journal of the American Chemical Society*, *129*(9), 2448–2449.

Narayan, R. J., Wei, W., Jin, C., Andara, M., Agarwal, A., Gerhardt, R. A., Shih, C. C., Shih, C. M., Lin, S. J., Su, Y. Y., Ramamurti, R., & Singh, R. N. (2006). Microstructural and biological properties of nanocrystalline diamond coatings. *Diamond and Related Materials*, *15*(11–12), 1935–1940.

Nguyen, H. A., Srivastava, I., Pan, D., & Gruebele, M. (2020). Unraveling the fluorescence mechanism of carbon dots with sub-single-particle resolution. *ACS Nano*, *14*(5), 6127–6137.

Novoselov, K. S., Geim, A. K., Morozov, S. V., Jiang, D., Zhang, Y., Dubonos, S. V., Grigorieva, I. V., & Firsov, A. A. (2004). Electric field effect in atomically thin carbon films. *Science*, *306*(5696), 666–669.

Olesiak-Banska, J., Waszkielewicz, M., Obstarczyk, P., & Samoc, M. (2019). Two-photon absorption and photoluminescence of colloidal gold nanoparticles and nanoclusters. *Chemical Society Reviews*, *48*(15), 4087–4117.

Ostadhossein, F., & Pan, D. (2017). Functional carbon nanodots for multiscale imaging and therapy. *WIREs Nanomedicine and Nanobiotechnology*, *9*(3), e1436.

Pal, A., Ahmad, K., Dutta, D., & Chattopadhyay, A. (2019). Boron doped carbon dots with unusually high photoluminescence quantum yield for Ratiometric intracellular pH sensing. *ChemPhysChem*, *20*(8), 1018–1027.

Pan, L., Sun, S., Zhang, A., Jiang, K., Zhang, L., Dong, C., Huang, Q., Wu, A., & Lin, H. (2015). Truly fluorescent excitation-dependent carbon dots and their applications in multicolor cellular imaging and multidimensional sensing. *Advanced Materials*, *27*(47), 7782–7787.

Pan, L., Sun, S., Zhang, L., Jiang, K., & Lin, H. (2016). Near-infrared emissive carbon dots for two-photon fluorescence bioimaging. *Nanoscale*, *8*(39), 17350–17356.

Pandit, S., Banerjee, T., Srivastava, I., Nie, S., & Pan, D. (2019). Machine learning-assisted array-based biomolecular sensing using surface-functionalized carbon dots. *ACS sensors*, *4*(10), 2730–2737.

Park, J., Nam, J., Won, N., Jin, H., Jung, S., Jung, S., Cho, S.-H., & Kim, S. (2011). Compact and stable quantum dots with positive, negative, or zwitterionic surface: Specific cell interactions and non-specific adsorptions by the surface charges. *Advanced Functional Materials*, *21*(9), 1558–1566.

Patidar, R., Rebary, B., Sanghani, D. A., Bhadu, G. R., & Paul, P. (2017). Fluorescent carbon nanoparticles obtained from charcoal via green methods and their application for sensing Fe^{3+} in an aqueous medium. *Luminescence*, *32*(8), 1466–1472.

Peterson, J. J., & Krauss, T. D. (2006). Fluorescence spectroscopy of single lead sulfide quantum dots. *Nano Letters*, *6*(3), 510–514.

Pham, C. T., Thomas, D. G., Beiser, J., Mitchell, L. M., Huang, J. L., Senpan, A., Hu, G., Gordon, M., Baker, N. A., Pan, D., Lanza, G. M., & Hourcade, D. E. (2014). Application of a hemolysis assay for analysis of complement activation by perfluorocarbon nanoparticles. *Nanomedicine: Nanotechnology, Biology and Medicine*, *10*(3), 651–660.

Philippidis, A., Spyros, A., Anglos, D., Bourlinos, A. B., Zbořil, R., & Giannelis, E. P. (2013). Carbon-dot organic surface modifier analysis by solution-state NMR spectroscopy. *Journal of Nanoparticle Research*, *15*(7), 1–9.

Pooja, D., Singh, L., Thakur, A., & Kumar, P. (2019). Green synthesis of glowing carbon dots from Carica papaya waste pulp and their application as a label-freechemo probe for chromium detection in water. *Sensors and Actuators B: Chemical*, *283*, 363–372.

Prasad, B. N., Padmesh, T. V. N., Suganya, K. U., Govindaraju, K., & Kumar, V. G. (2016). Facile green synthesis of carbon nanoparticles using medicinally potent Pongamia pinnata shoots. *Journal of Environment & Biotechnology Research*, *3*(1), 12–16.

Priyadarsini, S., Mohanty, S., Mukherjee, S., Basu, S., & Mishra, M. (2018). Graphene and graphene oxide as nanomaterials for medicine and biology application. *Journal of Nanostructure in Chemistry*, *8*(2), 123–137.

Pu, K., Shuhendler, A. J., Jokerst, J. V., Mei, J., Gambhir, S. S., Bao, Z., & Rao, J. (2014). Semiconducting polymer nanoparticles as photoacoustic molecular imaging probes in living mice. *Nature Nanotechnology*, *9*(3), 233–239.

Pudza, M. Y., Abidin, Z. Z., Rashid, S. A., Yasin, F. M., Noor, A. S. M., & Issa, M. A. (2020). Eco-friendly sustainable fluorescent carbon dots for the adsorption of heavy metal ions in aqueous environment. *Nanomaterials*, *10*(2), 315.

Rai, S., Singh, B. K., Bhartiya, P., Singh, A., Kumar, H., Dutta, P. K., & Mehrotra, G. K. (2017). Lignin derived reduced fluorescence carbon dots with theranostic approaches: Nano-drug-carrier and bioimaging. *Journal of Luminescence*, *190*(April), 492–503.

Raman, C. V. (1929). Diamagnetism and crystal structure. *Nature*, *123*(3112), 945–945.

Ramanathan, T., Abdala, A. A., Stankovich, S., Dikin, D. A., Herrera-Alonso, M., Piner, R. D., Adamson, D. H., Schniepp, H. C., Chen, X., Ruoff, R. S., Nguyen, S. T., Aksay, I. A., Prud'Homme, R. K., & Nguyen, S. T. (2008). Functionalized graphene sheets for polymer nanocomposites. *Nature Nanotechnology*, *3*(6), 327–331.

Ramar, V., Moothattu, S., & Balasubramanian, K. (2018). Metal free, sunlight and white light based photocatalysis using carbon quantum dots from Citrus grandis: A green way to remove pollution. *Solar Energy*, *169*(April), 120–127.

Rao, C. N. R., Biswas, K., Subrahmanyam, K. S., & Govindaraj, A. (2009). Graphene, the new nanocarbon. *Journal of Materials Chemistry*, *19*(17), 2457–2469.

Ray, P., Moitra, P., & Pan, D. (2021). Emerging theranostic applications of carbon dots and its variants. *View*, 20200089. https://doi.org/10.1002/VIW.20200089

Ray, S. C., Saha, A., Jana, N. R., & Sarkar, R. (2009). Fluorescent carbon nanoparticles: Synthesis, characterization, and bioimaging application. *The Journal of Physical Chemistry C*, *113*(43), 18546–18551.

Sahoo, N. K., Jana, G. C., Aktara, M. N., Das, S., Nayim, S., Patra, A., Bhattacharjee, P., Bhadra, K., & Hossain, M. (2020). Carbon dots derived from lychee waste: Application for Fe^{3+} ions sensing in real water and multicolor cell imaging of skin melanoma cells. *Materials Science and Engineering C*, *108*, 110429.

Sarkar, N., Sahoo, G., Das, R., Prusty, G., & Swain, S. K. (2017). Carbon quantum dot tailored calcium alginate hydrogel for pH responsive controlled delivery of vancomycin. *European Journal of Pharmaceutical Sciences*, *109*(July), 359–371.

Schinazi, R. F., Sijbesma, R. I. N. T., Srdanov, G., Hill, C. L., & Wudl, F. (1993). Synthesis and virucidal activity of a water-soluble, configurationally stable, derivatized C60 fullerene. *Antimicrobial Agents and Chemotherapy*, *37*(8), 1707–1710.

Schwenke, A. M., Hoeppener, S., & Schubert, U. S. (2015). Synthesis and modification of carbon nanomaterials utilizing microwave heating. *Advanced Materials*, *27*(28), 4113–4141.

Semeniuk, M., Yi, Z., Poursorkhabi, V., Tjong, J., Jaffer, S., Lu, Z. H., & Sain, M. (2019). Future perspectives and review on organic carbon dots in electronic applications. *ACS Nano*, *13*(6), 6224–6255.

Sharma, S. K., Chiang, L. Y., & Hamblin, M. R. (2011). Photodynamic therapy with fullerenes in vivo: Reality or a dream? *Nanomedicine*, *6*(10), 1813–1825.

Sharma, V., Kaur, N., Tiwari, P., & Mobin, S. M. (2018). Full color emitting fluorescent carbon material as reversible pH sensor with multi-color live cell imaging. *Journal of Photochemistry and Photobiology B: Biology*, *182*(February), 137–145.

Sharma, V., Kaur, N., Tiwari, P., Saini, A. K., & Mobin, S. M. (2018). Multifunctional fluorescent "off-on-off" nanosensor for Au^{3+} and S^{2-} employing N-S co-doped carbon–dots. *Carbon*, *139*, 393–403.

Sharma, V., Saini, A. K., & Mobin, S. M. (2016). Multicolour fluorescent carbon nanoparticle probes for live cell imaging and dual palladium and mercury sensors. *Journal of Materials Chemistry B*, *4*(14), 2466–2476.

Shen, H., Zhang, L., Liu, M., & Zhang, Z. (2012). Biomedical applications of graphene. *Theranostics*, *2*(3), 283.

Shojaei, T. R., Salleh, M. A. M., Sijam, K., Rahim, R. A., Mohsenifar, A., Safarnejad, R., & Tabatabaei, M. (2016). Fluorometric immunoassay for detecting the plant virus citrus tristeza using carbon nanoparticles acting as quenchers and antibodies labeled with CdTe quantum dots. *Microchimica Acta*, *183*(7), 2277–2287.

Sk, M. P., Jaiswal, A., Paul, A., Ghosh, S. S., & Chattopadhyay, A. (2012). Presence of amorphous carbon nanoparticles in food caramels. *Scientific Reports*, *2*(1), 1–5.

Skaltsas, T., Goulielmaki, M., Pintzas, A., Pispas, S., & Tagmatarchis, N. (2017). Carbon quantum dots/block copolymer ensembles for metal-ion sensing and bioimaging. *Journal of Materials Chemistry B*, *5*(27), 5397–5402.

Skaltsas, T., Stergiou, A., Chronopoulos, D. D., Zhao, S., Shinohara, H., & Tagmatarchis, N. (2016). All-carbon nanosized hybrid materials: Fluorescent carbon dots conjugated to multiwalled carbon nanotubes. *The Journal of Physical Chemistry C*, *120*(16), 8550–8558.

Song, S., Shen, H., Wang, Y., Chu, X., Xie, J., Zhou, N., & Shen, J. (2020). Biomedical application of graphene: From drug delivery, tumor therapy, to theranostics. *Colloids and Surfaces B: Biointerfaces*, *185*, 110596.

Soni, H., & Pamidimukkala, P. S. (2018). Green synthesis of N, S co-doped carbon quantum dots from triflic acid treated palm shell waste and their application in nitrophenol sensing. *Materials Research Bulletin*, *108*(August), 250–254.

Srinivasan, V., Kathiravan, A., Kathiresan, M., Krishnan, G., & Jhonsi, M. A. (2020). Facile synthesis of carbon nanocubes and its applications for sensing antibiotics. *Journal of Photochemistry and Photobiology A: Chemistry*, *403*(August), 112855.

Srivastava, I., Khamo, J. S., Pandit, S., Fathi, P., Huang, X., Cao, A., Haasch, R. T., Nie, S., Zhang, K., & Pan, D. (2019). Influence of electron acceptor and electron donor on the photophysical properties of carbon dots: A comparative investigation at the bulk-state and single-particle level. *Advanced Functional Materials*, *29*(37), 1902466.

Srivastava, I., Misra, S. K., Bangru, S., Boateng, K. A., Soares, J. A., Schwartz-Duval, A. S., Kalsotra, A., & Pan, D. (2020). Complementary oligonucleotide conjugated multicolor carbon dots for intracellular recognition of biological events. *ACS Applied Materials & Interfaces*, *12*(14), 16137–16149.

Srivastava, I., Misra, S. K., Ostadhossein, F., Daza, E., Singh, J., & Pan, D. (2017). Surface chemistry of carbon nanoparticles functionally select their uptake in various stages of cancer cells. *Nano Research*, *10*(10), 3269–3284.

Srivastava, I., Moitra, P., Sar, D., Wang, K., Alafeef, M., Scott, J., & Pan, D. (2021). Luminescence switching in polymerically confined carbon nanoparticles triggered by UV-light. *Nanoscale*, *13*(38), 16288–16295.

Srivastava, I., Sar, D., Mukherjee, P., Schwartz-Duval, A. S., Huang, Z., Jaramillo, C., Civantos, A., Tripathi, I., Allain, J. P., Bhargava, R., & Pan, D. (2019). Enzyme-catalysed biodegradation of carbon dots follows sequential oxidation in a time dependent manner. *Nanoscale*, *11*(17), 8226–8236.

Subrahmanyam, K. S., Ghosh, A., Gomathi, A., Govindaraj, A., & Rao, C. N. R. (2009). Covalent and noncovalent functionalization and solubilization of graphene. *Nanoscience and Nanotechnology Letters*, *1*(1), 28–31.

Sun, Y. P., Zhou, B., Lin, Y., Wang, W., Fernando, K. S., Pathak, P., Meziani, M. J., Harruff, B. A., Wang, X., Wang, H., Luo, P. G., Yang, H., Kose, M. E., Chen, B., Veca, L. M., & Xie, S. Y. (2006). Quantum-sized carbon dots for bright and colorful photoluminescence. *Journal of the American Chemical Society*, *128*(24), 7756–7757.

Tan, D., Yamada, Y., Zhou, S., Shimotsuma, Y., Miura, K., & Qiu, J. (2014). Carbon nanodots with strong nonlinear optical response. *Carbon*, *69*, 638–640.

Tian, L., Ghosh, D., Chen, W., Pradhan, S., Chang, X., & Chen, S. (2009). Nanosized carbon particles from natural gas soot. *Chemistry of Materials*, *21*(13), 2803–2809.

Tiwari, P., Kaur, N., Sharma, V., & Mobin, S. M. (2020). A spectroscopic investigation of carbon dots and its reduced state towards fluorescence performance. *Journal of Photochemistry and Photobiology A: Chemistry*, *403*(August), 112847.

Tripathi, S., Sonkar, S. K., & Sarkar, S. (2011). Growth stimulation of gram (Cicer arietinum) plant by water soluble carbon nanotubes. *Nanoscale*, *3*(3), 1176–1181.

Tsoi, K. M., MacParland, S. A., Ma, X. Z., Spetzler, V. N., Echeverri, J., Ouyang, B., Fadel, S. M., Sykes, E. A., Goldaracena, N., Kaths, J. M., Conneely, J. B., Alman, B. A., Selzner, M., Ostrowski, M. A., Adeyi, O. A., Zilman, A., McGilvray, I. D., & Chan, W. C. (2016). Mechanism of hard-nanomaterial clearance by the liver. *Nature Materials*, *15*(11), 1212–1221.

Victoria, F., Manioudakis, J., Zaroubi, L., Findlay, B., & Naccache, R. (2020). Tuning residual chirality in carbon dots with anti-microbial properties. *RSC Advances*, *10*(53), 32202–32210.

Wang, X., Feng, Y., Dong, P., & Huang, J. (2019). A mini review on carbon quantum dots: Preparation, properties, and electrocatalytic application. *Frontiers in Chemistry*, 7, 671.

Wang, Y., Bao, L., Liu, Z., & Pang, D. W. (2011). Aptamer biosensor based on fluorescence resonance energy transfer from upconverting phosphors to carbon nanoparticles for thrombin detection in human plasma. *Analytical Chemistry*, 83(21), 8130–8137.

Wen, J., Xu, Y., Li, H., Lu, A., & Sun, S. (2015). Recent applications of carbon nanomaterials in fluorescence biosensing and bioimaging. *Chemical Communications*, 51(57), 11346–11358.

Willner, M. R., & Vikesland, P. J. (2018). Nanomaterial enabled sensors for environmental contaminants. *Journal of Nanobiotechnology*, 16(1), 95.

Wu, L., Cai, X., Nelson, K., Xing, W., Xia, J., Zhang, R., Stacy, A. J., Luderer, M., Lanza, G. M., Wang, L. V., Shen, B., & Pan, D. (2013). A green synthesis of carbon nanoparticles from honey and their use in real-time photoacoustic imaging. *Nano Research*, 6(5), 312–325.

Xiong, Y., Zhang, X., Richter, A. F., Li, Y., Döring, A., Kasák, P., Popelka, A., Schneider, J., Kershaw, S. V., Yoo, S. J., Kim, J. G., Zhang, W., Zheng, W., Ushakova, E. V., Feldmann, J., & Rogach, A. L. (2019). Chemically synthesized carbon nanorods with dual polarized emission. *ACS Nano*, 13(10), 12024–12031.

Yan, A., Lau, B. W., Weissman, B. S., Külaots, I., Yang, N. Y. C., Kane, A. B., & Hurt, R. H. (2006). Biocompatible, hydrophilic, supramolecular carbon nanoparticles for cell delivery. *Advanced Materials*, 18(18), 2373–2378.

Yang, K., Zhang, S., Zhang, G., Sun, X., Lee, S. T., & Liu, Z. (2010). Graphene in mice: Ultrahigh in vivo tumor uptake and efficient photothermal therapy. *Nano Letters*, 10(9), 3318–3323.

Yang, R., Tang, Z., Yan, J., Kang, H., Kim, Y., Zhu, Z., & Tan, W. (2008). Noncovalent assembly of carbon nanotubes and single-stranded DNA: An effective sensing platform for probing biomolecular interactions. *Analytical Chemistry*, 80(19), 7408–7413.

Yang, Z. C., Li, X., & Wang, J. (2011). Intrinsically fluorescent nitrogen-containing carbon nanoparticles synthesized by a hydrothermal process. *Carbon*, 49(15), 5207–5212.

Yogesh, G. K., Shuaib, E. P., Kalai Priya, A., Rohini, P., Anandhan, S. V., Krishnan, U. M., Kalyanavalli, V., Shukla, S., & Sastikumar, D. (2021). Synthesis of water-soluble fluorescent carbon nanoparticles (CNPs) from nanosecond pulsed laser ablation in ethanol. *Optics and Laser Technology*, 135(October), 106717.

Yogesh, G. K., Shuaib, E. P., & Sastikumar, D. (2017). Photoluminescence properties of carbon nanoparticles synthesized from activated carbon powder (4% ash) by laser ablation in solution. *Materials Research Bulletin*, 91, 220.

Zhao, Q. L., Zhang, Z. L., Huang, B. H., Peng, J., Zhang, M., & Pang, D. W. (2008). Facile preparation of low cytotoxicity fluorescent carbon nanocrystals by electrooxidation of graphite. *Chemical Communications*, 41, 5116–5118.

Zheng, J., Zhang, C., & Dickson, R. M. (2004). Highly fluorescent, water-soluble, size-tunable gold quantum dots. *Physical Review Letters*, 93(7), 077402.

Zhou, J., Booker, C., Li, R., Zhou, X., Sham, T. K., Sun, X., & Ding, Z. (2007). An electrochemical avenue to blue luminescent nanocrystals from multiwalled carbon nanotubes (MWCNTs). *Journal of the American Chemical Society*, 129(4), 744–745.

Zhou, J., Yang, Y., & Zhang, C. Y. (2015). Toward biocompatible semiconductor quantum dots: From biosynthesis and bioconjugation to biomedical application. *Chemical Reviews*, 115(21), 11669–11717.